Final Progress Report for Project Entitled:

Tracer Methods for Characterizing Fracture Creation in Engineered Geothermal Systems

GO18193

Peter Rose[1], Principal Investigator; Joel Harris[2], Co-Investigator;

Karsten Pruess[3], Tianfu Xu[3], Michael Bartl[2], Mike Mella[1], Kevin Leecaster[1], Scott Fayer[1], Steve Olsen[4], Randy Normann[5], Susan Petty[6]

[1]EGI, University of Utah
[2]Department of Chemistry, University of Utah
[3]Lawrence Berkeley National Laboratory, California
[4]Red Rock Analog Design, Salt Lake City
[5]Perma Works, Albuquerque
[6]AltaRock Energy, Seattle

Table of Contents for Phase I, Year 1

Project Objectives

The aim of this proposal is to develop, through novel high-temperature-tracing approaches, three technologies for characterizing fracture creation within Engineered Geothermal Systems (EGS). The objective of a first task is to identify, develop and demonstrate adsorbing tracers for characterizing interwell reservoir-rock surface areas and fracture spacing. The objective of a second task is to develop and demonstrate a methodology for measuring fracture surface areas adjacent to single wells. The objective of a third task is to design, fabricate and test an instrument that makes use of tracers for measuring fluid flow between newly created fractures and wellbores. In one method of deployment, it will be used to identify qualitatively which fractures were activated during a hydraulic stimulation experiment. In a second method of deployment, it will serve to measure quantitatively the rate of fluid flowing from one or more activated fracture during a production test following a hydraulic stimulation.

Task 1: Measuring Interwell Fracture Surface Area and Fracture Spacing Using Sorbing Tracers

The objective of this task is to develop and demonstrate a method for determining fracture surface area and fracture spacing within a geothermal reservoir based upon sorbing-tracer data. Our approach is based upon the completion of the following subtasks:

Task 1, Subtask 1: Design and Fabricate a Laboratory Reactor for Characterizing Tracer Sorption

Background and Previous Accomplishments

We constructed a geothermal reservoir flow simulator that consists of a high-pressure pump possessing minimal pulsation, adsorbing media column, ceramic heater, thermocouples, pressure gauges, chiller, and fraction collector.

Accomplishments (Kevin Leecaster)

We used the fluorescent tracer fluorescein to measure the volume of the pulse that the pump and delivery tubing will inject into the adsorbing media column (Figure 1). After evaluating several media types in the flow reactor, we switched to a different flow reactor column that retains the adsorbing media better and has a larger volume. It was decided to screen potential reactive tracers with a layered media of glass beads with ground samples of relevant rock types. Additionally, it was discovered that at high temperatures there was an induced thermal gradient within the column because the heating coil of the delivery tubing was not adequate. Parts have been ordered to remedy this, but not yet installed. We have added the capability to measure the heat transfer to the eluting solution by obtaining a data acquisition device for the pre- and post-column thermocouples.

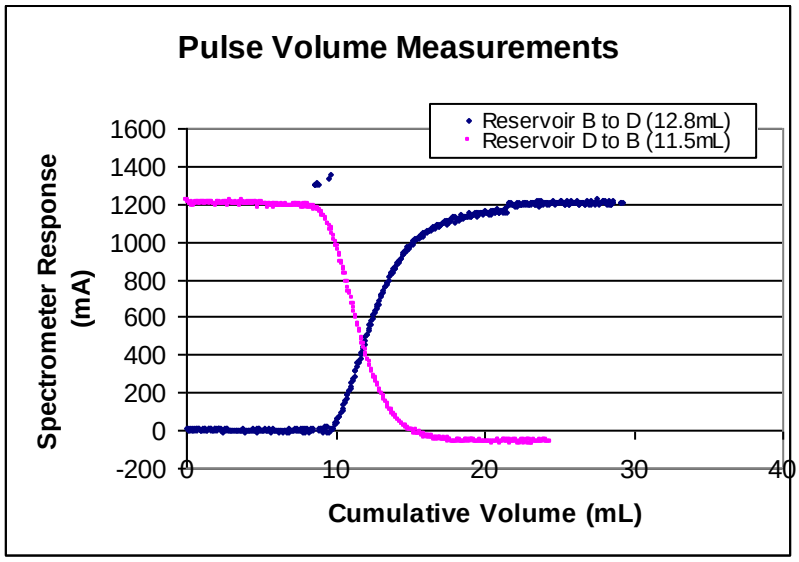

Figure 1. Adsorbing-media-column pulse volume measurement.

Task 1, Subtask 2: Conduct Search for Candidate Sorbing EGS Tracers

Background

Among the reversibly sorbing candidates that we have identified are the same cationic (positively charged) compounds used in groundwater sorption work, which sorb due to a charge that is opposite to that of the negatively-charged reservoir rock. Such compounds include ions such as Li^{+} and Sr^{++}, which are desirable since they are naturally occurring only at very low concentrations in reservoir water. Other candidates include cationic fluorescent compounds such as tinopal CBS. Another compounds that we have identified are the strongly sorbing scale inhibitors such as polycarboxylates, polyacrylates, and polymaleic anhydrides have been shown to sorb strongly but still reversibly within geothermal wellbores and formations.

Accomplishments (Kevin Leecaster)

Our initial search for candidate sorbing EGS tracers served to identify several for screening. Methylene blue is a common dye that is used in the construction & drilling industries to measure cation exchange capacity and has the promising property of endothermic adsorption onto perlite. Tinopal is a thermally stable compound that has had breakthrough curves that potentially indicated sorption. Rhodamine WT has been used in near-surface interwell tests and has been shown to be reactive based upon its breakthrough curve relative to conservative tracers. Another dye that we will be screening is Alcian blue because it is a 'hard' cation (small volume to charge ratio) that we think may help to increase sorption at higher temperatures. Finally, we have completed installing equipment and developing methods to measure ionic cations with our HPLC system and will screen for sorption of cations like Li & Sr at elevated temperatures.

Method development for the analysis of rhodamine WT with the HPLC was conducted, including separation of two distinct isomers. This isomer separation will allow us to examine the thermal stability of individual isomers and potentially provide an economical reactive tracer with two molecules that have similar diffusivities, but possibly different thermal stabilities.

We obtained samples of some of the other fluorescent dyes that we will examine for stability and retardation at temperature relative to a conservative tracer: Safranin O and Alcian Blue, as well as Methylene Blue, Tinopal CBS, Sr, and Li.

Task 1, Subtask 3: Conduct Sorption Screening Tests

Accomplishments (Kevin Leecaster)
We performed initial flow tests up to 1200 psi & 300°C. We will begin testing using clinoptilolite as the analogue geothermal reservoir medium. In order to best utilize traditional flow models, we have been carefully preparing the porous media with which we will screen candidate sorbing tracers. The material was crushed to provide a size fraction that is less than 1% of the column diameter by sieving the zeolite material through a 150 µm screen and retaining it on a 120 µm screen.

A preliminary column test (at 25° C) was run with rhodamine WT to provide a baseline conservative tracer measurement of the pore volume, as well as work out methodology and timing for the experiments. The resulting samples have almost all been analyzed, providing a partial breakthrough curve shown in figure 2. There was significant holdup of the rhodamine WT by the adsorbing media as well as an obvious difference between the adsorption of the two fluorescing species of rhodamine WT (labeled RWT1 & RWT2 in the figure).

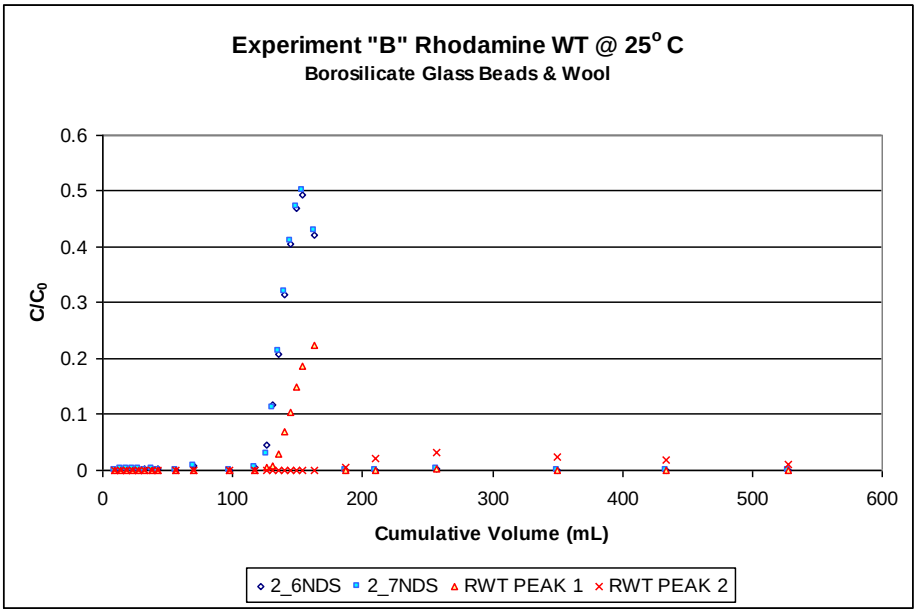

Figure 2. Preliminary low temperature column sorption test.

Task 1, Subtask 4: Develop a Model for Inverting Sorptive-Tracer Data to Calculate Interwell Fracture Surface Areas

The numerical and analytical methods being developed under Task 2, Subtask 1 will eventually be applied to this task.

Task 2: Measuring Fracture Surface Areas Adjacent to a Single Geothermal Well Using Tracers and Injection/Backflow Techniques

Task 2, Subtask 1: Develop a Numerical Model to Calculate Fracture Surface Areas from Injection/Backflow data

Background and Previous Accomplishments

At EGI, Scott Fayer:

A model was developed to calculate fracture surface area based upon the thermal decay of tracers having well characterized thermal decay kinetics. A paper was written by Fayer et al. (2009) for submission on May 11 for presentation at the 2009 GRC annual convention.

At LBNL, Karsten Pruess and Christine Doughty:

We started a literature survey on single well injection-withdrawal (SWIW) tests in fractured media that involve reversibly sorbing tracers. We are focusing on parameter sensitivities, especially the sensitivity to fracture-matrix interface area.

Accomplishments this Quarter

At EGI, Scott Fayer:

The expanded thermal decay model built last quarter was used to generate return curves for a hypothetical geothermal system. These curves represent a method for determining fracture spacing when compared to actual field returns curves. We are currently in the process of collaborating with other labs who have gained interest in this project to continue to build in features, and to compare against other code bases.

At LBNL, Karsten Pruess and Tianfu Xu:

TOUGH2 simulations were run for non-isothermal SWIW tests in fractured-porous media in which temperature plays the role of tracer. Different operational scenarios were explored for the sequence of fluid injection, a subsequent quiescent period, and withdrawal. Results show significant thermal contrast as a function of changes in fracture-wallrock surface area. A particle-tracking approach is being devised to compare the effect of reversibly sorbing tracers to the thermal effects.

Task 3: Design, Fabrication and Testing of a Downhole Instrument for Measuring Fracture Flow Following a Hydraulic Stimulation Experiment

Task 3, Subtask 1: Find and/or Synthesize an Appropriate Fluorescent Tracer for Downhole Fluorimetry

Background

The original fluorimeter design required that the tracers must fluoresce within the narrow window of 800-1000 nm. This is because the attenuation of neighboring visible light is too great over the target length of 9,000 ft of optical fiber. Likewise, any longer wavelength fluorescence is in appropriate for the silica-based CCD camera that will be used as a detector. Two near-IR fluorescent compounds were therefore identified: DTTCI and IR-125. The former is cationic, which may present problems (for this application) due to sorption. The latter is anionic and also likely more thermally stable.

Accomplishments (Michael H. Bartl, PI; Jacqueline T. Siy, graduate student)

The new fluorimeter design (see Task 3, Subtask 2 below) side steps the problems associated with deploying 9,000 ft of optical fiber. It is a wireline tool that promises to be much more durable and much more easily deployed than the optical fiber tool. The tracers that were originally designed for the long path lengths of optical fiber will still have application for the wireline tool. These are the newly synthesized PbS quantum dots that are described in the following section.

Commonly used high-temperature-stable tracers are based on organic dye molecules with emission in the ultraviolet range of the electromagnetic spectrum. Since this range is readily spectrally polluted by many naturally occurring reservoir contaminants, high-temperature-stable tracer species with emission bands at larger wavelengths (visible and near infrared) are highly desired. In particular, near infrared-emitting tracers (at wavelengths around 800-1000 nm) are of great interest due to reduced background absorption, fluorescence and light scattering in this range. Unfortunately, near infrared-emitting tracers based on organic dye molecules suffer, in general, from aggregation, photobleaching, and low fluorescence quantum yields. These obstacles, however, should be overcome by using semiconductor nanocrystals (“quantum dots”) as the emitting tracer species. Quantum dots are small crystallites (1-10 nm in diameter) of semiconducting compounds with tunable electronic and optical properties and high fluorescence quantum yields.

Initial efforts focused on synthesizing CdSe-based quantum dots that are water-soluble and have tunable fluorescence in the visible. For this, a synthesis method was adapted from literature reports that results in CdSe quantum dots with citrate molecules attached to their surface, rendering them water-soluble. The synthesis conditions were varied to fabricate quantum dots with different sizes (3-5 nm in diameter), resulting in green, yellow and orange emission colors. Furthermore, so-called core-shell structures were synthesized by covering the CdSe quantum dots with a thin shell of crystalline CdS. This extra shell minimizes surface defects of the CdSe core crystallite and thereby enhances the fluorescence quantum yield. Current efforts focus on

optimizing these core-shell architectures to produce water-soluble quantum dots with fluorescence quantum yields approaching those of conventionally used organic dye tracers.

In parallel to CdSe-based quantum dot synthesis we have also began to fabricate PbS quantum dots. The advantage of PbS is an inherently smaller electronic band gap, which shifts electronic and optical properties of PbS quantum dots into the near infrared range. So far we have successfully fabricated fluorescent PbS quantum dots with emission bands centered between 900 and 1000 nm. A current limitation of PbS quantum dots, however, is that synthesis routes require very hydrophobic (oily) conditions and as a result the synthesized quantum dots are insoluble in aqueous media. A central focus of current and future research is therefore to extend the water-based synthesis route that we successfully applied for CdSe quantum dots to PbS quantum dots.

Initial studies showed that CdSe and PbS-based quantum dots can be made water-soluble and display tunable fluorescence emission in the visible and near IR range, including the important 800 to 1000 nm wavelength range. These initial results are very encouraging and studies in the last funding period focused on up-scaling quantum dot production. Up-scaling of quantum dot production will be of great importance for field testing in an injection/backflow test in an EGS wellbore. However, up-scaling of conventional synthesis methods is generally a problem due to the high reaction temperatures (230-350 °C), which lead to the formation of temperature gradients in large reaction volumes. In addition, due to the fast nucleation and growth kinetics at high reaction temperatures injection of precursors has to occur very rapidly to avoid products with large unwanted size polydispersity.

We have recently developed a low-temperature (50-130 °C) synthesis route for the fabrication of high-quality colloidal nanocrystals. We recently were able to demonstrate first results, showing that the lowered synthesis temperatures allow up-scaling of CdSe quantum dot production. Up-scaling is pursued in two steps: 1) Increasing the concentration of produced quantum dots per reaction volume and 2) increasing the reaction volume per run. So far we focused on step 1 and were able to increase the concentration of quantum dots by a factor of 1000. This was accomplished by optimizing the ratio of quantum precursor components to surface-stabilizing ligands. Importantly, up-scaling did not lower the quality (structural and optical properties) of the synthesized CdSe quantum dots. The next steps will be to 1) continue optimizing the reaction parameters to further increase the production and 2) build a synthesis set-up that will enable increase of the reaction volume from currently 10-20 milliliters to several liters.

Task 3, Subtask 2: Design and Fabricate a Field Fluorimeter for Measuring Tracers Downhole

Accomplishments (Pete Rose, Mike Mella, Steve Olsen, Randy Normann)

A design of the field fluorimeter was completed. It will consist of a spectrometer (complete with fiber optics, a CCD camera and a laser light source). One of the problems identified with the design, however, is the need to mount the spectrometer on the coiled-tubing drum that will be used to deploy the fiber optic cable. The optical fiber will be deployed within the coiled tubing in order to protect it from the harsh environment within the wellbore. An alternative design is being developed that will allow for the deployment of the spectrometer downhole on a wireline, thus

avoiding the problems associated with deploying optical fiber over long distances within EGS wellbores.

A meeting was held with representatives from the high-temperature tool groups at Sandia National Laboratory (Doug Blankenship and Joe Henfling), the USGS (Steve Hickman), and DOE (Eric Hass and Bill Vandermeer), Perma Works (Randy Normann) and others for the purpose of establishing collaboration with these groups in anticipation of a design review for the borehole fluorimeter/flowmeter. Work continues on the design of the borehole fluorimeter/flowmeter in anticipation of that review.

Phases I and II, Year 2

Progress Report for Year Ending September 30, 2010:

Tracer Methods for Characterizing Fracture Creation in Engineered Geothermal Systems

GO18193

Peter Rose[1], Principal Investigator; Joel Harris[2], Co-Investigator;

Karsten Pruess[3], Tianfu Xu[3], Michael Bartl[2], Mike Mella[1], Kevin Leecaster[1], Scott Fayer[1], Bruce Boyes[4], Susan Petty[5]

[1]EGI, University of Utah
[2]Department of Chemistry, University of Utah
[3]Lawrence Berkeley National Laboratory, California
[4]Systronics, Salt Lake City
[5]AltaRock Energy, Seattle

Table of Contents for Phases I and II, Year 2

Project Objectives

Year 1

The aim of this proposal is to develop, through novel high-temperature-tracing approaches, three technologies for characterizing fracture creation within Engineered Geothermal Systems (EGS). The objective of a first task is to identify, develop and demonstrate adsorbing tracers for characterizing interwell reservoir-rock surface areas and fracture spacing. The objective of a second task is to develop and demonstrate a methodology for measuring fracture surface areas adjacent to single wells. The objective of a third task is to design, fabricate and test an instrument that makes use of tracers for measuring fluid flow between newly created fractures and wellbores. In one method of deployment, it will be used to identify qualitatively which fractures were activated during a hydraulic stimulation experiment. In a second method of deployment, it will serve to measure quantitatively the rate of fluid flowing from one or more activated fracture during a production test following a hydraulic stimulation.

Year 1, Subtask 1.1: Design and Fabricate a Laboratory Reactor for Characterizing Tracer Sorption

We constructed a geothermal reservoir flow simulator that consists of a high-pressure pump possessing minimal pulsation, column for holding adsorbing media, heating systems for column and pre-column fluid, thermocouples, pressure gauges, chiller, and fraction collector (Figure 1).

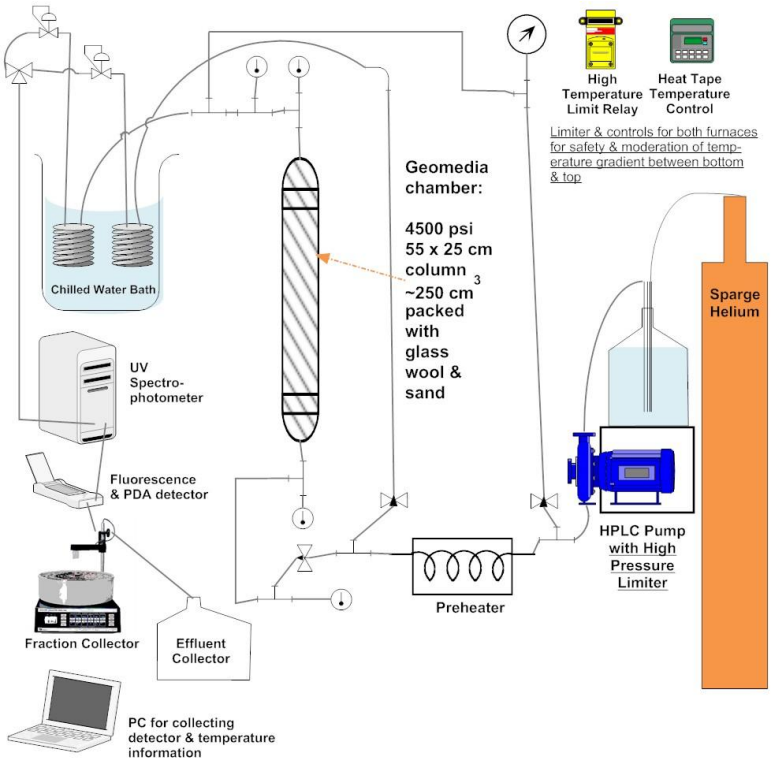

Figure 1. Laboratory Reactor Schematic

We are able to directly measure the tracer concentration in the column effluent after it passes through the chilling coils because of the incorporation of two photospectometric detectors, providing thorough breakthrough curves. We have added the capability to measure the heat transfer to the eluting solution by connecting the data acquisition device for the column inlet and outlet thermocouples. High temperature limiters were added to both the preheater and the column heater so that longer experiments could be run safely.

This subtask was completed on schedule. However, modifications to the design and fabrication of the reactor were intended to be continuously made throughout the remainder of this program. Since the completion of this subtask, the following additions/improvements to the reactor were completed:

Second Quarter, 2010

We acquired high temperature o-rings for the column that will allow experiments up to 315° C. Replacement of the original HPLC pump was required because of a mechanical failure. We modified the in-line fluorescence detector to measure via adsorption of a wide range of compounds by adding a white LED and a red LED light that allows us to use this system to directly measure the fluorescence of safranin O in the effluent. Additionally, in order to measure compounds in the ultraviolet spectrum, we procured a spectrophotometer that is also installed in-line after the column reactor.

Third Quarter, 2010

After evaluation of a variety of geomedia analogues, we conducted experiments on three different size fractions of Ottawa sand which will provide comparisons of tracer holdup on grains with identical mineralogy, but with different surface areas. Heating of the simulated geomedia has resulted in increased pH along the length of the column. We have determined that modifying the flow solution by raising the ionic strength through the addition of calcium/sodium salts and tetraethyl orthosilicate (TEOS) has eliminated the pH increase.

Fourth Quarter, 2010

No further changes were made to the reactor during this quarter. This task is 100% complete.

Year 1, Subtask 1.2: Conduct Search for Candidate Sorbing EGS Tracers

Among the reversibly sorbing candidates that we have identified are the same cationic (positively charged) compounds used in groundwater sorption work, which sorb due to a charge that is opposite to that of the negatively-charged reservoir rock. Such compounds include ions such as Li^{+} and Sr^{++}, which are desirable since they are naturally occurring only at very low concentrations in reservoir water. Other candidates include cationic fluorescent compounds such as alcian blue. Other compounds that we have identified are the strongly sorbing scale inhibitors such as polycarboxylates, polyacrylates, and polymaleic anhydrides have been shown to sorb strongly but still reversibly within geothermal wellbores and formations.

Our initial search for candidate sorbing EGS tracers served to identify several for screening. Methylene blue is a common dye that is used in the construction & drilling industries to measure cation exchange capacity and has the promising property of endothermic adsorption onto perlite. Tinopal is a thermally stable compound that has had breakthrough curves that potentially indicated sorption. Rhodamine WT has been used in near-surface interwell tests and has been shown to be reactive based upon its breakthrough curve relative to conservative tracers. Another dye that we will be screening is Alcian blue because it is a 'hard' cation (small volume to charge ratio) that we think may help to increase sorption at higher temperatures. Finally, we have completed installing equipment and developing methods to measure ionic cations with our HPLC system and will screen for sorption of cations like Li & Sr at elevated temperatures.

Method development for the analysis of rhodamine WT with the HPLC was conducted, including separation of two distinct isomers. This isomer separation will allow us to examine the thermal stability of individual isomers and potentially provide an economical reactive tracer with two molecules that have similar diffusivities, but possibly different thermal stabilities.

We obtained samples of some of the other fluorescent dyes that we will examine for stability and retardation at temperature relative to a conservative tracer: Safranin O and Alcian Blue, as well as Methylene Blue, Tinopal CBS, Sr, and Li.

Erioglaucine (blue 5), pyridine, and acetonitrile were identified as potential thermally stable and reversibly sorbing tracer candidates. Autoclaved Rhodamine WT samples analyzed on the HPLC indicated that there is a difference in the thermal stability of its isomers. The para isomer, as identified by Vasudevan et al, 2001, had a greater thermal stability under the conditions tested. Initial thermal stability testing in the autoclave has been accomplished for pyridine, indicating thermal stability up to 300° C.

This subtask is 100% complete. However, additional candidate sorbing tracers will be studied throughout the duration of the program.

Year 1, Subtask 1.3: Conduct Sorption Screening Tests

We performed initial flow tests up to 1200 psi & 300°C. We will begin testing using clinoptilolite as the analogue geothermal reservoir medium. In order to best utilize traditional flow models, we have been carefully preparing the porous media with which we will screen candidate sorbing tracers. The material was crushed to provide a size fraction that is less than 1% of the column diameter by sieving the zeolite material through a 150 µm screen and retaining it on a 120 µm screen.

A preliminary column test (at 25° C) was run with rhodamine WT to provide a baseline conservative tracer measurement of the pore volume, as well as work out methodology and timing for the experiments. The resulting samples have almost all been analyzed, providing a partial breakthrough curve shown in Figure 2. There was significant holdup of the rhodamine WT by the adsorbing media as well as an obvious difference between the adsorption of the two fluorescing species of rhodamine WT (labeled RWT Peak 1 & RWT Peak 2 in Figure 2).

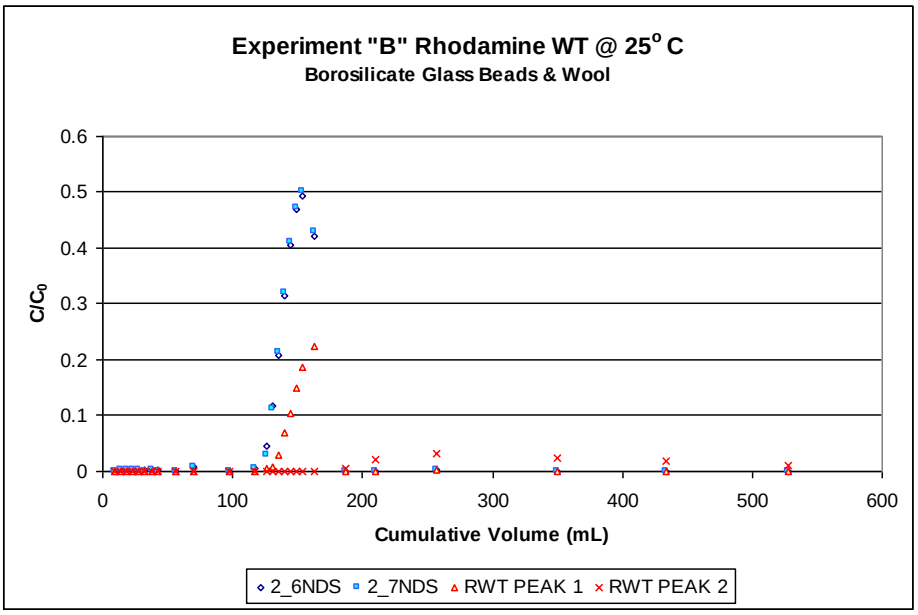

Figure 2. Preliminary low temperature column sorption test.

It proved too difficult to retain the zeolite within the column, so small particles of silica gel were used instead. But stabilization of the media was unsuccessful and initial tests were done with a media constructed of glass beads. Since at elevated temperatures Rhodamine WT hold up within the column was not evident at the higher concentrations required for the absorption detector and column reconstruction was necessary because of thermal decay of column o-rings, the column media was changed to glass wool and coarse Ottawa sand.

Alcian blue, Safranin O, methylene blue, erioglaucine, pyridine, and Rhodamine WT were experimentally tested in the laboratory reactor. Erioglaucine, pyridine, and Rhodamine WT did not show significant hold up at elevated temperatures with deionized water as the eluent. So, they were tested with the pH raised to 8.5. Preliminary examination of the breakthrough curves of the food coloring based tracers (Figure 3) indicates that adsorption can be induced at elevated temperature by raising the pH. The other more strongly cationic candidates would not elute until the use of a pH 3 flush solution.

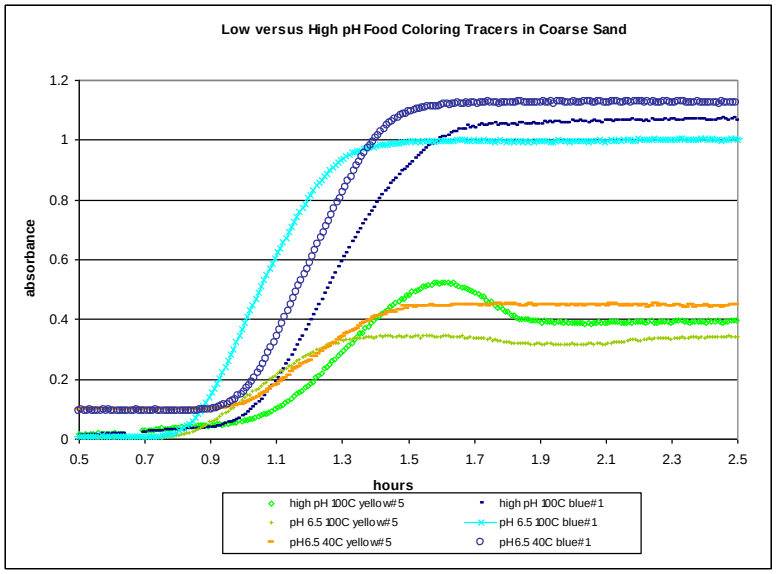

Figure 3. Elevated pH-induced hold up at 100 ^{o}C

This subtask was completed on schedule during the first year of the project. However, it continues under Phase 2.

Year 1, Subtask 1.4: Develop a Model for Inverting Sorptive-Tracer Data to Calculate Interwell Fracture Surface Areas

A numerical model was successfully modified to allow heat transport to be simulated (in addition to mass transport) in either single-well or cross-hole tracer tests. This capability was added to allow either diffusion coefficients or sorption parameters to be specified as a function of temperature, which may vary in EGS reservoirs by as much as 200C. Such variations could cause as much as five- to six-fold differences in diffusion coefficients of the same tracer in hot and cold parts of the reservoir and potentially similar differences in sorption parameters in different parts of the reservoir. The heat transfer features of the model were tested for several known simple cases and found to provide accurate solutions, although the time step size had to be reduced significantly relative to mass transport problems in the same geometry because of the much greater rate of thermal diffusivity relative to mass diffusivity. The capability to account for the temperature dependence of diffusion coefficients and sorption parameters will be added to the model in upcoming quarters (right now only temperatures are calculated; tracer properties are not directly tied to these, although this should be a relatively easy enhancement).

Year 1, Subtask 1.5: Develop a Numerical Model to Calculate Fracture Surface Areas from Injection/Backflow data

At EGI, Scott Fayer:

Second Quarter, 2010

A model was developed to calculate fracture surface area based upon the thermal decay of tracers having well characterized thermal decay kinetics. A paper was written by Fayer et al. (2009) for submission on May 11 for presentation at the 2009 GRC annual convention.

The expanded thermal decay model built last quarter was used to generate return curves for a hypothetical geothermal system. These curves represent a method for determining fracture spacing when compared to actual field returns curves. We are currently in the process of collaborating with other labs who have gained interest in this project to continue to build in features, and to compare against other code bases.

After further refinements, presentations of the model were made at the TOUGH2 Symposium in Berkeley, CA and at the annual Geothermal Resources Council conference in Reno, NV.
Fourth Quarter

Scott completed a M.S. thesis within the Department of Chemical Engineering at the University of Utah on the subject of a numerical method to estimate fracture surface areas in near-wellbore geothermal formations using thermally decaying tracers. He will defend his thesis during the first quarter of next year.

At LBNL, Karsten Pruess and Christine Doughty:

First Quarter, 2010

We started a literature survey on single well injection-withdrawal (SWIW) tests in fractured media that involve reversibly sorbing tracers. We are focusing on parameter sensitivities, especially the sensitivity to fracture-matrix interface area.

Second Quarter, 2010

TOUGH2 simulations were run for non-isothermal SWIW tests in fractured-porous media in which temperature plays the role of tracer. Different operational scenarios were explored for the sequence of fluid injection, a subsequent quiescent period, and withdrawal. Results show significant thermal contrast as a function of changes in fracture-wallrock surface area. A particle-tracking approach is being devised to compare the effect of reversibly sorbing tracers to the thermal effects.

We performed numerical simulations to evaluate the ability of thermal single-well injection-withdrawal tests (SWIW) to provide characterization data for fracture systems intercepted by an injection well. Results of this work will be presented in a paper to be submitted to the upcoming Stanford geothermal workshop.

Third Quarter, 2010

Numerical simulations with TOUGH2 for the injection phase of a non-isothermal single well injection-withdrawal (SWIW) test were compared with a closed-form analytical solution by Lauwerier (1955). Excellent agreement was obtained, see Figure 4.

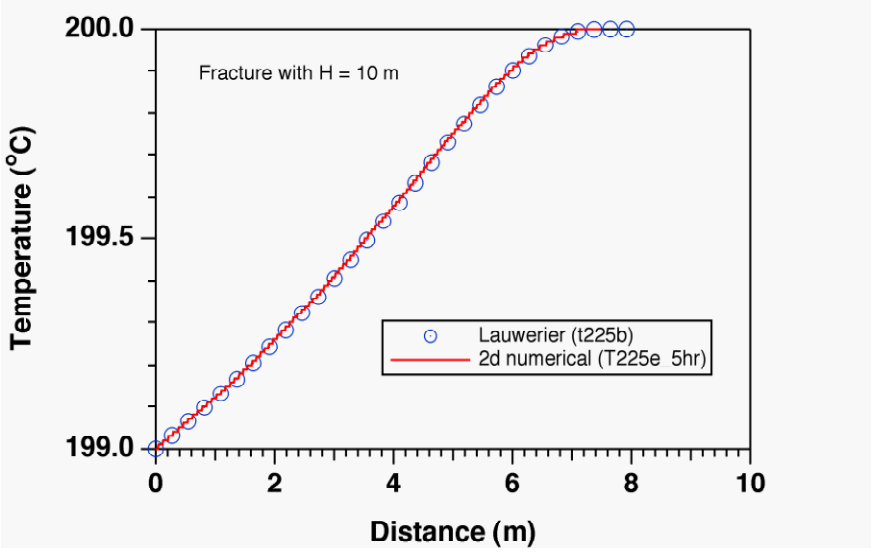

Figure 4. Temperature profiles in a linear fracture after 5 hours of non-isothermal injection, comparing the analytical solution of Lauwerier with a numerical simulation.

A summary paper on "Tracer Methods for Characterizing Fracture Stimulation in Engineered Geothermal Systems (EGS)" was submitted and presented at the DOE geothermal review, May 18-20, 2010.

Fourth Quarter, 2010

The preliminary SWIW thermal model is complete. Plans are pending for testing the concept in a field experiment.

Year 1, Subtask 1.6: Find and/or Synthesize an Appropriate Fluorescent Tracer for Downhole Fluorimetry

The original fluorimeter design required that the tracers must fluoresce within the narrow window of 800-1000 nm. This is because the attenuation of neighboring visible light is too great over the target length of 9,000 ft of optical fiber. Likewise, any longer wavelength fluorescence is in appropriate for the silica-based CCD camera that will be used as a detector. Two near-IR fluorescent compounds were therefore identified: DTTCI and IR-125. The former is cationic, which may present problems (for this application) due to sorption. The latter is anionic and also likely more thermally stable.

The new fluorimeter design (see Task 3, Subtask 2 below) side steps the problems associated with deploying 9,000 ft of optical fiber. It is a wireline tool that promises to be much more durable and much more easily deployed than the optical fiber tool. The tracers that were originally designed for the long path lengths of optical fiber will still have application for the wireline tool. These are the newly synthesized PbS quantum dots that are described in the following section.

Commonly used high-temperature-stable tracers are based on organic dye molecules with emission in the ultraviolet range of the electromagnetic spectrum. Since this range is readily spectrally polluted by many naturally occurring reservoir contaminants, high-temperature-stable tracer species with emission bands at larger wavelengths (visible and near infrared) are highly desired. In particular, near infrared-emitting tracers (at wavelengths around 800-1000 nm) are of great interest due to reduced background absorption, fluorescence and light scattering in this range. Unfortunately, near infrared-emitting tracers based on organic dye molecules suffer, in general, from aggregation, photobleaching, and low fluorescence quantum yields. These obstacles, however, should be overcome by using semiconductor nanocrystals ("quantum dots") as the emitting tracer species. Quantum dots are small crystallites (1-10 nm in diameter) of semiconducting compounds with tunable electronic and optical properties and high fluorescence quantum yields.

Initial efforts focused on synthesizing CdSe-based quantum dots that are water-soluble and have tunable fluorescence in the visible. For this, a synthesis method was adapted from literature reports that results in CdSe quantum dots with citrate molecules attached to their surface, rendering them water-soluble. The synthesis conditions were varied to fabricate quantum dots with different sizes (3-5 nm in diameter), resulting in green, yellow and orange emission colors. Furthermore, so-called core-shell structures were synthesized by covering the CdSe quantum dots with a thin shell of crystalline CdS. This extra shell minimizes surface defects of the CdSe core crystallite and thereby enhances the fluorescence quantum yield. Current efforts focus on optimizing these core-shell architectures to produce water-soluble quantum dots with fluorescence quantum yields approaching those of conventionally used organic dye tracers.

In parallel to CdSe-based quantum dot synthesis we have also began to fabricate PbS quantum dots. The advantage of PbS is an inherently smaller electronic band gap, which shifts electronic and optical properties of PbS quantum dots into the near infrared range. So far we have successfully fabricated fluorescent PbS quantum dots with emission bands centered between 900 and 1000 nm. A current limitation of PbS quantum dots, however, is that synthesis routes require very hydrophobic (oily) conditions and as a result the synthesized quantum dots are insoluble in aqueous media. A central focus of current and future research is therefore to extend the water-based synthesis route that we successfully applied for CdSe quantum dots to PbS quantum dots.

Initial studies showed that CdSe and PbS-based quantum dots can be made water-soluble and display tunable fluorescence emission in the visible and near IR range, including the important 800 to 1000 nm wavelength range. These initial results are very encouraging and studies in the last funding period focused on up-scaling quantum dot production. Up-scaling of quantum dot production will be of great importance for field testing in an injection/backflow test in an EGS wellbore. However, up-scaling of conventional synthesis methods is generally a problem due to the high reaction temperatures (230-350 °C), which lead to the formation of temperature gradients in large reaction volumes. In addition, due to the fast nucleation and growth kinetics at high reaction temperatures injection of precursors has to occur very rapidly to avoid products with large unwanted size polydispersity.

We have recently developed a low-temperature (50-130 °C) synthesis route for the fabrication of high-quality colloidal nanocrystals. We recently were able to demonstrate first results, showing that the lowered synthesis temperatures allow up-scaling of CdSe quantum dot production. Up-scaling is pursued in two steps: 1) Increasing the concentration of produced quantum dots per reaction volume and 2) increasing the reaction volume per run. So far we focused on step 1 and were able to increase the concentration of quantum dots by a factor of 1000. This was accomplished by optimizing the ratio of quantum precursor components to surface-stabilizing ligands. Importantly, up-scaling did not lower the quality (structural and optical properties) of the synthesized CdSe quantum dots. The next steps will be to 1) continue optimizing the reaction parameters to further increase the production and 2) build a synthesis set-up that will enable increase of the reaction volume from currently 10-20 milliliters to several liters.

We optimized up-scaling of our low-temperature synthesis procedure for high-quality semiconductor nanocrystals ("quantum dots"). Up-scaling is pursued in two steps: 1) Increasing the concentration of produced quantum dots per reaction volume and 2) increasing the reaction volume per run. The ultimate goal is to reach synthesis batch levels high enough to directly use quantum dots as luminescent tracers for field testing in an injection/backflow test in an EGS wellbore.

In the previous funding period we made significant progress in tuning synthesis parameters, resulting in an increase in yield-per-synthesis-run by a factor of about 1000. Since then we focused on optimizing the optical properties of the quantum dots synthesized at such high yields. We made significant progress and achieved quantum dot qualities in terms of optical and structural properties equal to those synthesized at low concentrations and/or high temperatures. This is also evidenced in the narrow optical absorption and emission peak features (with full-width-at-half-maximum values as low as 30 nm) shown in Figure 5.
The second main aspect of our current research is aimed towards up-scaling the overall reaction volume. For this, we built a new quantum dot synthesis set-up that will allow increase of the per-batch reaction volume by a factor of up to 200 (from the current 20 mL to about 4 L). Figure 6 shows a photograph of the set-up and we are currently in the finishing stages of linking the various synthesis apparatus components and starting with quantum dot synthesis runs at these high reaction volumes.

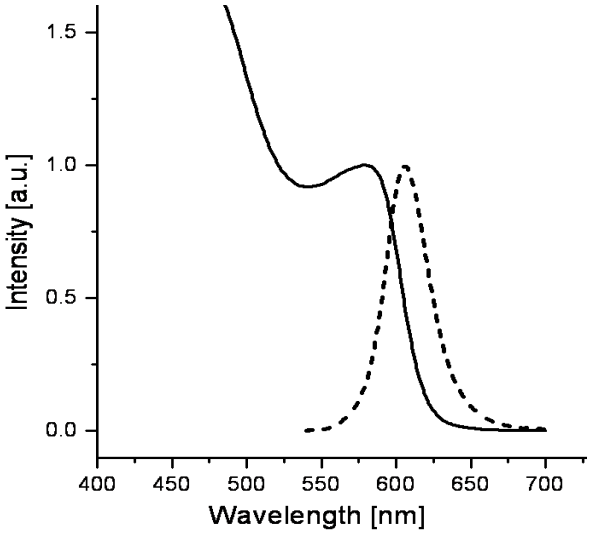

Figure 5. *UV-vis absorption (full line) and photoluminescence emission (dotted line) spectra of CdSe nanocrystal quantum dots produced at low reaction temperatures (130 C) and high yield (1000 fold increase).*

Figure 6. Photograph of high-reaction-volume synthesis set-up for up-scaled quantum dot production.

This subtask was completed on time during the first year of the project. Further research on quantum dot nanocrystals is being conducted under a separate DOE grant. Furthermore, conventional geothermal tracers that fluoresce in the visible (e.g. fluorescein) will be more than adequate for uses within the borehole fluorimeter as described below.

Year 1, Subtask 1.7: Design and Fabricate a Field Fluorimeter for Measuring Tracers Downhole

Background

The original design of the field fluorimeter was analyzed and considered to be too risky to pursue. It was to consist of a spectrometer (complete with fiber optics, a CCD camera and a laser light source) located at the surface near the wellhead. One of the problems identified with the design, however, was the need to mount the spectrometer on the coiled-tubing drum that will be used to deploy the fiber optic cable. The optical fiber would be deployed within the coiled tubing in order to protect it from the harsh environment within the wellbore. However, there are many problems associated with deploying 10,000 ft of optical fiber—even if that fiber is enclosed within capillary tubing. Not only is the fiber quite expensive to deploy in this fashion, any break in the fragile fiber would of course render the tool inoperable. Given these risks, an alternative design was developed that will allow for the deployment of the spectrometer downhole on a wireline, thus avoiding the problems associated with deploying optical fiber over long distances within EGS wellbores. The drawback of this approach is that the tool will now have to be designed and fabricated in such a fashion that it can be deployed downhole and through a lubricator, limiting the diameter of the tool to about 2.6 inches. As described below, excellent progress is being made towards the design and fabrication of the tool.

Accomplishments

First Quarter, 2010

A meeting was held with representatives from the high-temperature tool groups at Sandia National Laboratory (Doug Blankenship and Joe Henfling), the USGS (Steve Hickman), and DOE (Eric Hass and Bill Vandermeer), Perma Works (Randy Normann) and others for the purpose of establishing collaboration with these groups in anticipation of a design review for the borehole fluorimeter/flowmeter. Work continues on the design of the borehole fluorimeter/flowmeter in anticipation of that review.

Pete Rose, Mike Mella, and Steve Olsen visited the laboratories of Steve Hickman at the USGS, Menlo Park, CA to discuss challenges and design features common to the DOE-funded high temperature borehole televiewer. Steve donated several public domain files to us regarding the design and fabrication of the televiewer. It was decided that a design review would be necessary before initiating the fabrication of the borehole fluorimeter (see Figure 7 for most current design). In anticipation of that design review, Pete Rose and Daniel Bour (AltaRock Energy) visited Dan Bebout at Welaco, Bakersfield to discuss collaboration with this company who will most likely be the first to test the borehole fluorimeter in a geothermal wellbore.

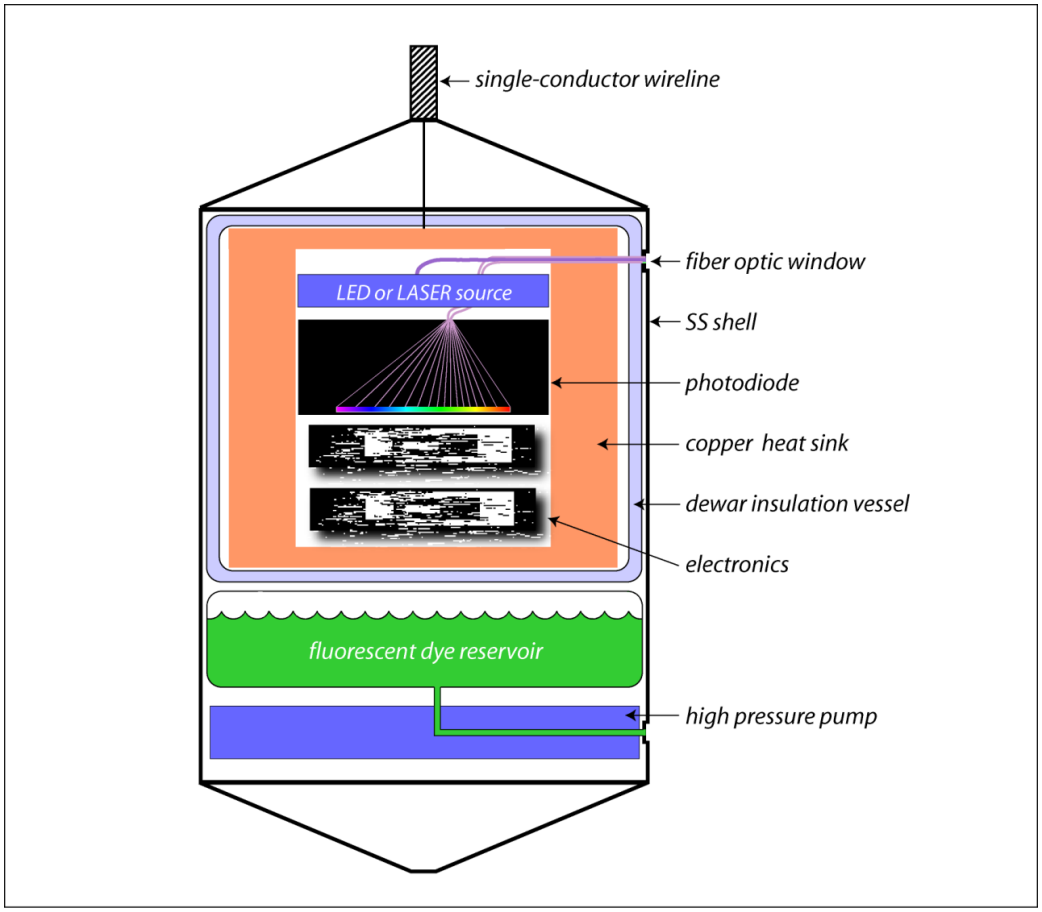

Figure 7. Sketch of the wireline fluorimeter.

Second Quarter, 2010

The physical requirements of deploying the tool in a geothermal well were investigated. The flow conditions and temperature effects were considered to help shape the design of the tool. In particular the flow conditions will help determine the tool length and the temperature conditions will help determine what type of electrical components need to be specified.

Flow Conditions

Critical to the design is the mixing distance needed if tracer is introduced at one end and a measurement is taken at the other end of the tool. With assumptions of an 8 inch well bore diameter calculations were made at several volumetric flow rates to determine the distance needed to achieve 99% axial mixing in turbulent conditions. Figure 8 shows plots of mixing length vs. flow rate.

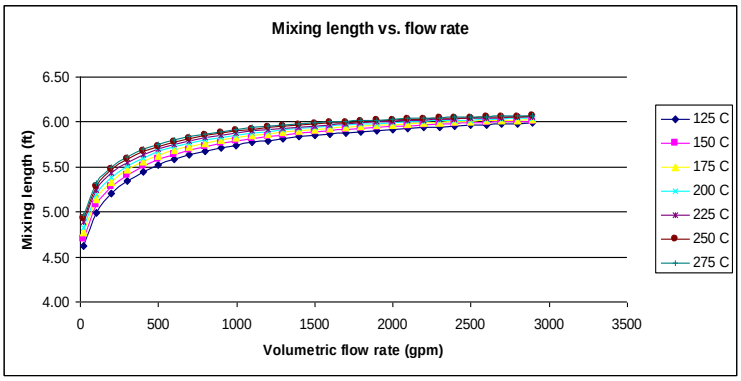

Figure 8. Mixing lengths required for complete axial mixing vs. flow rate.

From the plot one can see that the injection source and detection must be about 6 feet apart to safely approximate complete mixing even at very high flow rates (high velocities). The back mixing effect present in turbulent flow rates and present in most geothermal wells will ensure well mixed tracer provided the tool is longer than 6 feet. The use of the tool at laminar flow conditions will be a challenge because of the lack of natural mixing. Figure 9 shows tracer concentration across the wellbore 8 feet from the injection source at different flow rates. As evident from the plot, the tracer concentration would vary significantly from the borehole walls to the center line.

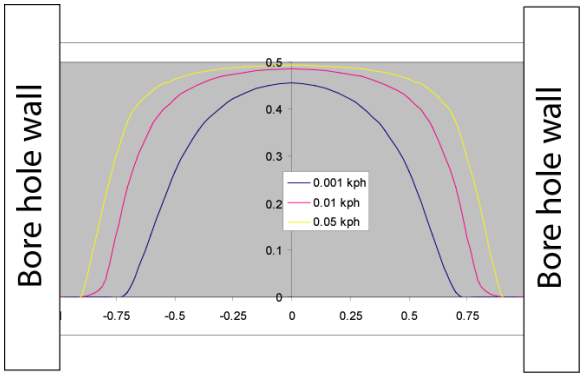

Figure 9. Tracer concentration profile across the wellbore at a distance of 8 feet from the injection point.

Operation at laminar flow regimes will require addition a mixing device to provide for even mixing across the wellbore. Two of the ideas to help induce mixing include adding recirculation jets to induce back mixing or adding a mixing brush on the outside of the tool. Both of these options are depicted graphically in Figure 10 below.

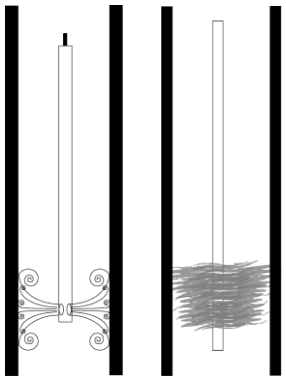

Figure 10. Cartoon representation of mixing devices, recirculation jets on the left and mixing brush on the right.

Temperature Effects

Perhaps the biggest challenge of deploying a tool in a geothermal wellbore is the high working temperature. From earlier discussions with others who have made tools, the need to encase the tool in a Dewar style heat shield with a heat sink to mitigate temperature rise was quickly realized. From communications with heat-shield-designer Mitco, estimates were made as to what the internal temperature of the tool would be at geothermal conditions. With a stainless steel heat sink and an assumption of 5 watts of power dissipation within the tool a plot of internal temperature versus time for several temperatures was produced and is shown below as Figure 11. Included in the plot are two lines that represent 85°C and 125°C. These two lines are significant because they show the temperatures at which traditional electronics (85°C) and automotive class electronics (125°C) will fail. The price increase to move from traditional to automotive grade electronics is not significant and will most likely be the components that are used provided all the necessary components are available in that class. Any electronics beyond these temperatures will need to be high temperature components, representing a very large cost difference. These components can typically operate near 180°C. At present the plan is to use lower grade electronics in the prototype tool and then upgrade to high temperature components as the budget allows.

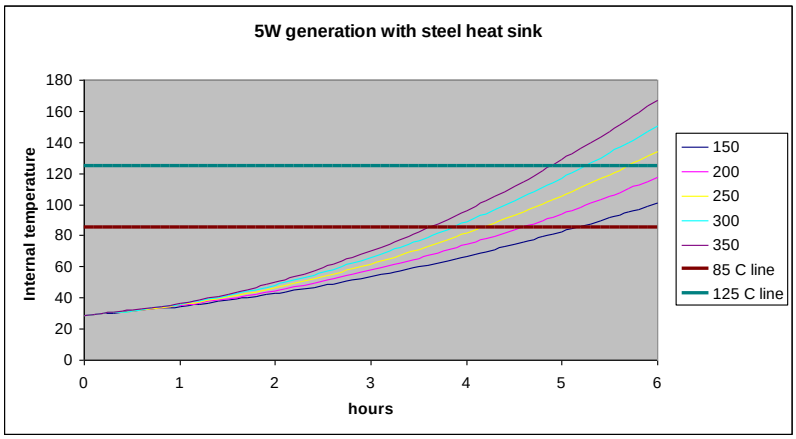

Figure 11. Expected internal temperature vs. time at various external temperatures.

From the plot it can be seen that use of automotive class components will allow for about 5 hours of operation at temperatures up to 300°C. To get to six hours of downhole operation at temperatures greater than 250°C it would appear that high temperature electronics would be called for.

In an attempt to try and elongate the time that can be spent in the well, one of the options that was looked at was phase-change cooling. This entails the use of a low melting temperature alloy sealed inside the heat sink. The idea is that thermal energy would be expended in the phase change of the alloy and could delay temperature rise. The low melt alloys are typically made up of Bi, Pb, In, and/or Cd in different ratios depending on the melt temperature desired. For comparison, calculations were performed with a low melt alloy, AIM 70, and the results were plotted as seen in Figure 12 below.

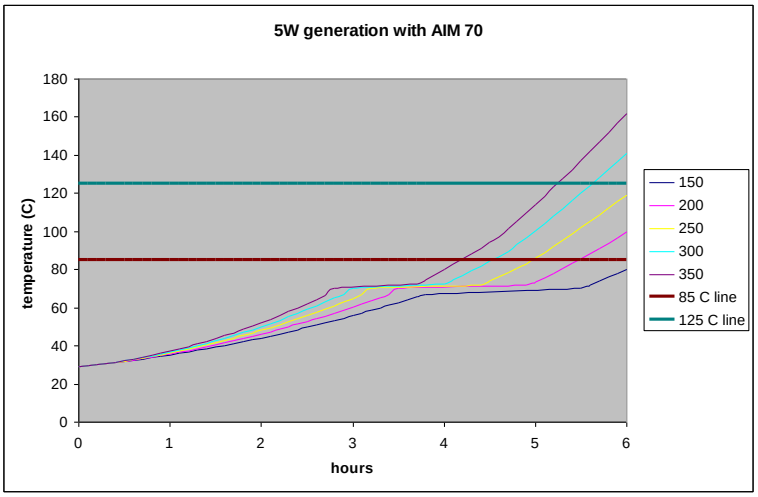

Figure 12. Expected internal temperature vs. time with heat sink that includes phase change material.

From the plot it would appear that the phase change material would elongate the tool's time in the well by about 30 minutes to an hour depending on the temperature. It is unlikely that we would opt to use this strategy in a prototype tool but it may be part of a future tool. Overall it appears that the main challenges for temperature management include limiting internal heat generation and designing with higher grade automotive components.

Visit to Welaco

Peter Rose, Mike Mella and Steve Olsen visited the office of Well Analysis Corporation (Welaco) in Bakersfield, CA for an informal design review and discussion. The trip was very productive as Welaco was very interested in the project and had several very useful tips on the practical design of the tool. Several of the components that they suggested and strategies that they discussed will likely be incorporated in the tool. Welaco was also able to verify that most of the ideas that we had will work in a geothermal environment. Welaco also offered the use of some of their older tools and equipment for preliminary tests.

Current Design

With the knowledge gained from the meeting with Welaco and the flow and temperature effects that can be expected, the preliminary design was updated. A cartoon sketch of the current tool design is shown below as Figure 13 with a close up look at the optical fiber bundle that will serve as excitation light delivery and emission light collection.

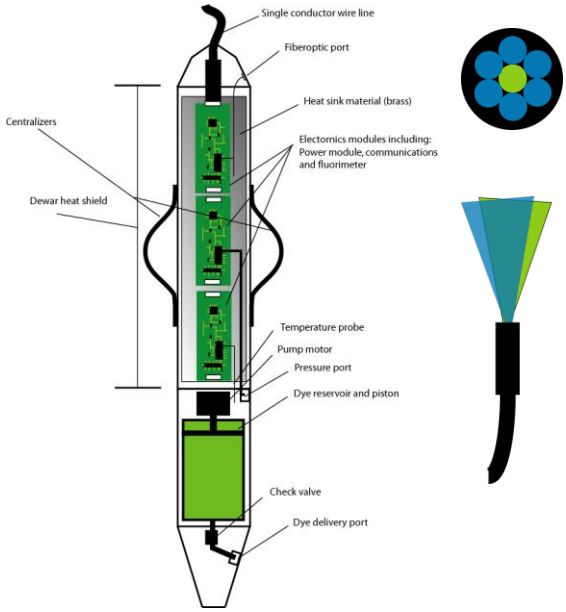

Figure 13. Cartoon sketch of purposed tool and fiber optic bundle.

Electrical Components

An overview of the tool's electrical components is summarized below.

Power Supply

The power supply will consist of two components. The first is regulation of the power delivered at the surface and the second is the regulation of power at the tool. The power supply at the surface will take poorly regulated AC power from the surface and convert it to DC power that will be sent down the wireline to the tool. The power supply at the surface will need to regulate voltage based on the power consumption in the tool and the resistance that is encountered in the line. Figure 14 below shows the relationship of voltage to power consumption with different line resistances encountered. The tool side power supply will be able to give real time information to the surface power supply to determine how much voltage to send.

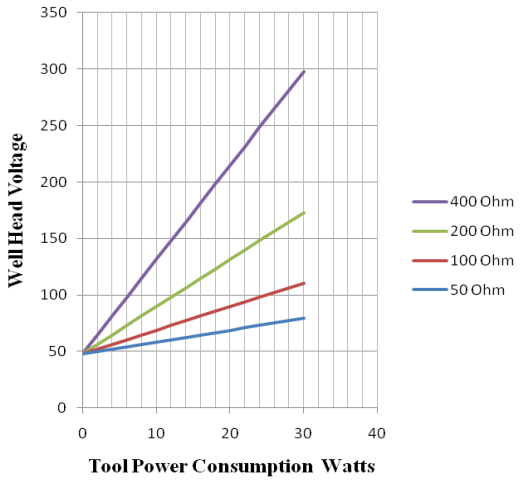

Figure 14. Well head voltage vs. power consumption with different line resistances.

The tool side power supply will involve input protection against over voltage and a DC to DC conversion to supply DC power at 12 volts to the various components. The power supply will also make use of real time supply optimization to request the right amount of power from moment from the surface supply. This should help to reduce the amount of heat that would be dissipated in the tool. A second strategy that will be used will be turning unused components off when they are not needed. For instance when the tool is on the way to the zone of interest to log only intermittent temperature and pressure readings may be desired, the other components can be turned off to reduce internal heat generation.

Light Source and Detector

The light source is a high efficiency blue LED that will provide excitation at 465nm and will operate at 125°C. The LED will be coupled to a collimator which will be connected to the fiber optic source. The LED operation strategy will include modulation to effectively subtract dark current as well as sampling the light to get an accurate indication of intensity out.

The detectors that have been considered include avalanche photodetectors (APD) and photomultiplier tubes (PMT). The advantages of the APD are low cost, ruggedness and a small electrical footprint. The disadvantages include low sensitivity and inability to operate at high temperatures, the limit appears to be around 50°C. The PMT by comparison has several orders of magnitude better sensitivity and can operate at temperatures up to 175°C. The disadvantages of PMT include larger electrical footprint, high voltage (low current) operation and increased cost. At this point we are designing to using a PMT instead of an APD.

Pressure, Temperature and Inclination

The temperature of the outside well environment and internal tool environment will be closely monitored throughout the test. A platinum RTD will be placed through one end of the tools sub assembly and then a second RTD will record temperatures within the tool body. Because some of the components will cease to work at high temperatures and can also be destroyed at high temperature a close watch on internal temperature will be necessary.

Pressure measurement is an essential part of any well log. Pressure will be measure using a high temperature piezoelectric pressure transducer. Pressures will be obtained by using a standard pressure filter port through the tools bottom sub assembly.

An accelerometer will be included in the tool to give some idea as to the inclination of the tool. The accelerometer will be able to accurately measure the pull of gravity and determine from its own orientation what the orientation of the tool is. These components are also capable of 125°C operation.

Tool Control and Data Transmission

In general much of the tool control will be located within the software being run at the surface monitoring station. The tool will be able to receive instructions from the surface and carry them out. Some of the things that will be controlled will be the on/off of individual components, the LED intensity, the PMT gain and the flow rate of the dye pump.

Field Programmable Gate Arrays (FPGA) will be utilized in the communication up and down the wireline. The FPGAs will allow for flexible signals, in this case data will be packetized and sent with internal validation. The tool will control which signals get sent based on a prioritization system and will be controlled by a CAN bus within the tool.

Third Quarter, 2010

Mike Mella and Steve Olsen visited the offices of Sandia National Labs high temperature tool division and PermaWorks, makers of high temperature tools, in Albuquerque. At both locations an informal design review was presented. In each case the reviewers were positive of the work being done and had good suggestions for components and pieces to use.

The only change from the design reported last quarter is the movement of the LED light source and the photo multiplier tube (PMT) to the ends of the Dewar heat shield. These two components can withstand temperatures of 150°C and 175°C, respectively, and can therefore be placed in the section of the heat shield where it is anticipated it will be hotter. The other electronic components have been designed for maximum operating temperatures of 125°C and will be within the center of the heat shield. The LED and PMT will be separated from the other electronics by a PEEK, or similar, isolator allowing wires to pass through but limiting thermal contact between the different sections of the heat shield.

Fourth Quarter, 2010

Steve Olsen, the electronics engineer who was responsible for the design, fabrication and testing of the electronic components, died during the previous quarter. We are in the process of finalizing contractual agreements for his replacement, who is Bruce Boyes of Systronics, Inc. Bruce is a very capable electronics engineer who is rapidly coming up to speed with the project. He will present a design of the tool at a design review to be held in the first quarter of 2011.

Year 2

Year 2, Subtask 2.1: Continue Sorptive-Tracer Screening Tests

Second Quarter, 2010

Methylene blue was tested in both the simulated geothermal reservoir for sorption and in our autoclaves for thermal stability. Elution through the heated reactor column did not occur despite attempts at temperatures up to 270° C at low pH and the analysis with HPLC has not been successful, yet. Because of the strong sorption indicated by the lack of breakthrough from the heated reactor column, we have decided to not further investigate at this time this potential candidate. Initial tests with Alcian blue resulted in similar results as with the methylene blue, but thermal stability tests have not been done in the autoclave, yet.

Safranin O, erioglaucine, and tartrazine were heated in autoclaves in the absence of oxygen to assess their thermal stability. Safranin O shows indications of having a half-life at 140° C of over 5 days, but additional tests need to be performed at different temperatures (Figure 15). Erioglaucine's half-life at 140° C of over 4 days (Figure 16) while the half-life of tartrazine at this temperature would be less than 2 days (Figure 17).

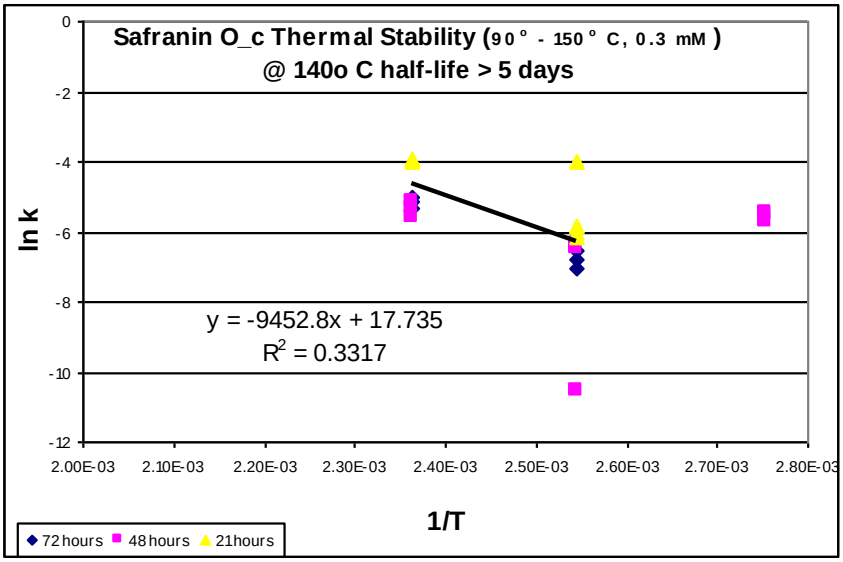

Figure 15. Arrhenius equation rate constant plot for safranin O.

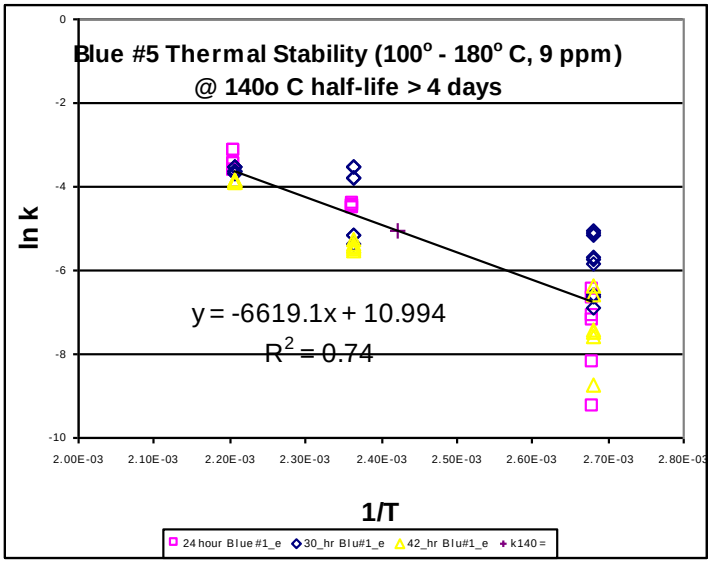

Figure 16. Arrhenius equation rate constant plot for erioglaucine.

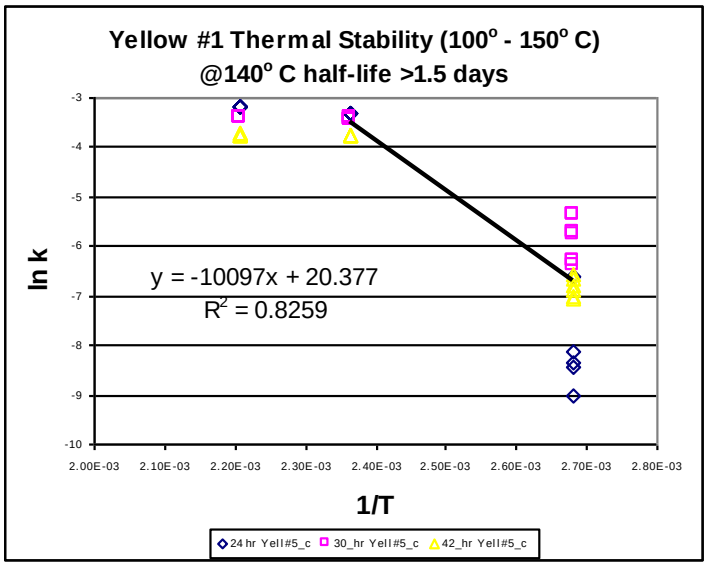

Figure 17. Arrhenius equation rate constant plot for tartrazine.

Pyridine was screened for sorption in the heated column at 100° C. At this temperature there was no indication of significant sorption as indicated by a ratio of ~1 between the first moments of the breakthrough curves for the conservative and 'reactive' tracers (retardation factor). We ran an experiment with tinopal cbs-x as the reactive tracer through the same sand as used with pyridine experiment at 25° C. At this temperature there appeared to be significant hold-up of the tracer. Using a linear best-fit model to estimate the time of 50% normalized concentration for both the reactive and conservative tracers' input pulse results in a retardation factor of 2.7. While for the flush step the ratio of the 1st moments of time vs. concentration results in a

retardation factor of only 2, but still indicative of its being a potential candidate since our lab has previously found that tinopal cbs-x is thermally stable up to 200° C.

Initial experiments with Safranin O have indicated that it shows promise as a reactive tracer. It exhibits fluorescence which will allow a lower detection limit than the candidates detectable via only absorption. The first flow experiment was through a column of only 3 mm diameter glass beads and glass wool and there was no holdup of the safranin O. In order to test it on more typical and natural media the column was filled with sand and flow experiments were conducted. Initial tests resulted in no breakthrough, but when the pH was lowered there was eventual breakthrough (Figure 18).

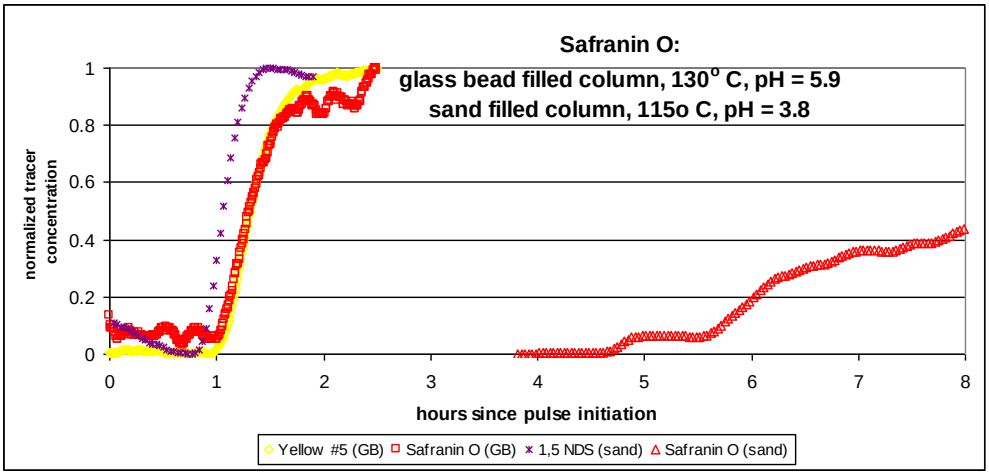

Figure 18. Breakthrough curve showing hold up of safranin O by sand at 115°C.

Third Quarter, 2010

During the third quarter of 2010, a series of step input sorptive-tracer screening tests were performed. Initially, a media of glass beads was tested with safranin O. There was no breakthrough of the tracer. Measurement of the effluent pH suggested that dissolution reactions were increasing adsorption above the practical limits. The food colorings, yellow #5 & blue #1, were eluted through the column filled with sieved Ottawa sand between 600 and 500 µm (geometric mean of 548 µm) at temperatures of 75°and 125° C. While there was only minor holdup (retardation factor of 1.02) of the blue #1 at 125 degrees (Figure 19), the experiment demonstrates that yellow #5 behaves in the column similarly to the 1,5 naphthalene disulfonate. Since the yellow #5 has significantly lower thermal stability, but behaves conservatively it may prove useful as a low temperature geothermal reservoir temperature probe.

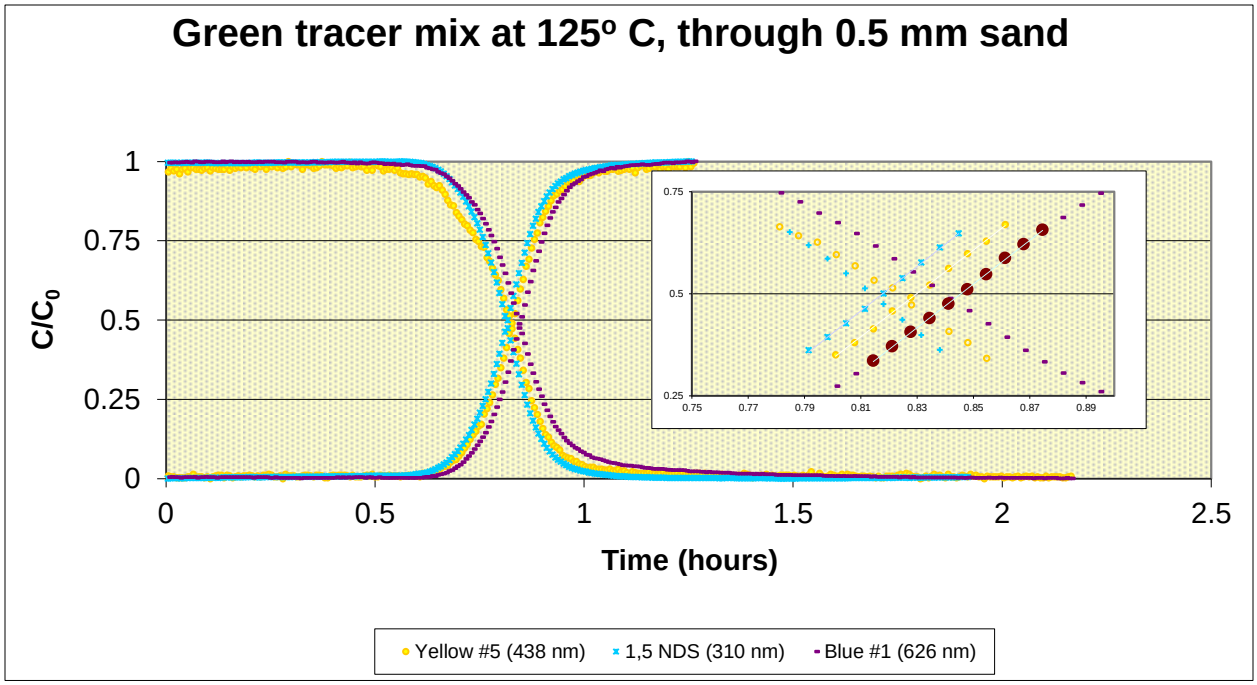

Figure 19. Incoming and outgoing breakthrough curves for triple tracer solution. Inset graph shows the linear portion of the breakthrough curves. The NDS elutes slightly earlier than the yellow #5 due to having its detector ahead of the yellow #5's.

After adjusting the solution chemistry with the salts and TEOS, the effluent pH remained below 8 and a series of experiments were conducted with two types of safranin on the 0.5 mm fraction sand. Experience with the interpretation of the breakthrough curves from these experiments has led to the adoption of the technique of comparing the median residence times of the tracers. This technique has proved relatively rapid and accurate without being strongly affected by instrument noise. In summary, this involves linear interpolation of a normalized concentration of half the response from the input concentration as determined from the response after the step input is eluting.

Comparison of the adsorption by safranin O versus safranin T (Figure 20) indicates that the safranin T would be a better candidate based on it having a smaller retardation factor on the Ottawa sand, 2.2 and 1.4, respectively. The two types of safranin differ only in that safranin T has a third methyl group attached to the phenyl group. Having less retardation in a geothermal aquifer, as long as there is still retardation, will be beneficial in terms of sample collection intervals and the overall samples required to define the breakthrough curve. Additionally, the safranin T is significantly more thermally stable than safranin O. Initial thermal stability tests of heating solutions in ampoules for 3 days in autoclaves resulted in over a third of the tracer remaining at 250° C and over 90% left from the 180° C treatment.

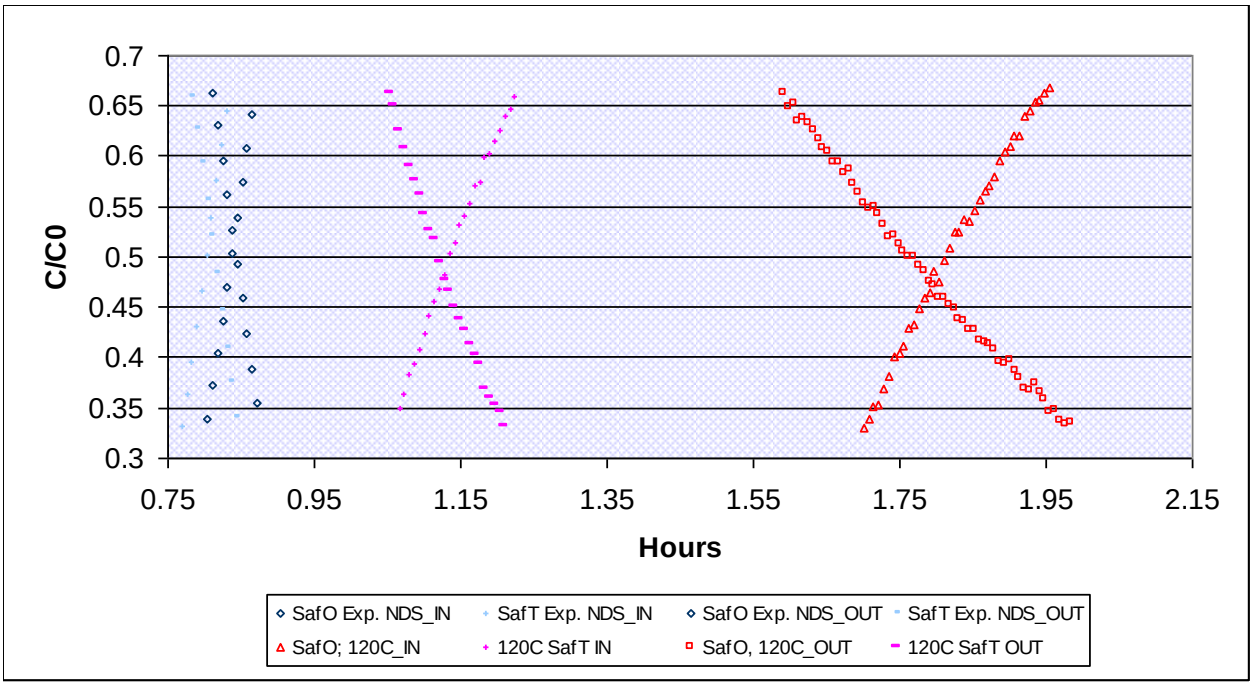

Figure 20. Comparison of the median residence times from breakthrough curves through 0.5 mm Ottawa sand at 120° C. Reactive tracers were safranin T and O and both experiments used 1,5 naphthalene disulfonate as the conservative tracer.

Fourth Quarter, 2010

During this quarter we completed a series high temperature sorbing tracer tests with the simulated geothermal reservoir to examine the response of the reactive tracer by increasing the surface area of otherwise identical media. We sieved Ottawa sand into three fractions: coarse (0.5 – 0.6 mm); medium (0.425 – 0.5 mm); and fine (0.18 – 0.425). Safranin T was eluted through each of these media at three different temperatures: 120, 140, and 160° C. Results from the coarse and medium fraction experiments are consistent with the hypothesis that the reactive tracer would be more retarded by the media with larger surface area (i.e. medium fraction), but the results from the fine fraction didn't corroborate the hypothesis. We are assuming (but testing) that there was preferential flow occurring in the fine fraction that bypassed some of the media as the safranin T was held up less strongly by the media in this column (see Figure 21).

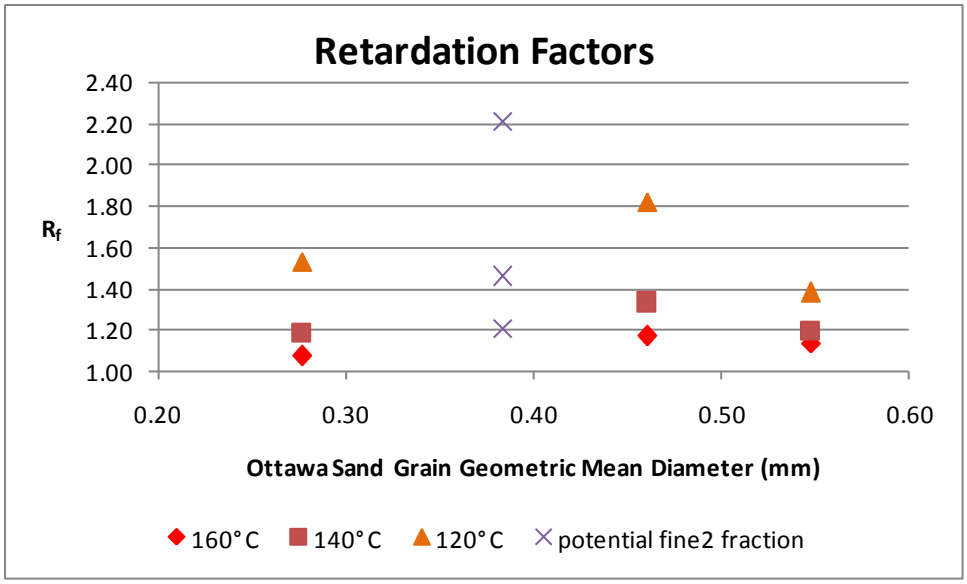

Figure 21. *The retardation factors from the series of experiments conducted at different temperatures and on different particle size fractions of Ottawa sand are plotted against particle size. For illustration purposes only another fraction with a smaller range of particle sizes (fine-2) is included to indicate how the results from the column with the fine fraction are anomalous. A linear relationship between particle size and retardation factor was used to predict the fine-2 result, but a linear model was chosen for ease and is not intended to be inferred without further data and analysis.*

The most significant difference (besides total surface area) between the fractions was that the fine fraction represented a particle size range of 245 µm, whereas the coarse fraction had only a 100 µm range and the medium fraction only 75 µm. This larger range in particle sizes might have resulted in a bed that was not packed as uniformly as the other fractions. To help address this we have separated a fine fraction of Ottawa sand with a smaller range in particle sizes of 355 – 417 µm that we will pack into a column and test safranin T sorbtion at the same temperatures.

Because of the success we've found with safranin T as a reactive tracer in the laboratory, we have begun discussions with geothermal reservoir managers to find a field site to include it in an interwell tracer test. Our initial site has a relatively low temperature; hence the selection of our initial laboratory screening temperatures, but this site may now prove infeasible. Other sites that may become available have higher temperatures, so we are going to test safranin T retardation at higher temperatures in the laboratory during the next quarter.

Year 2, Subtask 2.2: Determine Adsorption Equilibrium Constants for Appropriately Adsorbing Tracers

Third Quarter, 2010

Experiments were performed eluting safranin T through the 0.5 mm Ottawa sand at three different temperatures, 120°, 140°, & 160° C (Figure 22). The reactive tracer was held up relative to the conservative tracer breakthrough at that temperature less at the higher temperatures indicating common exothermic cation exchange adsorption reactions. The retardation factor of only 1.1 at 160° C would still provide a strong enough signal for surface

area measurements, but if it exhibits a linear relationship between the distribution coefficient and temperature the initial measurements indicate that safranin T will not adsorb above 180° C. The three experiments with safranin T do not exhibit a strong linear relationship between medium temperature and retardation factor. The retardation factor at 120° C was 14% larger than measured at 140° C, wheras there was only an 8% decrease when the temperature was increased from 140° C to 160° C. Therefore, we may yet find that it adsorbs sufficiently at geothermal temperatures.

The similarity in slopes between the linear portion of the tracer breakthrough curves during the loading phase and unloading phases (table 1) indicates that the adsorption and desorption reactions are similar. This will allow for the use of the advection diffusion equation with less complicated instantaneous equilibrium assumptions to model the column experiments for distribution coefficient parameter estimation. Software (CXTFIT2) for this has been obtained and model fitting will be initiated during the next quarter.

Table 1. Average Slopes of Linear Portion of Breakthrough Curves

Temp (C)	Conservative Tracer (IN)	Conservative Tracer (OUT)	Reactive Tracer (IN)	Reactive Tracer (OUT)
120	5.3	-5.4	2.0	-2.1
140	5.5	-5.8	3.9	-3.2
160	5.7	-5.9	4.2	-4.0

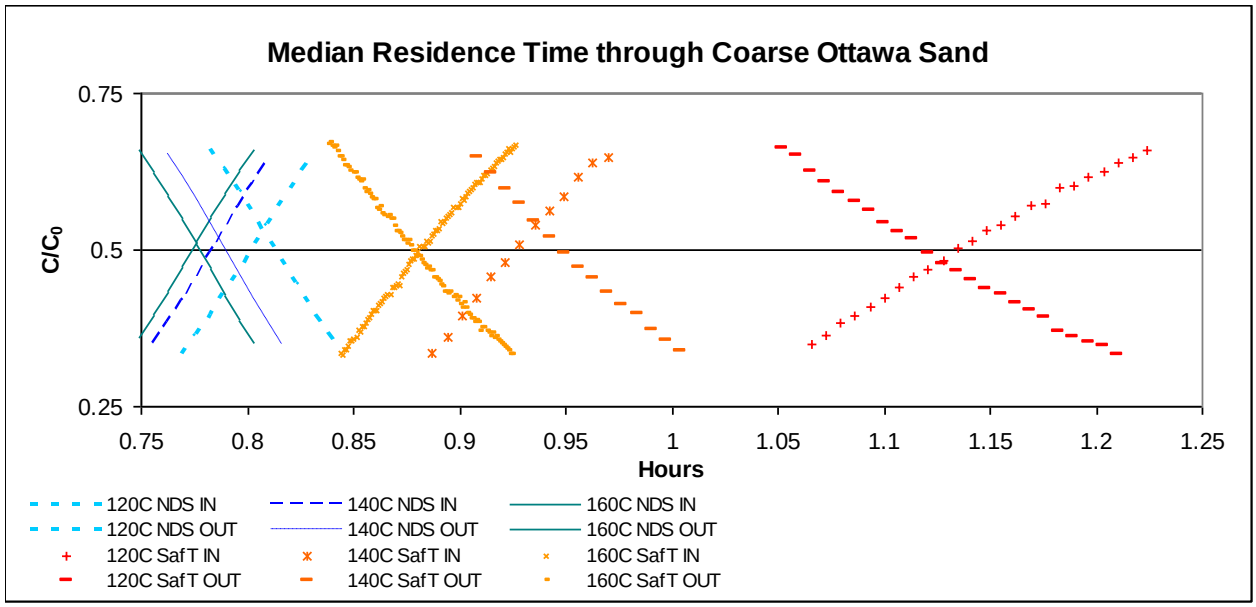

Figure 22.Comparison of the median residence times from breakthrough curves of safranin T through 0.5 mm Ottawa sand at three temperatures (120°, 140°, & 160° C). Retardation factors at the different temperatures are: 1.4, 1.2, & 1.1, respectively.

Fourth Quarter, 2010

Last quarter's results suggested that safranin T might not be held up sufficiently by the Ottawa sand to demonstrate measurable retardation in our columns above 180° C. Fortunately after this quarter's research and further analysis, it is clear that the relationship between R_f and temperature for safranin T has not turned out to be linear as concerned us last quarter. When examining the relationship between retardation factor and the inverse of temperature on a single particle size fraction there is an exponential relationship (see Figure 23). The trend shown from this series of experiments suggests that the safranin T could be held up by up to 2% relative to a conservative tracer by the medium fraction of the Ottawa sand at 220° C.

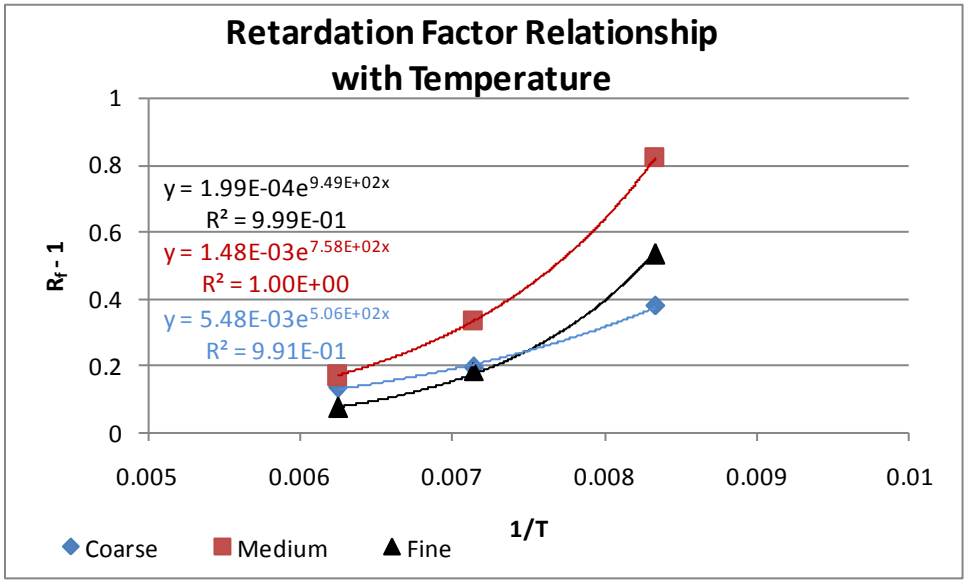

Figure 23. *Retardation of the reactive solute, safranin T, decreases exponentially with increasing temperature on Ottawa sand fine, medium, and coarse particle size fractions. The retardation factor was adjusted by subtracting one(1), based upon the equation relating the mass-based distribution coefficient to retardation factor:* $R_f = 1 + K_d \frac{\rho_b}{\theta}$.

Year 2, Subtask 2.3: Conduct a Single-Well Injection/Backflow Field Experiment to Measure Fracture Surface Area

Third Quarter, 2010

This task has not yet been initiated, since no single-well injection/backflow experiments have yet been conducted. However, Safranin T has just recently been identified as a promising candidate as a thermally stable tracer exhibiting sorption on geomedia. We are conducting a search for a suitable field experiment opportunity. Additionally, we have begun experiments comparing its sorption on columns packed with identical minerals (Ottawa sand), but different surface areas to empirically test the retardation factor response to increasing surface areas.

Fourth Quarter, 2010

This task has not yet been initiated, since no single-well injection/backflow experiments have yet been conducted. However, an EGS stimulation experiment at the Desert Peak geothermal field is in progress and will possibly provide an opportunity in the first quarter of 2011 to conduct an injection/backflow field experiment.

Year 2, Subtask 2.4: Invert Data to Determine Near-Wellbore Fracture Surface Area from Numerical Simulation Model

This task has not yet been initiated since no single-well injection/backflow experiments have yet been conducted.

Year 2, Subtask 2.5: Deploy the Field Fluorimeter to Demonstrate Identification of Fractures Created by a Hydraulic Stimulation

This subtask has not been initiated, since neither the design nor the fabrication of the newly modified tool has been completed.

Year 2, Subtask 2.6: Modify the Field Fluorimeter to Accommodate Downhole Measurements of Volumetric Flow Rate

This subtask has not been initiated, since neither the design nor the fabrication of the newly modified tool has been completed.

Phase II, Year 3

Progress Report for Year Ending September 30, 2011:

Tracer Methods for Characterizing Fracture Creation in Engineered Geothermal Systems

GO18193

Peter Rose[1], Principal Investigator; Joel Harris[2], Co-Investigator;

Karsten Pruess[3], Tianfu Xu[3], Michael Bartl[2], Mike Mella[1], Kevin Leecaster[1], Bridget Ayling[1], Paul Reimus[6], Bruce Boyes[4], Susan Petty[5]

[1]EGI, University of Utah
[2]Department of Chemistry, University of Utah
[3]Lawrence Berkeley National Laboratory
[4]Systronics, Salt Lake City
[5]AltaRock Energy, Seattle
[6]Los Alamos National Laboratory

Table of Contents for Phase II, Year 3

Project Objectives

The aim of this proposal is to develop, through novel high-temperature-tracing approaches, three technologies for characterizing fracture creation within Engineered Geothermal Systems (EGS). The objective of a first task is to identify, develop and demonstrate adsorbing tracers for characterizing interwell reservoir-rock surface areas and fracture spacing. The objective of a second task is to develop and demonstrate a methodology for measuring fracture surface areas adjacent to single wells. The objective of a third task is to design, fabricate and test an instrument that makes use of tracers for measuring fluid flow between newly created fractures and wellbores. In one method of deployment, it will be used to identify qualitatively which fractures were activated during a hydraulic stimulation experiment. In a second method of deployment, it will serve to measure quantitatively the rate of fluid flowing from one or more activated fracture during a production test following a hydraulic stimulation.

Task 1.4: Develop a Numerical Model to Calculate Fracture Surface Areas from Injection/Backflow data

Accomplishments

At LBNL, Karsten Pruess and Tianfu Xu:

First Quarter

We conducted a literature survey on single well injection-withdrawal (SWIW) tests in fractured media that involve reversibly sorbing tracers. We focused on parameter sensitivities, especially the sensitivity to fracture-matrix interface area.

TOUGH2 simulations were run for non-isothermal SWIW tests in fractured-porous media in which temperature plays the role of tracer. Different operational scenarios were explored for the sequence of fluid injection, a subsequent quiescent period, and withdrawal. Results show significant thermal contrast as a function of changes in fracture-wallrock surface area.

We performed numerical simulations to evaluate the ability of thermal single-well injection-withdrawal tests (SWIW) to provide characterization data for fracture systems intercepted by an injection well. Results of this work were presented in a paper at the Stanford geothermal workshop.

Third Quarter

No activity this quarter.

Bridget Ayling and Tianfu Xu:

Second Quarter

Numerical simulations performed to date have focused on simple 1D, porous-media models, the aim being to simulate the laboratory-based experiments in the column and explore the effect of different retardation factors on tracer breakthrough curves. A series of simulations were run with a sorbing and conservative tracer pair using the TOUGH-2 and TOUGH-REACT numerical codes developed by LBNL. The simple distribution-coefficient approach was applied to model tracer sorption, and several retardation factors were modeled. The 1D model consisted of a linear series of grid blocks with injection and production cells at either end; tracer injection occurred in the injection cell and was mapped spatially through time. The tracer breakthrough curve was extracted from a grid-block near the end of the sequence. Some comparative results are displayed in Figure 1 below.

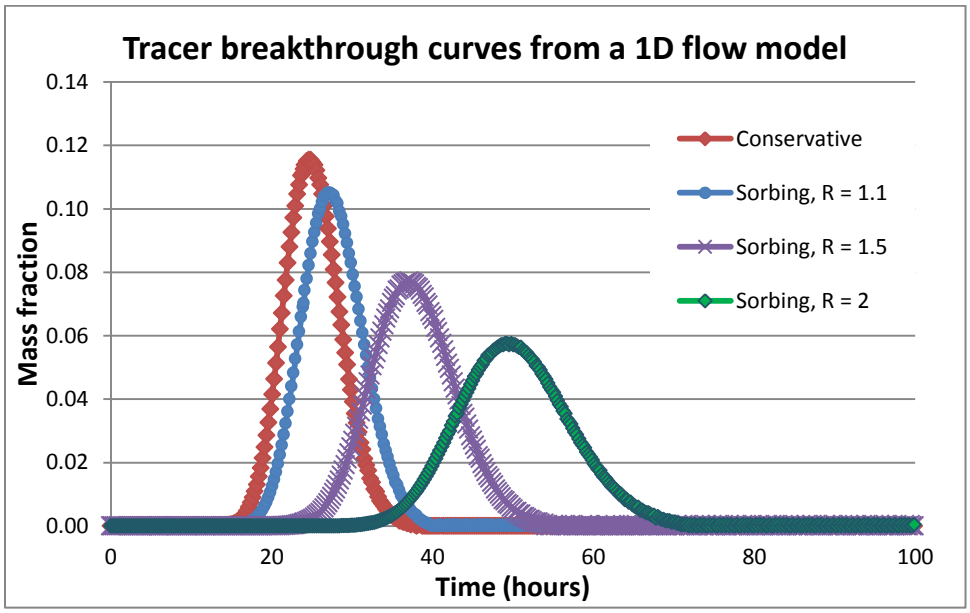

Figure 1: Simulated breakthrough curves for varying retardation factors in a porous medium.

The next stage of simulations will be to model tracer sorption in a fractured-porous medium, using the MINC mesh generator in TOUGH 2. This will enable the relationships between fracture surface area and retardation factor to be examined.

Third Quarter

In this quarter, there has been progress on the numerical modeling of the laboratory flow reactor. A simple, 1D flow-model is being developed and tested using TOUGH REACT, the goal being to simulate/replicate the behavior of the conservative and reactive (sorbing tracer) in the laboratory column. As discussed in previous sections (K. Leecaster), laboratory experiments were conducted on various tracers to identify compounds that have potential use as reactive tracers in geothermal reservoirs. Safranin T was identified as one such compound, and its sorption potential was further explored through experiments in the laboratory flow reactor under varying conditions (temperature and surface area). For our first attempt at simulating the

laboratory setup, we selected the experiment run at 120°C on the fine-grained Ottawa sand (mean grain size ~277μm). Model parameters are summarized in Table 1 below.

Table 1: Flow reactor parameters for numerical simulation

Column length	0.51 m
Column diameter	0.0254 m
Column porosity	0.34
Density	2650 g/m³
Heat capacity	800 J/kgK
Thermal conductivity	6.0 W/mK
Temperature	120°C
Flow rate	2 ml/min (0.000033 litres/sec)
Tracer Injection concentration	100 ppm NDS 1-5, 1.4ppm Saf T
Pressure (average)	1100 psi
Surface area	13.99m²
Mineralogy	Glass beads (SiO2)
Grain size (geometric mean)	277μm
Pore water velocity (v)	1.193 cm/min
Dispersion coefficient	0.41 cm²/min
Longitudinal dispersivity (α)	0.344 cm

We attempted first to match the physical dispersion within the flow reactor to the numerical dispersion of the model. Although the TOUGH codes do not explicitly enable the modeling of physical dispersion, it can be incorporated into the model via numerical dispersion, which occurs when the mass and heat transport equations are solved by finite difference approximations. The effect of numerical dispersion on the results is to 'smooth out' a tracer pulse in much the same way that physical dispersion affects a tracer pulse in the laboratory or the field. Physical dispersion $D = \alpha.v$ where α = longitudinal dispersivity, and v = the pore water axial velocity. Numerical dispersion $D_{num} = \frac{v.\Delta x.(1+\lambda)}{2}$ where λ is the Courant number defined as $\lambda = \frac{v.\Delta t}{\Delta x}$ where Δt and Δx are the time step and grid size respectively (Liou, 2007). D_{num} can thus be modified by changing the grid size and/or time step size.

For this first simulation attempt, the magnitude of numerical dispersion was calculated to equal the expected hydrodynamic dispersion with a grid block size of 0.4cm in the direction of flow. However, visually, it appears that an even smaller grid block size is required to reproduce the rapid rate of change observed in the breakthrough curve for the conservative tracer (Figure 2). The cause of the offset between the observed and modeled tracer concentration is not yet determined.

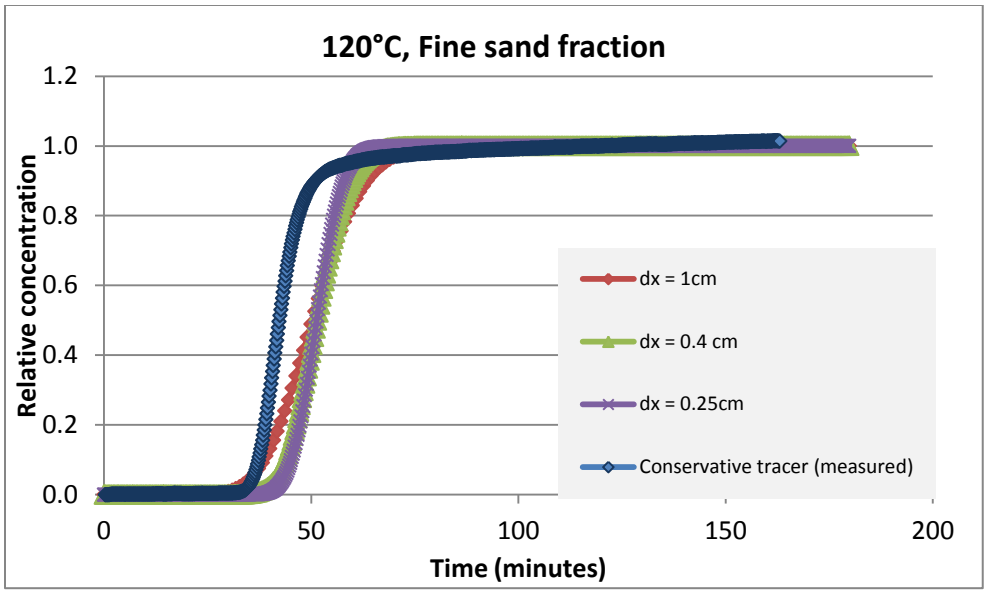

Figure 2: Simulated tracer breakthrough for the flow reactor, demonstrating the effect of changing the grid size on the numerical dispersion.

In addition, initial attempts at simulating the sorbing tracer (Safranin-T) were made, through modification of the retardation factor of the tracer (as can be specified in TOUGH REACT). Given that the laboratory experiments to date have determined R factors between approximately 1.1 and 2 for this tracer, we started here. In addition, diffusion of this solute tracer was also modified to see if this improved the correlation/fit of the modeled tracer curve with the observed (Figure 3). After a number of tests, it was found that the observed tracer data could be reproduced with a retardation factor of 1.35, and a solute diffusion coefficient of 1E-6 (Figure 4).

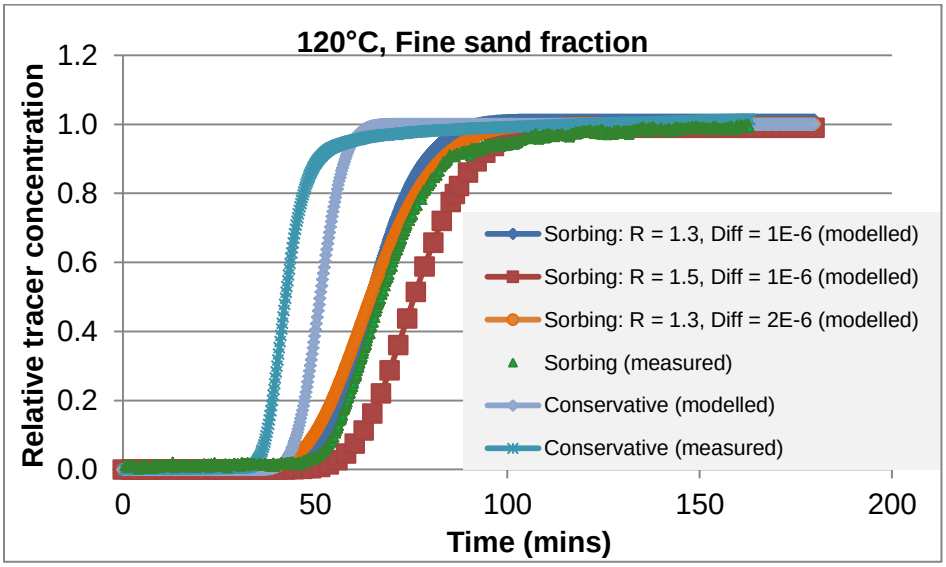

Figure 3: Numerical simulation results of the sorbing tracer at different model conditions (R factor and diffusion), compared to the conservative tracer break-through-curves.

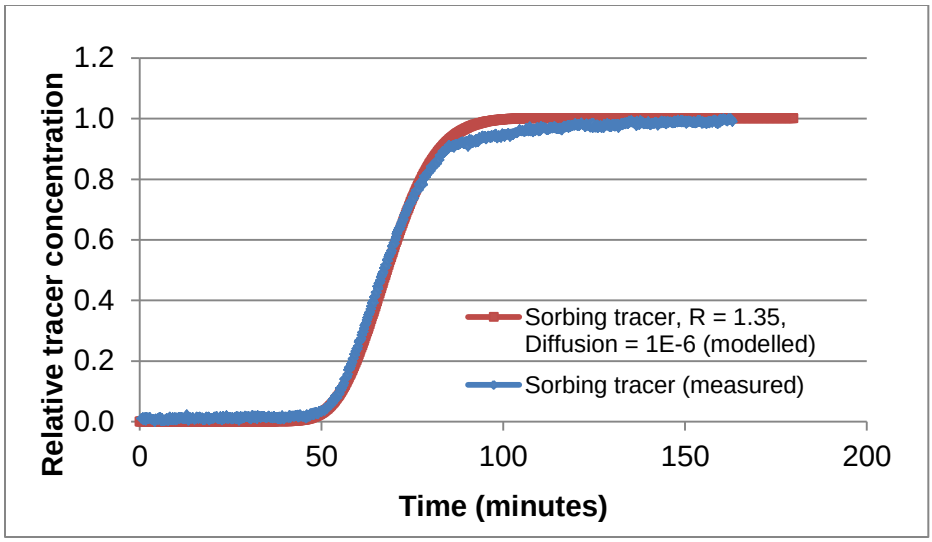

Figure 4: The best fit between the modeled and measured breakthrough curves for Safranin T at 120°C in the fine sand media was obtained with an R factor of 1.35, and a solute diffusion coefficient of 1E-6.

Future work will involve more rigorous testing of this 'visual curve-matching' approach, in combination with simulation of other experimental conditions in the flow reactor (temperature and surface area.

Fourth Quarter

Since last quarter, the offset between the observed and modeled breakthrough curves for the conservative tracer has been addressed (for the experiment at 120°C in the fine-grained Ottawa sand). This was achieved by modifying the media-porosity in the model. The updated results are illustrated in Figure 5 below.

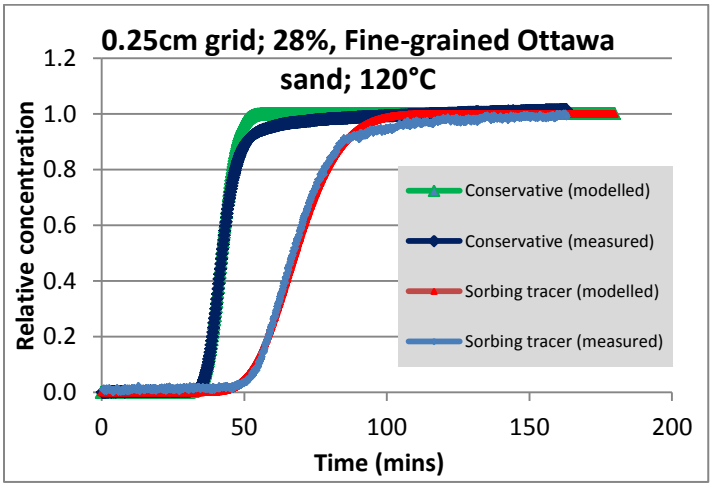

Figure 5: Simulated breakthrough curves of the conservative and reactive tracer plotted against the data measured using the laboratory flow reactor.

Using the same model values for the reactive tracer breakthrough curve except for diffusion (this was off for the conservative tracer, and turned on for the reactive tracer), the measured and modeled data were in agreement with a modeled retardation factor of 1.65: this value is close to the measured R value of 1.6. The breakthrough curve for the reactive (sorbing) tracer is displayed in Figure x.
Progress is continuing on building a numerical model of the flow-reactor that represents fractured media: this will use the MINC preprocessing module of TOUGH REACT. The aim here is to modify fracture surface area: volume relationships and observe the effect on the breakthrough curves of reactive tracers.

References:

Liou, T-S., 2007, Numerical analysis of a short-term tracer experiment in fractured sandstone. *Terr. Atmos. Ocean. Sci.*, Vol. 18(5), pp1029-1050.

Task 1.7: Design and Fabricate a Field Fluorimeter for Measuring Tracers Downhole

Background

The original design of the field fluorimeter was analyzed and considered to be too risky to pursue. It was to consist of a spectrometer (complete with fiber optics, a CCD camera and a laser light source) located at the surface near the wellhead. One of the problems identified with the design, however, was the need to mount the spectrometer on the coiled-tubing drum that will be used to deploy the fiber optic cable. The optical fiber would be deployed within the coiled tubing in order to protect it from the harsh environment within the wellbore. However, there are many problems associated with deploying 10,000 ft of optical fiber—even if that fiber is enclosed within capillary tubing. Not only is the fiber quite expensive to deploy in this fashion, any break in the fragile fiber would of course render the tool inoperable. Given these risks, an alternative design was developed that will allow for the deployment of the spectrometer downhole on a wireline, thus avoiding the problems associated with deploying optical fiber over long distances within EGS wellbores. The drawback of this approach is that the tool will now have to be designed and fabricated in such a fashion that it can be deployed downhole and through a lubricator, limiting the diameter of the tool to about 2.6 inches. As described below, excellent progress is being made towards the design and fabrication of the tool.

Current Design

A cartoon sketch of the tool design is shown below as Figure 6 including the optical fiber bundle that will serve as excitation light delivery and emission light collection.

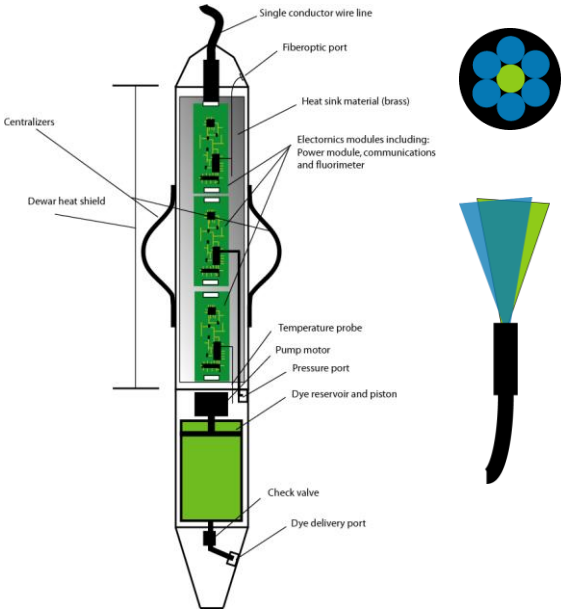

Figure 6. Cartoon sketch of purposed tool and fiber optic bundle.

Accomplishments

First Quarter

Rose and Boyes visited the Welaco offices in Bakersfield and Sandia National Laboratory in Albuquerque in order to discuss the design of the fluorimeter with experts (specifically, Dan Bebout at Welaco and Joe Henfling at Sandia) who design and deploy high-temperature geothermal-borehole tools. In addition Rose and Mella visited the Mitco facility in Riverside, CA to discuss their role in the design and fabrication of the critical dewar flask that will provide the structure for the tool and house the sensitive electronics and analytical equipment. It will have a nominal i.d. of 1.2 in. and an o.d. of 1.8 in. and a length of approximately 100 in. A contract was obtained with Cockrill Precision Products of Massachusetts to design and fabricate the motor/syringe assembly that will deliver the fluorescent dye. The design of the borehole fluorimeter (including a design review) will be complete by the end of next quarter (31 March, 2011).

Second Quarter

After working closely with dewar flask designer Pat Dailey of Mitco and Professor Joel Harris of the Department of Chemistry, significant progress was made towards the design of the borehole fluorimeter. A sketch of the tool concept is shown in Figure 7. Most significantly, we have devised a mechanism for delivering light from an LED through an optical fiber and out the open end of the flask, through a series of lenses and prisms into the uninsulated sub and finally through a sapphire window to the wellbore. The backscattered fluorescent signal will then return through the same set of filters, into a bundle of optical fibers and into a photomultiplier.

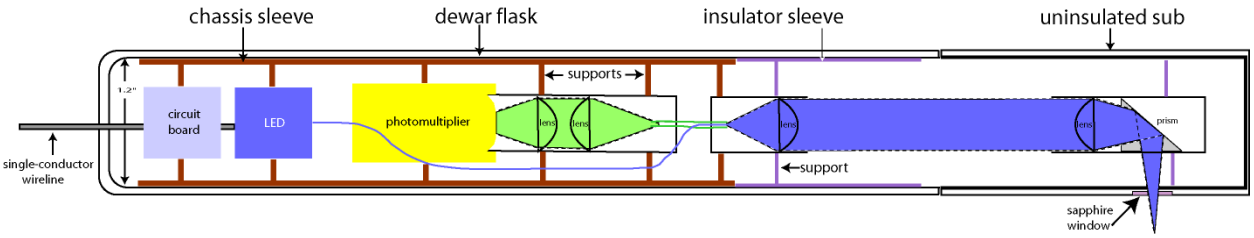

Figure 7. Updated sketch of the borehole fluorimeter showing the delivery and return of excitation and emission signals, respectively, between the tool and the wellbore.

A very preliminary laboratory prototype of the tool was constructed and used to demonstrate the feasibility of the concept. We are now in the process of purchasing components for the fabrication of a more advanced laboratory prototype. Dimensions of the components will be used by Mitco to complete a drawing of the flask and sub housing in anticipation of their fabrication.

Third Quarter

A mock up of the fluorimeter tool was constructed on a bench top. The photomultiplier tube (PMT) that will be used in the final tool was coupled with a mock circuit board with dimensions estimated from the circuit designer attached to a mock heat sink. Figures 8 and 9 show the PMT and the mock PMT and board on the heat sink.

Figure 8. The PMT

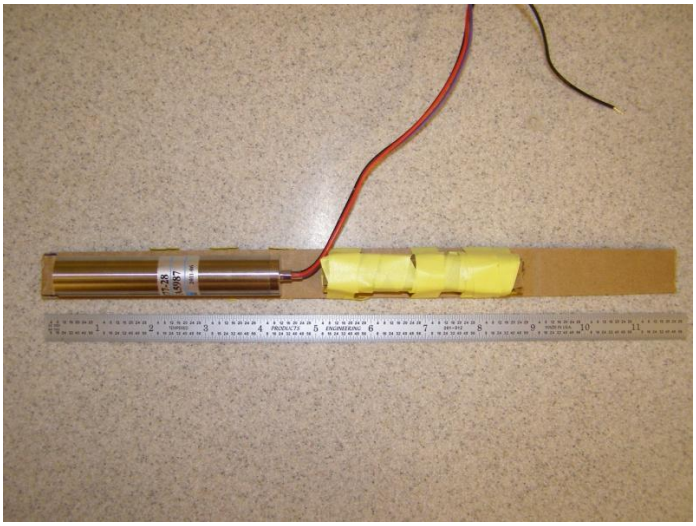

Figure 9. The PMT on a mock heat sink with the mock circuit board behind.

A lens holder tube with half-inch lenses was used to show that about 2" would be needed between the prism and the PMT to get a focused beam onto the PMT sensor. Figure 10 shows light being focused on the PMT sensor. In the lab we have been able to produce custom length fiber optic cables which ultimately should help in relaxing design constraints and shorten the overall length of the tool. If a different length is needed between the PMT and prism then a different length of fiber optic cable can be made.

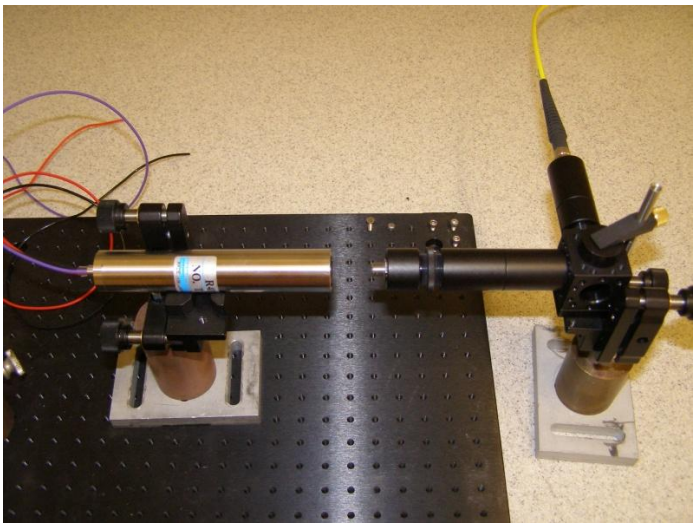

Figure 10. Light focused onto the PMT

Calculation of the fluid boundary layer around the tool revealed that in general the boundary layer will be less than 1 mm. Due to this small fluid boundary layer, the light beam directed from the prism will have sufficient focal length to be sufficient to analyze the bulk fluid in the well

bore. A short light tube (about 1”) and lenses would be sufficient to realize this. Figure 11 shows light being focused about 1.0 cm from the prism.

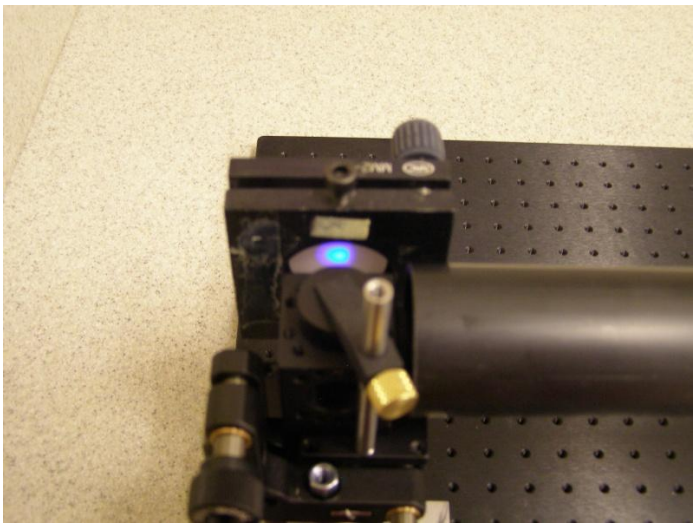

Figure 11. Light from coming from prism focused on paper.

A mock up of the tool is shown in Figure 12 with a 24” light tube with 1.18” inner diameter. These dimensions would be sufficient to contain the entire optical path, PMT and light source.

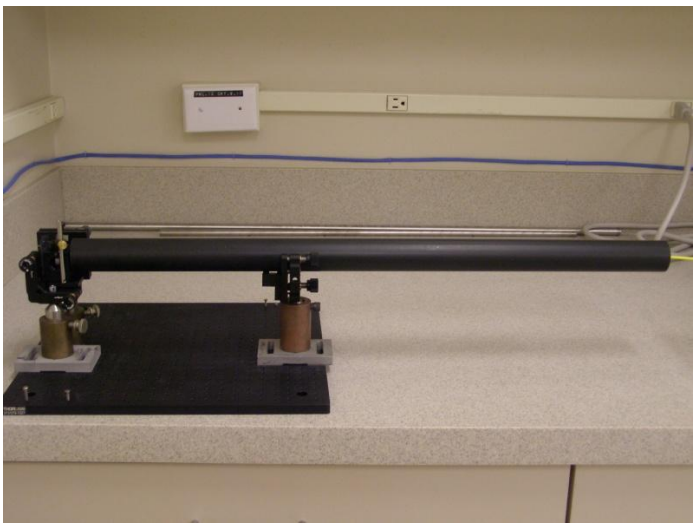

Figure 12. Mock tool on bench in 24” long 1.18” diameter tube.

Shown in Figure 13 are the circuit boards that will control the LED. The larger board stacks on top of an Arduino Uno or equivalent controller board which will run the firmware needed to control the LED in our lab model. Since such stacking boards for Arduino are called "shields" this would be a "Luxeon Rebel Shield". This shield includes an adjustable closed-loop constant current source for the LED. It can also be modulated to adjust the duty cycle of the stimulation source, while maintaining closed loop current drive. There is a place to mount a Luxeon Rebel

LED directly to that board, but not a means to attach a fiber connector. There are connector pads to connect this current source and monitor photo diodes to a remotely mounted LED/PD board which does accept a fiber.

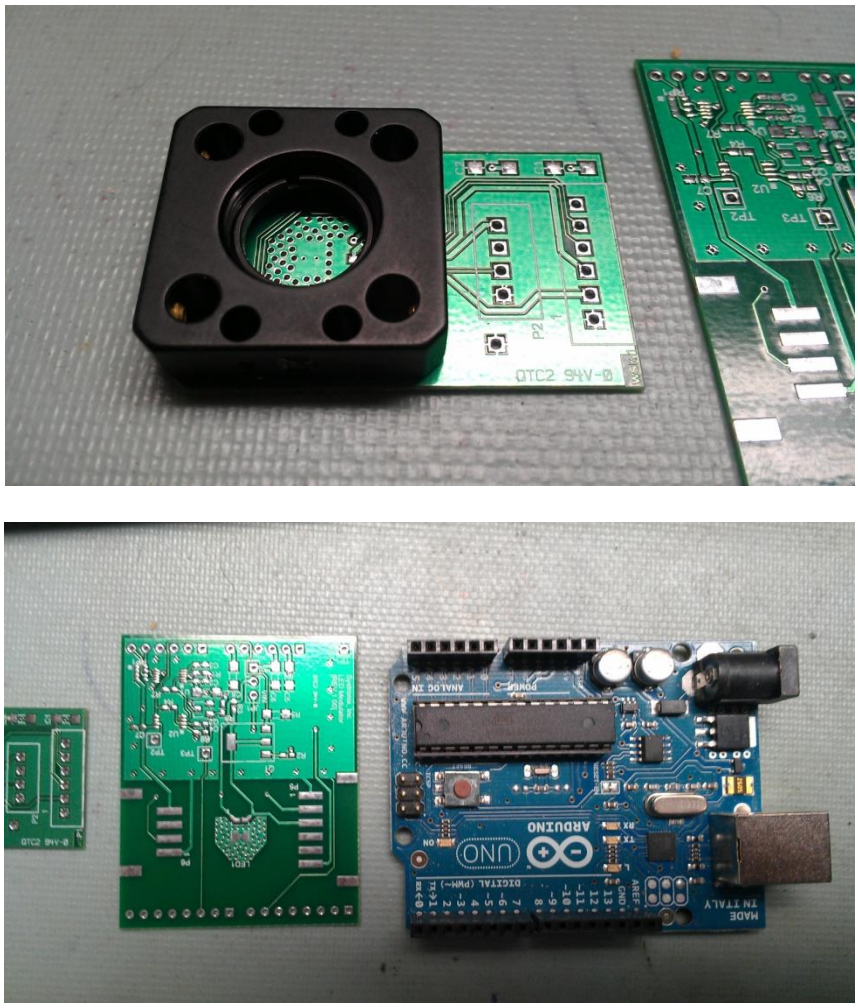

Figure 13. LED modulator boards

The small board is the remotely mounted LED/PD board which connects to the Luxeon Rebel Shield. This board has pads for a Luxeon Rebel LED, as well as dual monitor photodiodes which will sample stray light from the LED. It also includes a temperature sensor which is mounted directly to the LED heatsink area. This remote board has a series of pads for a Thorlabs SP02 adapter (the black square shown in one of the photos) and bolts to the larger PC board. Its major function is to center the Luxeon Rebel emitter in the SP02 threaded bore, which also accepts an SMA905 fiber connector adapter. This adapter then is held precisely centered over the LED and couples the maximum light possible into whatever fiber (600 or 1000 um core) is attached to that SMA905 adapter. From there, the emitter light travels through the optical path of the fluorimeter.

The LED is driven with a closed loop current source (feedback monitors the actual current through the LED). In addition the monitor photodiodes provide closed loop optical feedback. The temperature sensor provides for compensation for changes in LED output due to temperature, as well as allowing for its shut off if it gets too hot. It also lets for experimentation with the LED self-heating effect due to any combination of current drive and pulse duty cycle.

Fourth Quarter

The LED light source for the tool was completed and rigorously tested for durability and brightness. The light source is fully capable of staying on for long periods of time or being pulsed. The LED was run for several days continuously with no problems. The LED light source was also tested against a commercial LED light source meant for room temperature use only. The tool light source that was produced was superior in intensity at the wavelength to be used in this project. Overall the LED light source that was produced is better in terms of temperature range and intensity than anything that could have been purchased off the shelf.

The LED was coupled to optical components to produce a lab testing tool. The optical and electrical components were secured to a steel frame. This frame was housed in a clear polycarbonate tube with centralizers attached to the outside. The lab tool is still incomplete as it lacks a photo detector. Once the photo detector is completed it can be attached to the lab tool frame and a working tool will be ready to be tested in the lab. A photo of the completed portion of the lab tool is seen in Figure 14.

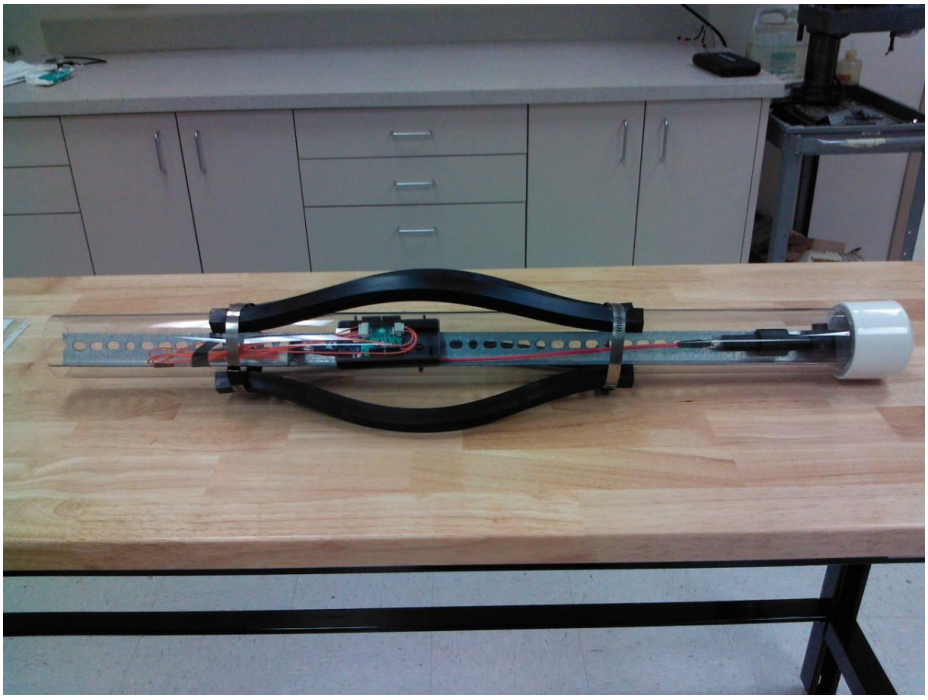

Figure 14. Lab demonstration tool inside polycarbonate housing.

The optical path has also been tested to ensure that emitted light can be seen back through the prism after passing through interference filters. A strong concentration of fluorescein was used

and green emitted light was clearly seen returning up the return path on a Y fiber optic cable. Once a photo detector is produced we will be able to determine the limit of detection this tool is capable of. A testing fixture for the lab tool and for the eventual field tool was also completed. This test fixture consists of an 8 inch translucent PVC tube with ports for the entrance of water and tracer. The tube is affixed to the wall and allows for a tool to be lowered into it. A photo of the test fixture with the lab tool is seen in Figure 15.

Figure 15. Laboratory test fixture.

In addition to the lab tool work continues on the design of the field tool. The basic components being designed for the lab tool should all be scalable to the size restrictions for the heat shielded field tool. Many of the same circuits will be able to be reused but will be put onto smaller printed circuit boards. For example the photo detector circuits and software will also be used for the PMT used in the field tool. The overall length of final field tool will be estimated from the lab tool and will allow for construction of the heat shield housing to begin.

Task 2.1: Continue Sorptive-Tracer Screening Tests

Accomplishments

First Quarter

The sorbing tracer Safranin T was screened at elevated temperatures this quarter in order to evaluate its use in a tracer projected at the Blundell geothermal reservoir in Utah. This reservoir is 260°C, substantially hotter than the temperatures of the previous series of screening tests up to 180°C. There was still measureable hold-up of the safranin T in relation to the 1,5-naphthalene disulfonate at 220°C on the medium size fraction of Ottawa sand resulting in an adsorption retardation factor of 1.06 and 1.05 during desorption. The retardation factors from the series of experiments with safranin T on the medium fraction from 120° - 260°C are shown in Figure 16. After completing more experiments it appears that the safranin T is retarded greater relative to the 1,5-naphthalene disulfonate during adsorption than during desorption.

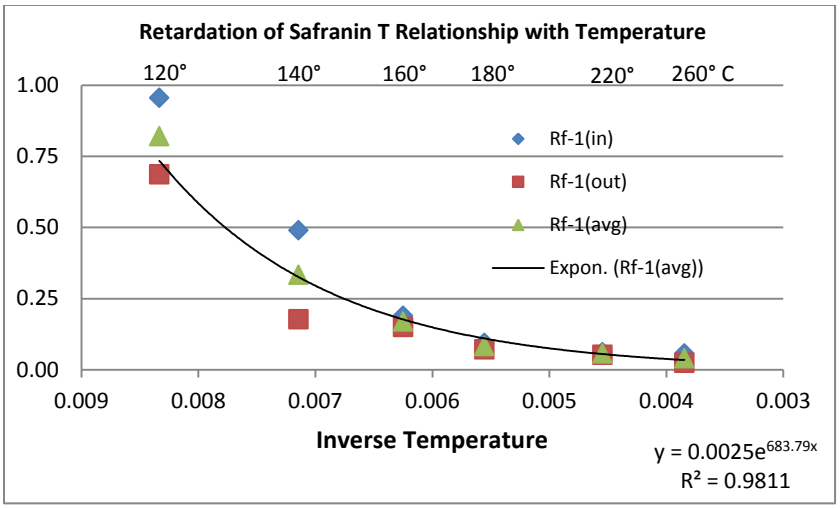

Figure 16. After normalization of the retardation factors to zero and inverse transformation of the temperature there is an apparent exponential relationship that may potentially be used to infer reservoir temperatures estimates from breakthrough curves of reactive tracers.

We also performed a series of screening tests to evaluate the elemental cation lithium on the same system to measure its retardation. Tests were performed at 25, 35, 45, and 90°C using a solution consisting of 20 ppm LiBr, 100 ppm disodium naphthalenedisulfonate, and 9 ppm tetraethylorthosilicate. The breakthrough curves from the 25°C screening test are presented in Figure 17 and the entire series is provided in Table 2.

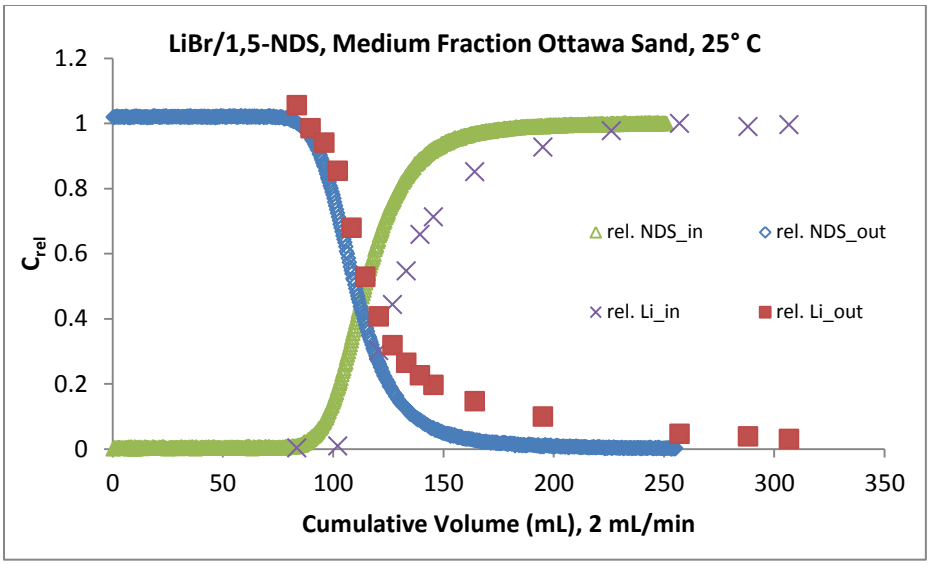

Figure 17. Results of lithium reactive tracer screening test through Ottawa sand fraction passing 0.5 and retained by 0.425 mm sieves.

Table 2. LiBr elution results through medium fraction of Ottawa sand	25° C		35° C		45° C		90° C	
	Entry	Exit	Entry	Exit	Entry	Exit	Entry	Exit
Li^+-Retardation Factor	1.14	1.04	1.12	1.01	1.14	1.06	1.15	1.03
Li^+-Slope ($0.34<C_{rel}<0.66$)	0.017	0.022	0.014	0.017	0.012	0.012	0.015	0.018
1,5-NDS^{2-}-Slope ($0.34<C_{rel}<0.66$)	0.025	0.026	0.023	0.025	0.013	0.016	0.028	0.030

Second Quarter

No activity this quarter.

Third Quarter

Screening tests of Safranin T on different size fractions of Ottawa sand were completed this quarter. This series of experiments eluted a solution of 175 ppm $CaCl_2$, 200 ppm NaCl, 10 ppm tetraethyl orthosilicate, 100 ppm 1,5-naphthalene disulfonate, and 1.4 ppm Safranin T at pH 5 through three columns with different surface areas, based on the geometric mean of particle diameter—all at 120, 140, and 160 degrees Celsius. These experiments demonstrate a relationship between surface area and the retardation of the Safranin T relative to the conservative tracer (Figure 18). There is a strong temperature response, as the retardation factor at 160° in the column with 14 m^2 is only 3% greater than the column with 8 m^2. When performed at 120° there was a 30% difference between the two columns. These results indicate that this cationic reactive tracer may lose significant resolution at higher temperatures, but could still indicate an increase in surface area if the change is large enough and there is not a large difference in temperatures. Additionally, if the surface area is the same a change in the temperature profile could be deduced from the change in retardation of the reactive tracer from subsequent tracer injections.

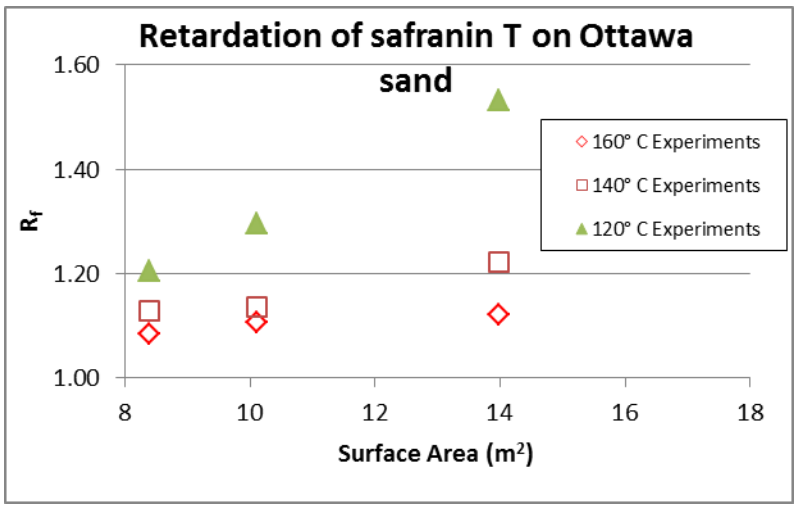

Figure 18. Nine experiments at three temperatures on three different size fractions of Ottawa sand demonstrate the relationship between surface area and retardation. There is also a significant temperature relationship that could be used to monitor temperature profiles within geothermal reservoirs, but will impede measuring small increases in surface area at high temperatures.

In order to further examine the relationship between surface area and retardation we intend to examine Safranin T retardation on 500 to 125 µm particles of tuff exhibiting substantial internal porosity. This will enable us to substantially increase the surface area in the flow reactor, as well as to examine Safranin T sorption on a different mineral type. We also are going to perform additional experiments on Ottawa sand at a higher eluent pH and with a lower ionic strength solution.

Fourth Quarter

We continued to screen safranin T's suitability as a reactive tracer for geothermal aquifers. In order to evaluate safranin T retardation on minerals other than the quartz sand of the initial screening tests, we performed a step injection of this sorptive tracer on a sample of rhyolite tuff obtained from a commercial rock specimen supplier (Ward's Natural Science). Figure 19 shows the mineral identification of the tuff using QEMSCAN technology (quantitative evaluation of minerals by scanning electron microscopy). Besides having different mineralogy than the Ottawa sand, we chose the tuff because we hoped internal porosity could provide a medium that might simulate fracture aperture flow through the inter-particle pores and matrix diffusion into the vesicular intra-particle void space. The results from this series of experiments will be discussed in more detail in section 2.2.

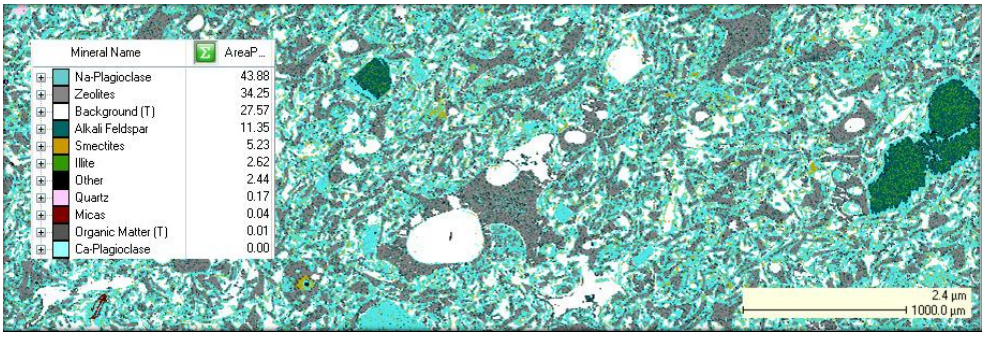

Figure 19. At less than 1% quartz, this rock specimen provided a significant contrast to the Ottawa sand of the initial experiments. Important points to note are: 1) high proportion of zeolites; 2) significant porosity (28% within this frame); and 3) the zeolite minerals reflect alteration and devitrification of the volcanic glass shards that comprise the tuff: the relict shard texture is distinct and the original vesicles in the glass typically remain as open pore space in the tuff.

We initially tested the thermal stability of safranin T in the flow solution that was used for the interwell simulation reactor (175 ppm $CaCl_2$, 200 ppm NaCl, 9 ppm tetraethyl-orthosilicate, 1.4 ppm safranin T, & 100 ppm 1,5 naphthalene disulfonate at pH 5) and saw good stability of less than 6% loss per day at 220 C. Results from field tests and this experiment through tuff indicated that its thermal stability might decrease in the presence of some mineral surfaces and/or at a different pH. We have begun autoclave runs to measure the thermal degradation of safranin T in 0.2% phosphate buffered solutions at pH ~7. Figure 20 shows the results from three of the recent tests compared to the earlier tests. Preliminary conclusions drawn from these results would indicate that the safranin T is not as thermally stable in the buffered solution as was estimated from its stability within the lower salt concentration of the experimental flow solution.

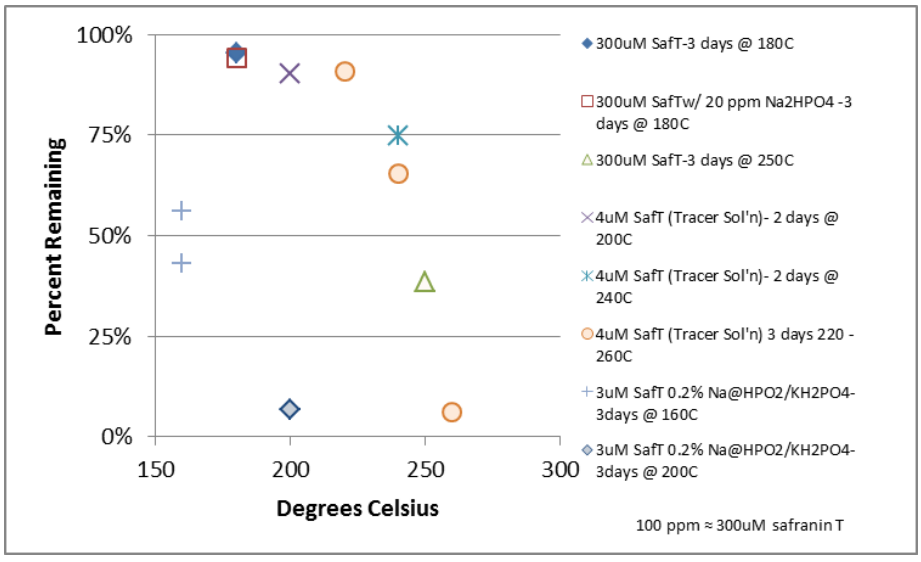

Figure 20. Selected results of autoclave thermal stability of safranin T. The recent tests in 0.2% salt 6.8 pH buffered solutions had less than 50% of the safranin T remaining, whereas the earlier tests at pH indicated that there would be minimal thermal decay at 160° C.

Task 2.2: Determine Adsorption Equilibrium Constants for Appropriately Adsorbing Tracers

Accomplishments

First Quarter

Conditional adsorption equilibrium constants from our flow through experiments were determined based on instantaneous, linear adsorption/desorption from the advective diffusion equation relationship between retardation factor and distribution coefficient. The formula is:

$$R_f = 1 + \frac{\rho_b}{n_e} K_{d,m}$$

where ρ_b is the bulk density (g/cm^3), n_e is the effective porosity, and $K_{d,}m$ is the distribution coefficient (mL/g). The mass based distribution factors from the safranin T and LiBr experiments are provided in Tables 2&3.

Table 2. Distribution coefficients of safranin T on fractions of Ottawa sand.

Fraction of Ottawa sand	Temperature (C)	Adsorption $K_{d,m}$ (mL/g)	Desorption $K_{d,m}$ (mL/g)
Coarse	120	0.089	0.076
Coarse	140	0.040	0.045
Coarse	160	0.028	0.027
Medium	120	0.239	0.172
Medium	140	0.119	0.043
Medium	160	0.047	0.037
Medium	180	0.023	0.018
Medium	220	0.014	0.012
Medium	260	0.012	0.005

Table 3. Distribution coefficients of lithium on medium fraction of Ottawa sand.

Temperature (C)	Adsorption $K_{d,m}$ (mL/g)	Desorption $K_{d,m}$ (mL/g)
25	0.037	0.009
35	0.033	0.004
45	0.038	0.017
90	0.040	0.008

Second Quarter

No activity this quarter.

Third Quarter

Effective adsorption constants of Safranin T on Ottawa sand are being determined based on the advective-dispersion equation (ADE) of solute flow through porous media. Initially we use a spline method to extract a representative selection of data from the breakthrough curve in order to decrease the quantity of data. Then the pore water velocity and the coefficient of dispersion are iteratively determined by minimization of the sum of squared error between observed and modeled estimates. For example the results from an experiment eluting Safranin T through 427 g of Ottawa sand with a geometric mean particle diameter of 0.28 mm are shown in Figure 21.

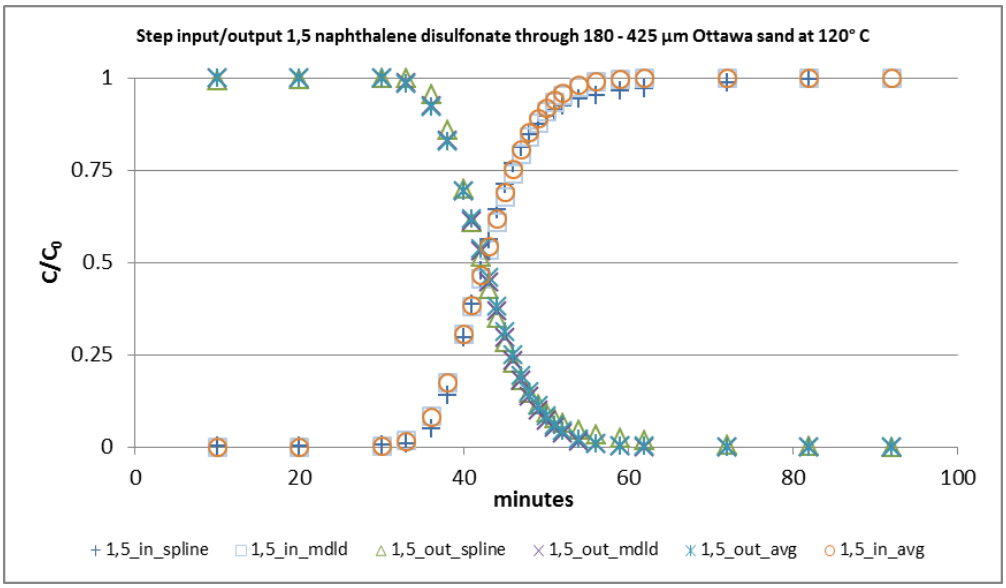

Figure 21. Parameter fitting of conservative tracer with the effect of using average values for the pore water velocity and coefficient of dispersion.

Next, for the reactive tracer, the average estimated pore water velocity and coefficient of dispersion determined from the conservative tracer are used within the ADE to estimate the retardation factor. It has been found on all of the initial analyses that an equilibrium based model of the coefficient of adsorption does not match well the observed experimental results. Using the Stanmod program for inverse model parameter fitting to the non-equilibrium advective dispersion equation (NADE) there is a good fit between the observed and modeled data, Figure 22.

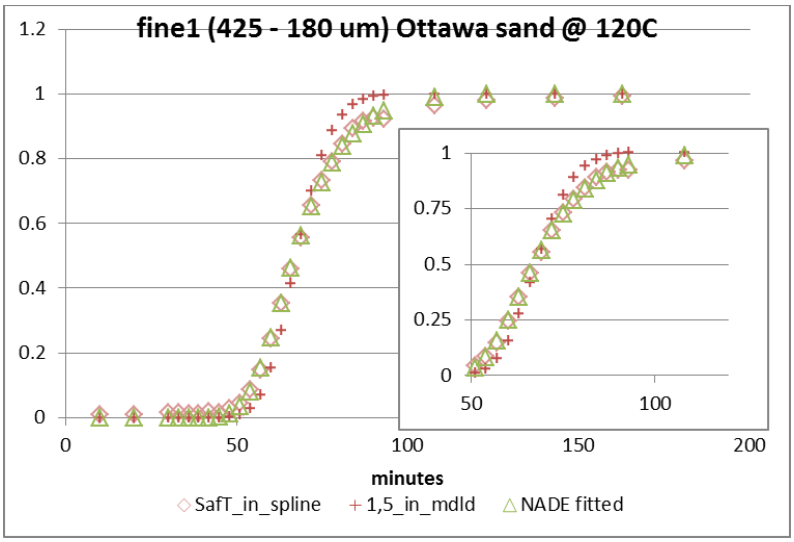

Figure 22. Model fitting of Safranin T.

There is not a large difference between the estimated equilibrium and non-equilibrium retardation factors in the experiments examined to date. There has been only a 1 – 3% estimated decrease in Rf when non-equilibrium conditions are assumed and the estimated dimensionless mass transfer parameter is less than 2% of the pore water velocity (n = 7). The commonly used relationship between retardation factor and the effective adsorption coefficient, $R_f = 1 + \frac{\rho_b}{n_e} K_{d,m}$ assumes equilibrium, whereas estimating the retardation factor directly from the difference in retention times of the reactive and conservative tracers is model independent. We will continue to evaluate the tracer behavior via model fitting in order to determine if there is an effect of temperature on the model parameters and/or equilibrium behavior. Experimentally we will compare breakthrough curves at differing pore water velocities in order to determine if apparent nonequilibrium behavior is observed to change at different fluid fluxes.

Fourth Quarter

Paul Reimus at LANL:

The MULTRAN (MULticomponent Reactive TRANsport) model was used to match the 1,5 NDS and lithium breakthrough curves in the experiments in the Ottawa sand-packed columns described in Task 2.1. As Figure 15 shows, the lithium was delayed relative to the 1,5 NDS during injection into the column, but when the tracers were flushed out of the column, it was only after a significant fraction of the NDS had eluted from the column that the lithium exhibited a delay relative to the NDS. This behavior is in contrast to the adsorbing dye Safranin T (breakthrough curves not shown here), which had a classic delayed response relative to the NDS during both the injection and elution phases of the experiments (see an example of an attempt to fit a lithium breakthrough curve with a simple non-mechanistic retardation model in Figure 23).

MULTRAN fits to the NDS and lithium breakthrough curves for the four column experiments at four different temperatures (Table 2) are shown in Figure 24. It is apparent that MULTRAN

qualitatively captured the asymmetrical breakthrough behavior of the lithium. This asymmetrical response can be attributed to charge balance constraints in the column experiment. A classical retardation response is observed during the injection phase as lithium gradually fills up cation exchange sites (presumably exchanging with sodium) until the entire column reaches equilibrium with respect to the available sites. Charge balance with the tracer anions (bromide and NDS) during the injection phase is maintained by cations being liberated from the cation exchange sites (see Figure 25, where it is assumed that the sodium is the primary exchanging cation). During the elution phase, charge balance is maintained by co-elution of both lithium and sodium with the bromide and NDS. The sodium and lithium maintain cation-exchange equilibrium on the sites throughout the experiment (sorption and desorption kinetics are assumed fast).

Interestingly, the lithium breakthrough curves were fit with the same cation exchange parameters in each experiment, suggesting very little temperature dependence of the exchange reactions over the temperature range studied (25-90C). The fits to the lithium breakthrough curves provide only a qualitative match to the final tailing behavior. The reasons for the discrepancies between model and data are not entirely clear, but they are most likely caused by some heterogeneity in the cation exchange sites (all sites were assumed identical in the model) or perhaps due to disequilibrium effects.

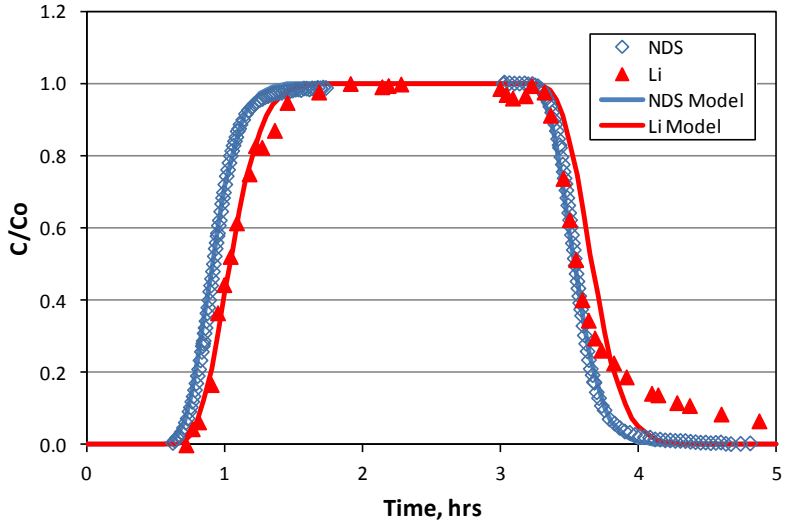

Figure 23. Example of a fit of a simple non-mechanistic retardation model to the 1,5-NDS and Li^+ breakthrough curves at 35C. Note the inability to fit the Li^+ data as the tracers are being flushed out of the column.

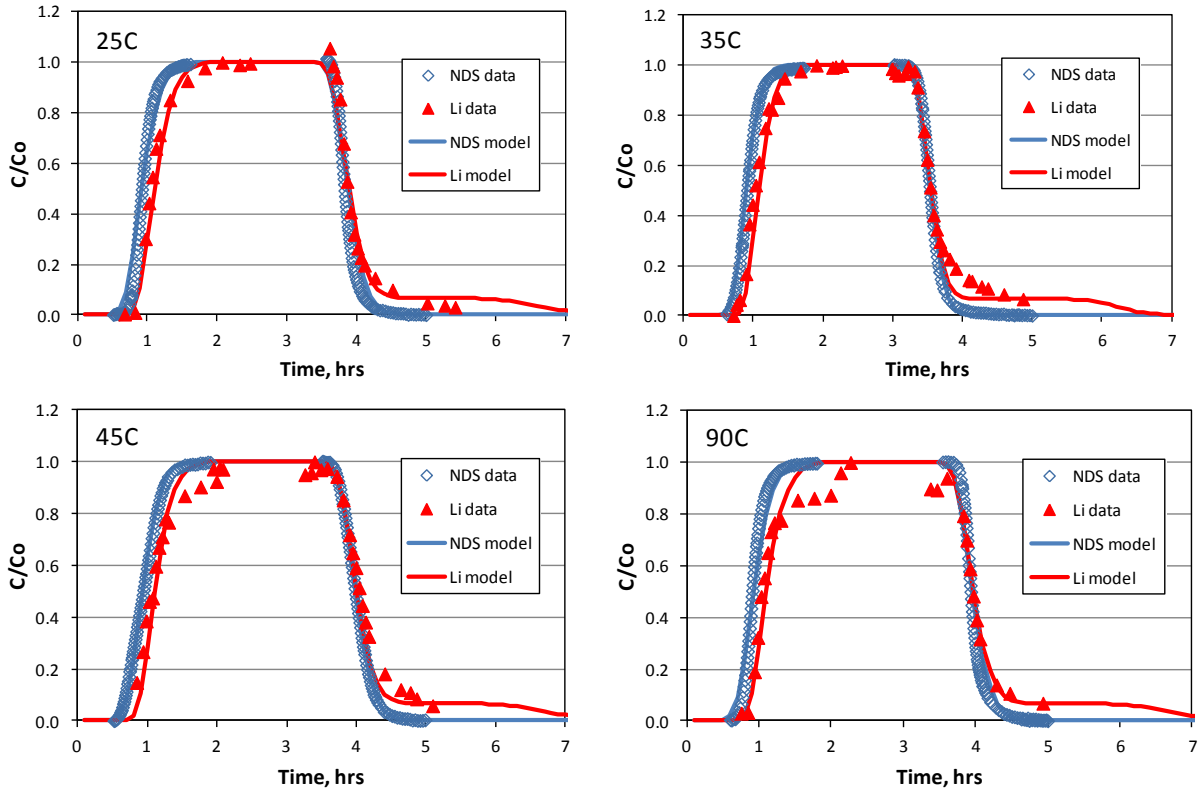

Figure 24. MULTRAN model fits to 1,5-NDS and Li^+ column data at different temperatures. The same cation exchange parameters were used at each temperature.

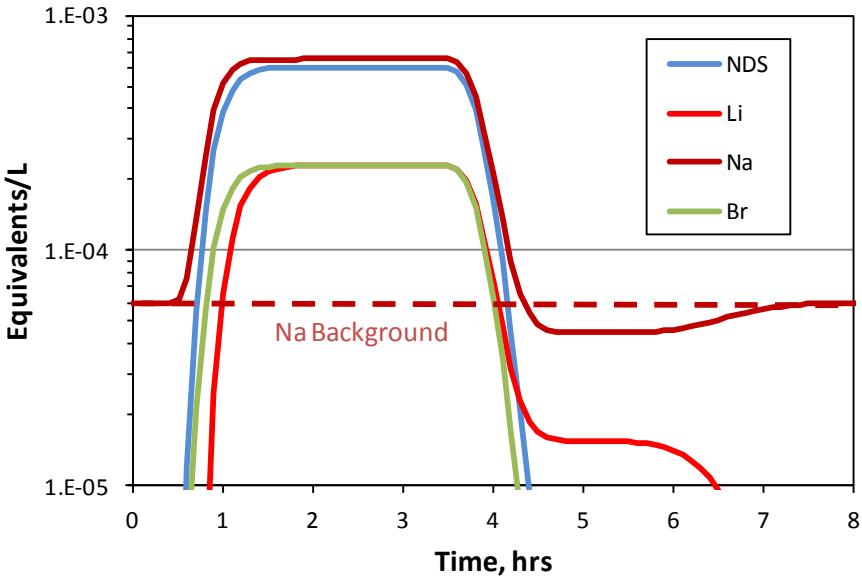

Figure 25. Multran predictions of 1,5-NDS, Li^+, Na^+ and Br^- concentrations (in eq/L, log scale) in the 25C column experiment. Note the conservative "arrival" of Na^+ to balance the charge of the anion tracers when they first arrive (also Na^+ is the counter-cation for the 1,5-NDS, which has a -2 charge). After the Li^+ concentration hits its maximum, the ratio of Li^+ to Na^+ concentrations remains the same until all the lithium has eluted from the column (starting at

around 6 hrs). It is assumed here that the exchange sites on the quartz sand are initially all occupied by Na^+ and that no other cations are present in the solution(s).

The model results suggest the possibility of using a cation such as lithium as a sorbing tracer in geothermal reservoirs to interrogate fracture surface area. Although lithium does not behave like a classically retarded tracer, the MULTRAN model allows the cation-exchange process to be depicted accurately enough to support surface area estimation provided cation exchange reaction parameters are reasonably well known. It is encouraging that even relatively clean quartz surfaces provided sufficient cation exchange capacity to significantly delay lithium transport relative to a conservative tracer. This suggests that the method offers promise in relatively unaltered systems that have little cation exchange capacity. The lack of temperature dependence of the lithium exchange reactions (if shown to hold at higher temperatures) is also desirable because it makes surface area estimation possible without temperature corrections. The principle disadvantage of using lithium as a reactive tracer is that detection limits are not as low as for fluorescent tracers, and significant background concentrations may exist in geothermal systems. The cation exchange method may therefore be best suited for single-well tracer tests in EGS systems, where return concentrations will be much higher than in interwell tracer tests. MULTRAN offers the capability to simulate single-well tracer tests.

Kevin Leecaster at EGI:

In order to use the retardation of a tracer to estimate fracture surface area it will be important to account for any differences in the tracer's adsorption affinity to the different mineral surfaces with which it interacts. During an internship with EGI this quarter; undergraduate student, Raphael Sanjuan, of the INP-ENSIACET in Paris, France; helped to perform an experiment testing the retardation of safranin T through our simulated interwell flow reactor. We performed the experiment at 160° C with the same flow rate and solution (175 ppm $CaCl_2$, 200 ppm NaCl, 9 ppm tetraethyl-orthosilicate, 1.4 ppm safranin T, & 100 ppm 1, 5-naphthalene sulfonate at pH 5) as we've used for our experiments through the Ottawa sand. The breakthrough curve from this experiment is shown in Figure 26.

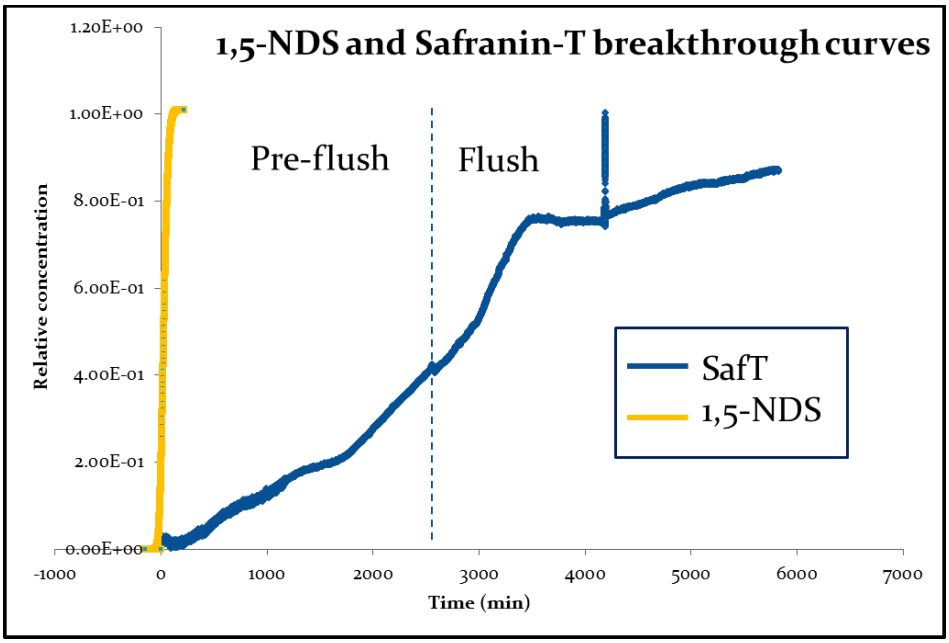

Figure 26. Breakthrough curve through rhyolitic tuff particles passing through 0.5 mm and retained by 0.18 mm sieves. Even after 21 hours after starting the safranin T, full breakthrough had not occurred indicating that it was retarded much more by tuff's mineral surfaces than by the Ottawa sands quartz surfaces.

We used HPLC to measure the safranin T concentration of a few aliquots of column effluent. These results show that near the end of the column experiment the concentration of safranin T was still not equal to the intial tracer solution concentration still after 2 days of flushing was still increasing. Also, the HPLC analysis showed that some of the same degradation products that we have seen in chromatograms of field & autoclaved samples were in the effluent from the 160° C tuff column experiment (Figures 27 & 28). We are currently using LC/MS to identify these compounds and to rerun under the same conditions through the Ottawa sand to see if this effluent contains the same molecules.

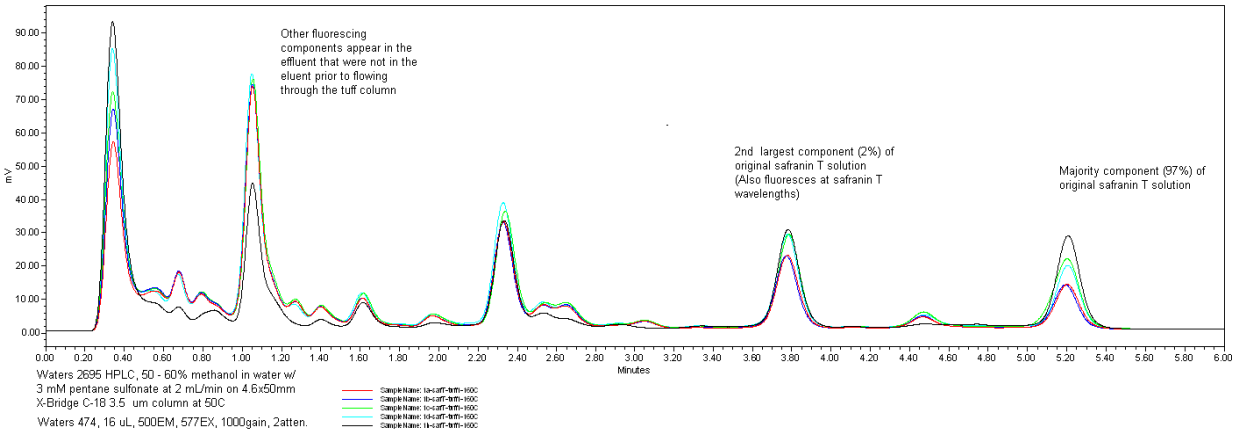

Figure 27. HPLC analysis of the effluent from the 160° C tuff experiment showing safranin T decay products.

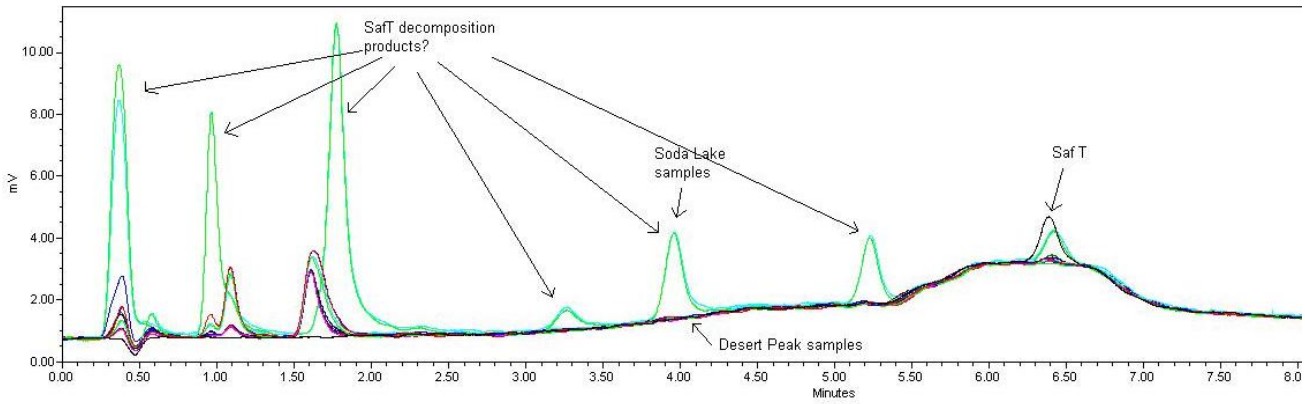

Figure 28. Thermal decomposition daughter products in samples from field injections of safranin T. Soda Lake is hotter than the Desert Peak, but it is probably more similar to the rhyolitic tuff's clay and zeolite content.

Task 2.3: Conduct a Single-Well Injection/Backflow Field Experiment to Measure Fracture Surface Area

Second Quarter

An injection-backflow reactive-tracer test was conducted at The Geysers geothermal field as part of a hydraulic stimulation experiment. A reactive two-phase tracer (n-propanol) was co-injected with a conservative vapor-phase tracer. After a brief shut-in period, the well was allowed to flow and tracer samples were taken. Samples were taken and returned to the laboratory for analysis.

Interwell sorbing-tracer tests accompanied the above-mentioned injection-backflow test at The Geysers. This interwell test will provide addition information on the utility of the tracer pairs in characterizing the interwell fracture surface area. And, it will have obvious relevance to the injection-backflow sorbing-tracer tests.

A second sorbing-tracer test was initiated this quarter at the site of the Desert Peak EGS project. The sorbing tracer Safranin T (see Task 2.1 above) was co-injected with the conservative tracer 1,6-naphthalene disulfonate. Samples are being collected daily and sent to the EGI laboratory for analysis.

These sorbing-tracer tests will have significant value in interpreting the results of the hydraulic stimulation EGS experiments at The Geysers and at the Desert Peak projects.

Third Quarter

The analyses of the tracer samples taken during The Geysers tracer test revealed that the PFT tracers, normalized for the masses injected, were recovered in much lower concentration (by about 3 orders of magnitude) than the alcohol tracers. This phenomenon could be explained by the much higher mobility of the vapor phase PFT tracers over the partitioning alcohol tracers.

The recovery of the PFT tracers was too low for them to be effective in calculations of fracture surface area.

At the Desert Peak EGS tracer test, the sorbing tracer Safranin T was never recovered. This is not unexpected given the very low recovery of the conservative tracer 1,6-naphthalene disulfonate. A second tracer test is planned during the coming quarter to test the sorbing tracer Safranin T under more favorable conditions.

Fourth Quarter

No opportunities arose for conducting an injection/backflow field experiment during this quarter. However, an interwell field test at Soda Lake with a very short residence time provided a proxy for an injection/backflow experiment. In this field test, 50 kg of the conservative tracer 1,6-nds and 100 kg of the sorbing tracer Safranin T were injected into temporary Soda Lake well 45A-33 in rapid succession. The produced water at neighboring well 32-33 was monitored for tracer production over the subsequent 20 days.

Paul Reimus (LANL):

A preliminary analysis was conducted to interpret an interwell tracer test involving near-simultaneous injection of a conservative and a reactive tracer (1,6 NDS and Safranin T, respectively) at Soda Lake, NV. The analysis was conducted using the RELAP (Reactive Transport LAPlace Transform Inversion) code, which was developed to interpret multiple tracer breakthrough curves in interwell tracer tests. RELAP uses a relatively simple retardation approach to model reactive transport. Laboratory testing with Safranin T had previously indicated that this approach should be adequate for modeling the transport of Safranin T.

The RELAP modeling of the Soda Lake test is considered preliminary at this time because the thermal decay kinetics of Safranin T are still being determined in the laboratory. Corrections for thermal decay are necessary because the Safranin T exhibited much lower normalized concentrations relative to the 1,6 NDS than would be expected from sorption alone. Also, the preliminary laboratory testing has confirmed significant thermal decay of the Safranin T at Soda Lake reservoir temperatures.

Figure 29 shows RELAP fits to the 1,6 NDS and Safranin T breakthrough curves assuming that the thermal decay constant for Safranin T is 0.35 day^{-1} (the Safranin T curve of Figure 29 is corrected for thermal decay, with the measured concentrations also plotted for comparison). The decay constant was somewhat arbitrarily chosen, although it was constrained to (1) fall between preliminary laboratory measurements of 0.23 day^{-1} (160C) and 0.99 day^{-1} (200C), and (2) keep the corrected Safranin T recovery less than that of the 1,6 NDS (which was approximately 25% after 500 hours). Based on the very preliminary thermal decay data, the assumed decay constant of 0.35 day^{-1} would correspond to an average reservoir temperature of ~170C. The known temperature of the reservoir is ~190C, so further delineation of the thermal decay kinetics of Safranin T is warranted. It should be noted that only minimal matrix diffusion of the tracers was assumed in the modeling exercise, with the same diffusion coefficients assumed for both tracers. Also, no sorption of Safranin T was assumed to occur in the matrix.

The modeling will be refined as more thermal decay data become available and as additional information on reservoir matrix properties relevant to matrix diffusion and matrix sorption becomes available. Ultimately, we hope to place some reasonable bounds on estimates of fracture surface area present along the flow pathways in the tracer test.

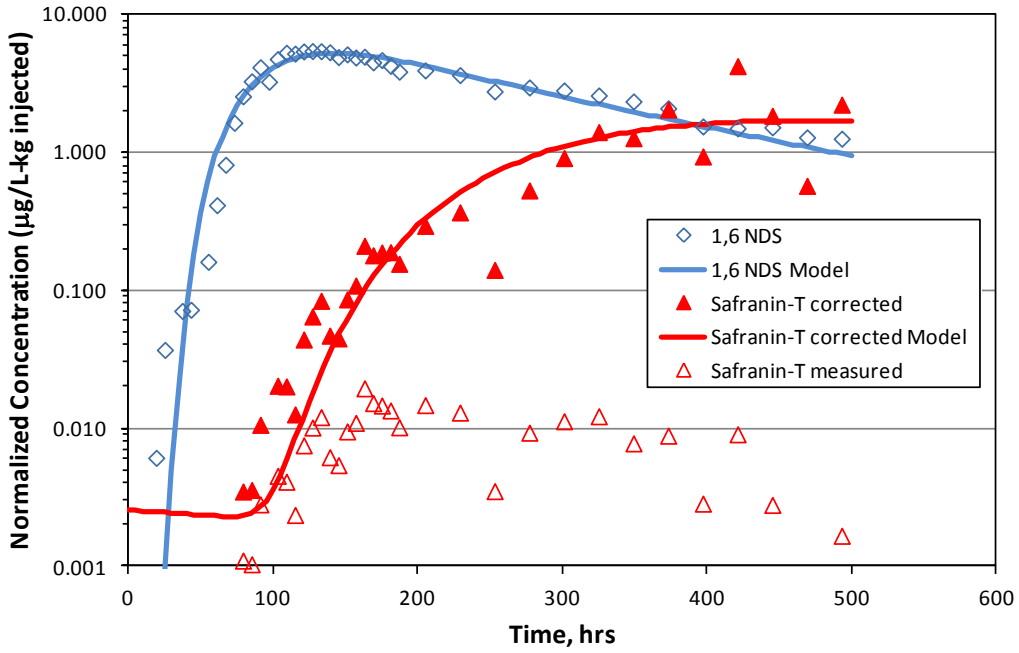

Figure 29. Preliminary RELAP fits to the 1,6-NDS and thermal-decay-corrected Safranin-T breakthrough curves in the Soda Lake tracer test. The best-fitting Safranin-T retardation factor is 3.4. Model interpretations will be refined as more Safranin-T thermal decay data and matrix property data become available. Sorption in the matrix is not accounted for.

Kevin Leecaster (EGI):

Construction of the simulated, physical injection/backflow model that will be used to calibrate and verify the numerical inversion estimates of surface area from reactive tracer field tests is progressing and is anticipated to ready for high temperature experiments during the next quarter.

Task 2.4: Invert Data to Determine Near-Wellbore Fracture Surface Area from Numerical Simulation Model

Accomplishments

Paul Reimus (LANL):

First Quarter
The 2-D numerical code, MULTRAN (MULticomponent mass TRANsport) was modified to simulate simultaneous heat and mass transfer in either single-well or cross-hole tracer test

configurations (it formerly solved only mass transfer in isothermal systems). The modifications include the capabilities to specify thermal decay of tracers and to account for temperature dependence of diffusion coefficients. Temperature dependence of cation exchange equilibrium constants will be incorporated into the code in the next quarter. Also, the computational speed of the code will be improved by allowing larger time steps for mass transfer calculations than for heat transfer calculations. The latter require much smaller time steps because thermal diffusivity is much faster than mass diffusivity. Also, the mass calculations are much more expensive per time step because they involve as many sets of equations as there are components and the equations are more complex than for heat transfer because interactions between components must be accounted for. The code successfully ran several test cases.

Third Quarter

Nothing to report.

Fourth Quarter

Nothing to report.

Karsten Pruess and Tianfu Xu (LBNL):

Second Quarter

We performed simulation studies of thermal single-well injection- withdrawal (SWIW) tests, both for individual fractures and for 3-D fracture networks. Our focus was on evaluating the sensitivity of temperature recovery curves to geometric parameters of the fractures, such as (average) fracture aperture b, fracture porosity phi, fracture height H, and fracture spacing D. A first account of this work was presented at the Hedberg geothermal conference in March 2011 (Jung and Pruess, 2011):

Jung, Y. and K. Pruess. Sensitivity Analysis of Thermal Single-Well Injection-Withdrawal Tracer Tests for Evaluating Fracture-Matrix Heat Transfer Area, presented at AAPG/SPE/SEG Hedberg Research Conference "Enhanced Geothermal Systems", Napa, California, March 14-17, 2011.

Third Quarter

No activity this quarter.

Fourth Quarter

A closed-form analytical solution was recently developed for thermal single-well injection-withdrawal (SWIW) tests. The earlier analytical solutions available are limited to the SWIW tests with no quiescent time, and unfortunately include errors in the equations. The numerical simulations for thermal SWIW tests are also found to be very susceptible to space and time discretization errors. However, with the newly developed analytical solution, the time

dependence of temperature recovery can accurately be evaluated for thermal SWIW tests entailing the injection of cold water into a well (injection period) and, after a certain quiescent or shut-in period, the production of the water from the same well (withdrawal period). Uniquely, during the derivation process, the initial temperature distribution for each period is not solved to find the transform during the derivation process. Accordingly the final solution includes the given initial condition for fracture and matrix. The advantage of this approach is that different initial conditions can easily be applied to our analytical solution. Therefore, the analytical solution can be applied to a SWIW test with slug-like injection or even more complicated injection scheme such as intermittent injection.

The analytical solution shows that strong thermal diffusivities of rocks as compared to typical solute diffusivities are not necessarily advantageous for characterizing fracture-matrix interaction, and therefore it is critical to carefully evaluate the sensitivites of thermal tracer tests to the properties of the fractured rock, including the fracture-matrix interface area. The dependency of return temperatures on other advection related mechanisms may improve the sensitivity of the tests to the fracture-matrix interface area, and will further be investigated.

The work has been summarized in a paper submitted to Water Resources Research. Figure 30 shows the schematic representation of the fracture-matrix system. Some results are given in Figure 31.

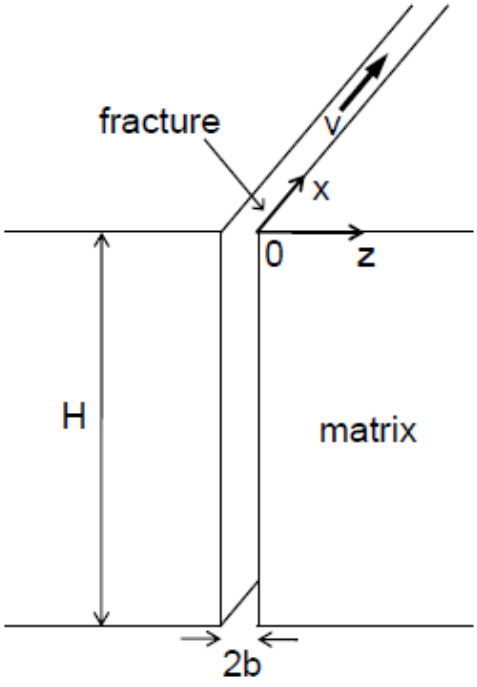

Figure 30. Perspective of a fracture with width 2b and height H and attached semi-infinite wall rocks.

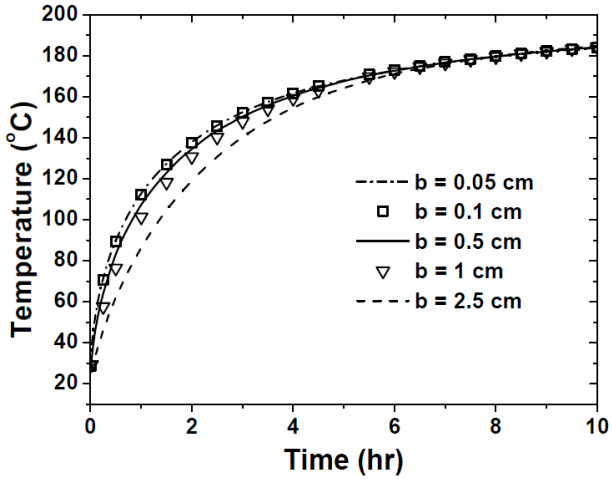

Figure 31. Effect of *b* (half fracture aperture) on temperature return profiles.

References

Jung, Y., and K. Pruess, A Closed-Form 6 Analytical Solution for Thermal Single-Well Injection-Withdrawal (SWIW) Tests, Paper submitted to Water Resources Research, 2011.

Task 2.5: Deploy the Field Fluorimeter to Demonstrate Identification of Fractures Created by a Hydraulic Stimulation

This subtask has not been initiated, since neither the design nor the fabrication of the newly modified tool has been completed.

Task 2.6: Modify the Field Fluorimeter to Accommodate Downhole Measurements of Volumetric Flow Rate

This subtask has not been initiated, since neither the design nor the fabrication of the newly modified tool has been completed.

Phase II, Year 4

Progress Report for Year Ending September 30, 2012:

Tracer Methods for Characterizing Fracture Creation in Engineered Geothermal Systems

GO18193

Peter Rose[1], Principal Investigator; Joel Harris[2], Co-Investigator;

Mike Mella[1], Kevin Leecaster[1], Bridget Ayling[1], Paul Reimus[6], Mark Williams[7], Vince Vermeul[7], Bruce Boyes[4], Susan Petty[5]

[1]EGI, University of Utah
[2]Department of Chemistry, University of Utah
[4]Systronics, Salt Lake City
[5]AltaRock Energy, Seattle
[6]Los Alamos National Laboratory
[7]Pacific Northwest National Laboratory

Table of Contents for Phase II, Year 4

Project Objectives

The aim of this project is to develop, through novel high-temperature-tracing approaches, three technologies for characterizing fracture creation within Engineered Geothermal Systems (EGS). The objective of a first task is to identify, develop and demonstrate sorbing tracers for characterizing interwell reservoir-rock surface areas and fracture spacing. The objective of a second task is to develop and demonstrate a methodology using reactive tracers for measuring fracture surface areas adjacent to single wells. The objective of a third task is to design, fabricate and test an instrument that makes use of tracers for measuring fluid flow between newly created fractures and wellbores. In one method of deployment, it will be used to identify qualitatively which fractures were activated during a hydraulic stimulation experiment. In a second method of deployment, it will serve to measure quantitatively the rate of fluid flowing from one or more activated fracture during a production test following a hydraulic stimulation.

Task 4.1: Select an Adsorbing Tracer for a Field Test for Characterizing Interwell Fracture-Surface Area in a Geothermal Reservoir

Second Quarter

This quarter we continued to identify and investigate dyes that can react within the reservoir both by adsorbing to the fracture surfaces and by thermally degrading. Two more candidates besides safranin T that may exhibit both of these characteristics are amino G (Figure 1A) and amaranth dye (Figure 1B). Phosphate buffered solutions of amino G were autoclaved in fused quartz ampules and thermally degraded at 180° C to 2-naphthol (see Figure 1) as seen in the spectrum shown to the right of the parent molecule's spectrum in Figure 2. Flow experiments to test amino G adsorption were initiated by testing different conservative tracers with naphthol and amino G, but it was determined that the use of a UV light would be needed and one has been ordered.

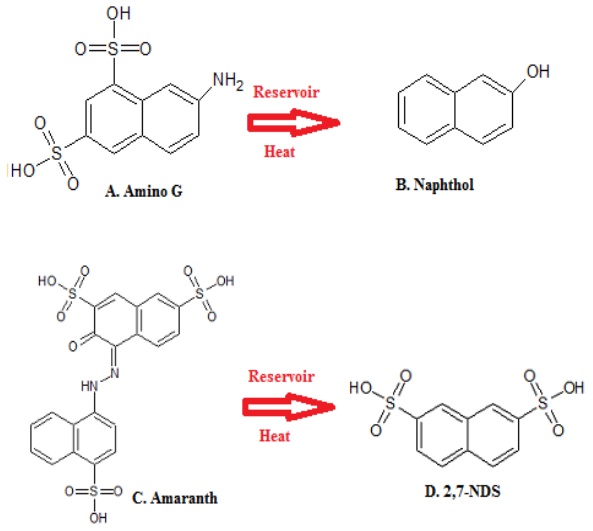

Figure 1: Reactive pathways of two candidate tracers for use in injection/backflow tracer testing. Both Amino G and Amaranth are possibly sorbing tracers.

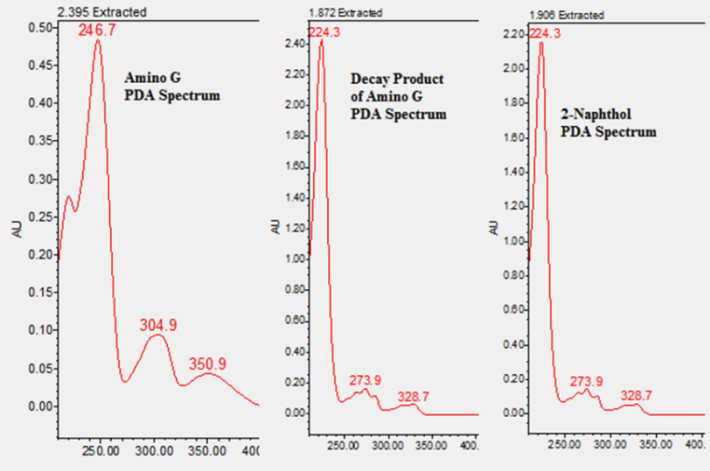

Figure 2: Absorption spectrum demonstrating 2-naphthol formation from the thermal decay of Amino G.

Amaranth dye (Figure 1C) was eluted through the interwell reactor filled with Ottawa sand to test for adsorption and thermal decay. After testing a variety of conservative tracers that would not interfere with amaranth detection, we proceeded with a low concentration of amaranth (0.5 ppm) and the yellow #5 food dye. Figure 3 shows the absorption spectra of the two dyes in the inline spectrometer suggesting that there would not be significant interference, but when eluted through the detectors there was still interference between the two tracers. We attempted to compensate by decreasing the concentration of the amaranth and increasing the sensitivity of detector. The increased sensitivity, by multiplying the signal from the CCD, produced considerable noise and a shifting baseline while monitoring the effluent but the unloading portion of the breakthrough curve appears to provide an indication that there was not significant retardation of the amaranth on the sand at 25° C, pH 7. Analysis of the signals from the different wavelengths by comparison of the flow until median concentration, shown in the inset within Figure 4, suggests that there was no retardation of the amaranth, but this will be examined with better detectability this quarter by using an alternative conservative tracer.

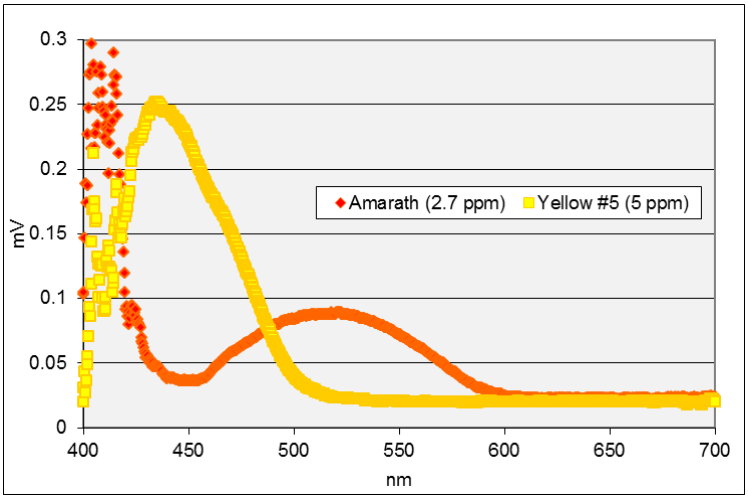

Figure 3: Example of spectra used to determine viability of independent monitoring for reactive/conservative tracer combinations.

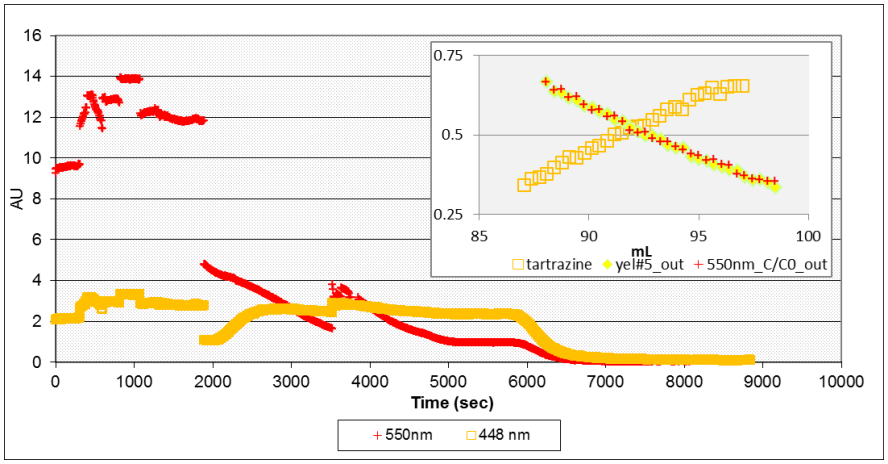

Figure 4: Breakthrough curve from initial test of amaranth reactivity to 25° C Ottawa sand in interwell reactor at pH 7 with a flow rate of 2 ml/min.

We ran the same solution through the same medium heated to 120° C for a preliminary examination for thermal decay products. The inline breakthrough curve suffered from the same shortcomings as with the 25° C BTC, but this curve indicates potential retardation relative to the yellow dye (Figure 5). The poor quality of these initial BTC's doesn't provide confidence about retardation by the quartz and we have begun to design new experiments to address this question. HPLC analysis of the effluent, however, provides evidence that the thermally stable 2,7-naphthalene disulfonate (Figure 1D) was produced by the thermal degradation of the amaranth (data not shown).

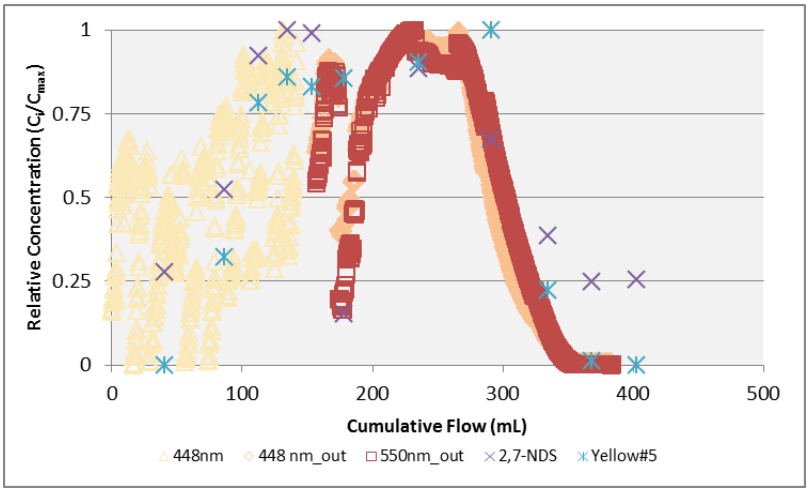

Figure 5: Breakthrough curve of amaranth and yellow #5 eluting through Ottawa sand column heated to 120° C as monitored by inline detectors. Samples were collected and analyzed with HPLC fluorescence and absorption spectra detectors indicating that the amaranth molecule had both 1,5- and 2,7-naphthalene disulfonate as thermal decay products.

Progress this quarter on the determination of the adsorption constant for safranin T with respect to Ottawa sand has provided insight into how this method can be used to the estimate surface area and to provide a temperature profile of a reservoir. It also provided an opportunity to compare the BET surface area measurements of the Ottawa sand with the values calculated from

the area of spheres. This, as well as Dr. Reimus' work, led to the realization that we had used the diameter instead of the radius when the surface areas were previously calculated. Corrected values from those reported earlier are provided in Table 1.

Table 1: Surface areas of selected Ottawa sand fractions based upon geometric mean radii.

Geomedium Analogue	US Mesh Size	Surface Area (m^2)
Coarse Sand	35/30	58.8
Medium Sand (1)	40/35	65.9
Medium Sand (2)	80/49	67.0
Fine Sand (1)	70/45	112
Fine Sand (2)	45/40	80.8

Retardation factors were determined from the ratio of the flow required for the column effluent concentration to reach half of the concentration of the final effluent concentration, as described in earlier reports. The adsorption constant ($K_{d,m}$) was determined from the average of the loading and unloading breakthrough curves from the definition of the equilibrium-based retardation factor (R_f), where ρ_s equals 2.65 kg l^{-1} and n is the porosity determined from the ratio of the 1st moment of the conservative tracer and the column volume: $K_{d,m} = \frac{n(R_f-1)}{\rho_s}$. The graph of these values is shown in Figure 6. Over the range of temperatures tested, the trend seen on this graph shows that the adsorption coefficient trends larger with increasing surface area, but that there is increasing adsorption and variation on the lower temperature geomedium.

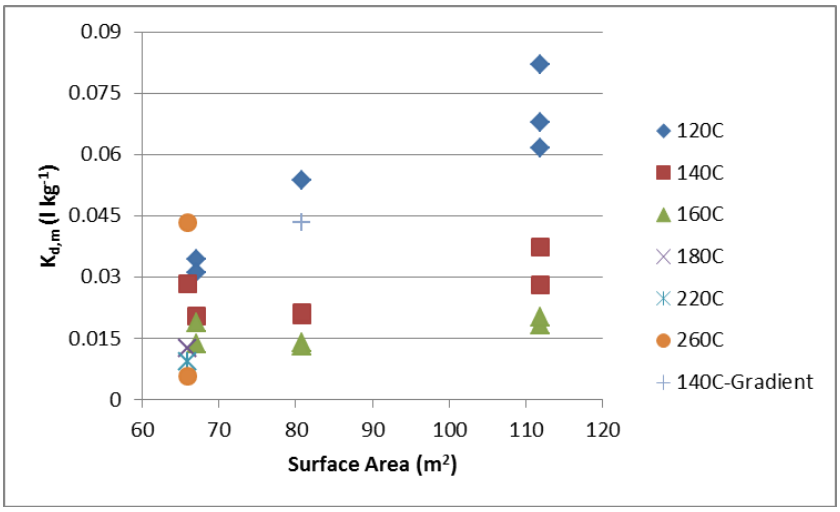

Figure 6: Mass-based adsorption coefficients of safranin T on Ottawa sand determined from simulated interwell step injections showing a clear trend of increasing sorption from columns packed with smaller particle sizes (greater surface area).

When the mass-based adsorption coefficient is adjusted to a surface-area-based coefficient and graphed versus temperature (see Figure 7), the temperature dependence is more pronounced. The relationship between $K_{d,a}$ and temperature empirically indicates that there may be an exponential

effect of temperature on the safranin adsorption, which suggests that the cooler rock near the injection well would have a significant impact on the dye's transport. This conclusion is supported by the data point from an experiment conducted with the inlet temperature set at 120° C and the outlet at 160° C, labeled as fine2-G. The safranin T retardation measured in this experiment was closer to that seen in the 120° C experiments than that measured from the 120° C experiments, but this is not definitive as there was more variation seen in the cooler experiments.

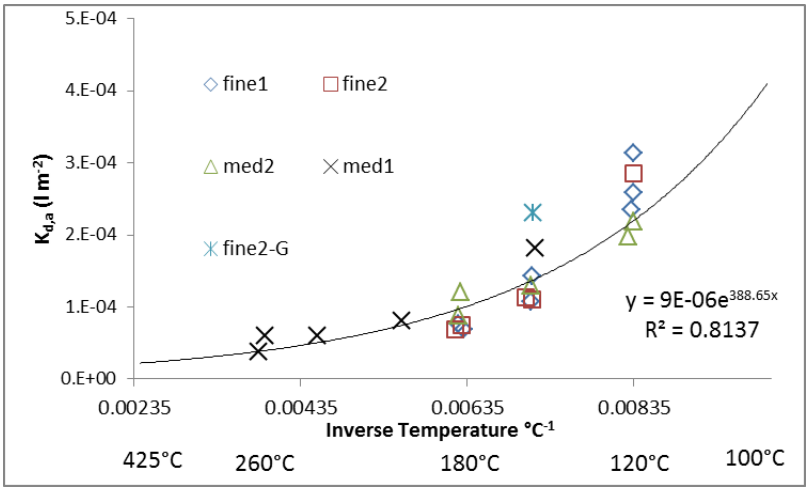

Figure 7: Empirical relationship suggesting that it will be feasible to account for the effect of matrix temperature on retardation factors from reactive tracer tests. This will help to provide better estimates of surface area and could provide thermal profiles of reservoirs from successive injections through the same matrix.

Considering the quartz surfaces from the Ottawa sand used in this series of experiments, these results support the hypothesis that these types of reactive tracers could be used to provide surface area estimates available for heat transfer from geothermal reservoirs, but there are some practical conditions that would need to be addressed about the temperature effect on adsorption. Numerical modeling of the reservoir flow using appropriately sized cell dimensions could be used to separate the effect of temperature from the surface area estimates, but would require *a priori* information about the temperature profile within the reservoir.

Another potential would be to coat the reactive tracer with a polymer that will allow conservative transport until it reaches a section of the reservoir at a target temperature and then release the reactive tracer by melting. Injection of tracers coated with polymers that would melt at different temperatures could be used to concurrently measure the thermal profile of the reservoir. Another use for the temperature dependence of adsorption is in reservoir management. Injection of these types of reactive tracers could be used to monitor changes in a reservoir's thermal profile through the use of sequential injections. Comparison of breakthrough curves after heat extraction with the reactive tracer injection (Figure 8) could indicate the temperature profile using mineralogically appropriate empirical relationships as shown in Figure 7.

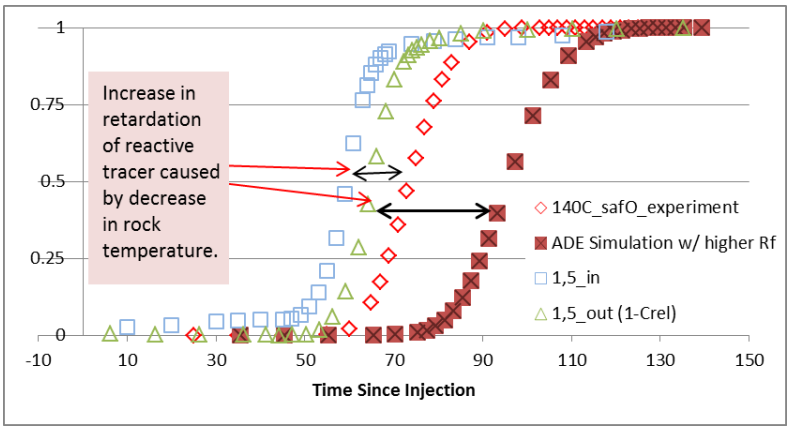

Figure 8: Advective-diffusion equation simulation of sequential reactive tracer injections through reservoir to measure thermal front propagation, assuming that the mineral/tracer interaction is the same for the each tracer test.

One potential caution about these adsorption coefficients is that examination with the advection diffusion equation (ADE) of many of the BTC's indicates that the adsorption of the safranin T is not exhibiting equilibrium behavior. An example graph is shown in Figure 9. The parameters from the nonequilibrium ADE (NADE) for this safranin T experiment through coarse sand at 120° C are $\beta = 0.88$ which is the proportion of adsorption sites exhibiting equilibrium and $\omega = 0.005$ which is the 1st order rate coefficient for the nonequilibrium sorption. This model fitting has only been tested on a small subset of the entire series of experiments to date and of course the model fit does not imply physical processes, so we will continue to examine this issue as it relates to the use of adsorption coefficients for estimation of heat transfer surface area.

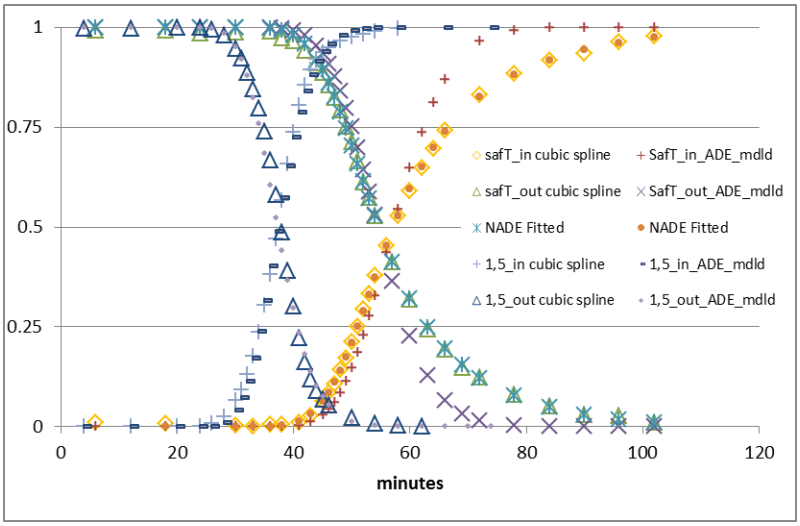

Figure 9: Model fit of one experiment on coarse fraction of Ottawa sand at 160° C showing that the equilibrium-based model accurately describes the conservative tracer, 1,5_NDS, but the safranin T adsorption is not described well by the ADE. The two-site non-equilibrium ADE (NADE) fits the data well.

Third Quarter

Kevin Leecaster, EGI

An experiment was conducted to test the effect of an increase in solution pH on safranin T adsorption in order to examine whether its retardation is primarily through ion exchange reactions with the quartz surfaces. The ionic binding capacity on the hydrated sand grain surfaces are caused by the reaction of the outer layers of metal ions within the quartz crystal structure with water molecules. Reactive sites arise from the siloxane groups along the planar surfaces reacting with water molecules forming silanol hydroxyl groups. As opposed to minerals with Al which can bind protons and exhibit net positively charged surfaces, silanol groups within the tetrahedral sheets only dissociate protons leading to negatively charged surfaces that attract cations from solution. Quartz exhibits this net negative charge down to pH 2 with the magnitude of charged sites depending on the solution pH. Since the negative charge of the mineral surfaces increases with pH, if the cationic safranin T is retarded more by the quartz at higher pH this will indicate that ion exchange sorption predominates.

A laboratory test was conducted through the 1" X 20" column filled with 432 g of Ottawa sand sieved to pass through a 355 μm mesh and retained by a 208 μm mesh heated to 160° C. The flush/equilibration fluid was the same as the previous safranin experiments (200 ppm NaCl, 175 ppm, & 10 ppm tetraethylorthosilicate), but instead of adjusting the acidity to 5.1 as in the previous experiments it was raised to pH 8.5 using NaOH and HCl. The tracer solution was the same with 89 ppm 1,5-naphthalene disulfonate (1,5NDS) and 1.5 ppm safranin T (safT). We monitored the effluent at two wavelengths: 577 nm for the (safT) using a FiaLabs fluorescence flow cell optically connected to a red 507 nm LED and an Ocean Optics USB2000 spectrometer and monitored the 1,5NDS concentration at 310 nm with a ThermoScientific model 4100 photospectrometer. The flow rate through the column, as measured gravimetrically, was 2 g/min with 1,100 psi maintained by use of a back pressure regulator. The fractions collected for flow rate measurements were analyzed using high pressure liquid chromatography (HPLC). HPLC analysis used a Waters 600 pumping system with a model 474 fluorescence detector monitoring emission at 577 and 340 nm and excitation at 505 nm and 224 for safranin T and 1,5 naphthalene disulfonate, respectively. In addition, a model 996 PDA detector was used for helping to identify potential degradation products.

The results of the experiment were satisfactory with definitive hold up of the safranin T although the signal from the inline fluorescence detector was noisy (Figure 10). The pore volume measured in using the method of moments of the inverse of the response to the Heaviside input was 82 ml with less than 0.5% coefficient of variation between the loading and unloading curves. The average 1,5NDS concentration of the 'tread' effluent as measured by HPLC was 87 ppm while the maximum safT concentration was only 1.14 ppm representing only 77% of the tracer concentration. A portion of this may be due to having not reached the 'tread' for the safT because of the high retardation and the noise in the fluorescence detector may indicate that there was some air in the system, but combined with results from previous experiments provides supporting evidence that surface catalysis decreases the thermal stability of this cationic tracer compound. Previous thermal stability tests in ampules indicated that there should have been no thermal decay during the ~1 hour mean retention time the tracer was at 160° C. Unlike in the rhyolitic tuff experiment performed at this temperature there was no detection of decay products in either the PDA or the fluorescent detector.

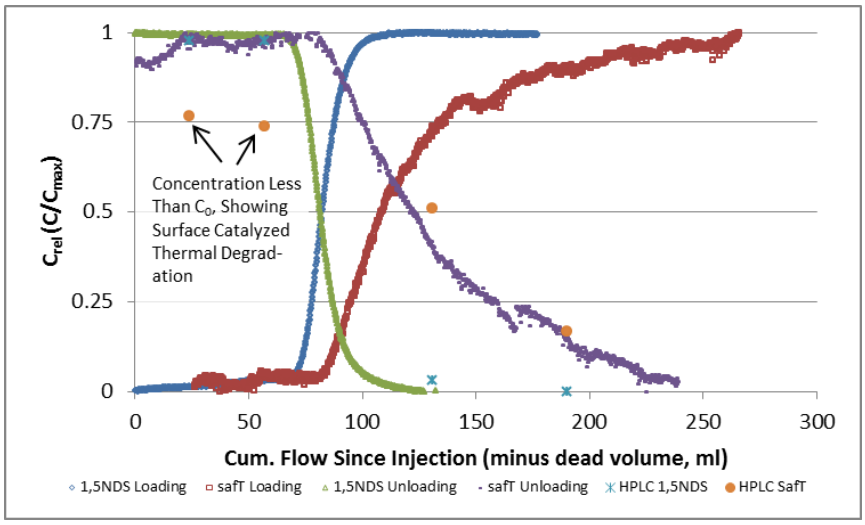

Figure 10: Breakthrough curves of safranin T & 1,5-naphthalene disulfonate through 177 m^2 of Ottawa sand grains (geometric mean particle diameter of 278 µm) at 160° C. The HPLC measured fractions collected during the tracer unloading are shown along with the inline measurements. The time of collection of the HPLC samples have not been corrected for integrated fraction period.

The retardation factors of the safT were 1.3 and 1.5 for the loading and unloading curves, respectively as determined by the ratio of how much flow was required for the effluent to exhibit median concentration of the safT over how much flow until the 1,5NDS was half of the tracer concentration. The surface area based adsorption coefficient from this elevated pH experiment is 50% higher than the average of the pH 5.1 measurements made at similar temperatures (Figure 11). The results of this experiment testing the adsorption of safranin T at elevated pH indicate that at least a significant portion of the observed retardation is caused by ion exchange since its adsorption increased with pH.

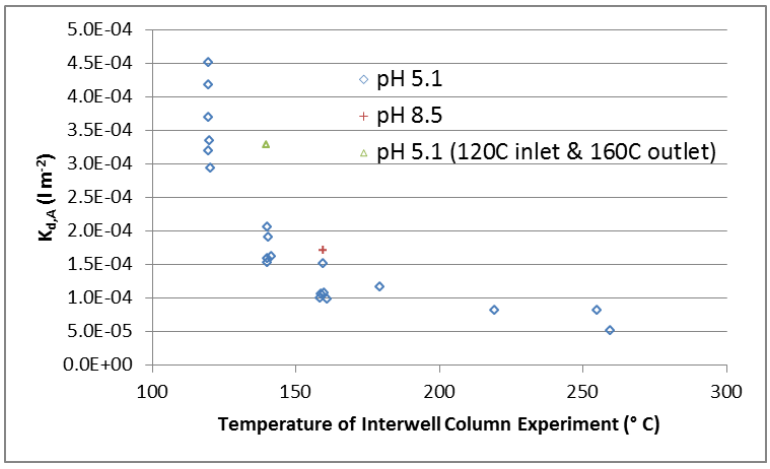

Figure 11: Surface area based adsorption coefficients determined for 1.4 ppm safranin T on Ottawa sand.

We ran follow-up tests examining amaranth dye for its ability to react with reservoir rock surfaces. Last quarter we reported that there was some indication that the amaranth was retarded relative to the conservative tracer tartrazine and that naphthalene sulfonates were formed when the dye decayed in a heated column. This dye might therefore provide a tool for assessing surface area via retardation by degrading to thermally stable fluorescent conservative tracers that will follow a co-injected initial conservative tracer after it is temporarily held up by the newly created fracture surfaces near the wellbore. Plus, it could act as a thermosensitive 'smart' tracer for interrogating reservoir temperatures in lower temperature reservoirs and similar compounds may be discovered for higher temperature applications.

We eluted a solution of 150 ppm NaCl adjusted to pH 8.5 with NaOH & HCl through the 1" X 20" column filled with 432 g of Ottawa sand sieved to pass through a 355 µm mesh and retained by a 208 µm mesh heated to 25° C. Next we switched to the tracer solution of 138 ppm NaCl, 4 ppm amaranth dye (AD), and 29 ppm 3,4-difluorobenzoic acid (DFBA). The column was pressurized to 610 psi with a nominal flow rate of 1.3 g min^{-1}. We monitored the effluent at two wavelengths: 510 nm for the AD using a FiaLabs fluorescence flow cell optically connected to a cool white LED and an Ocean Optics USB2000 spectrometer and monitored 230 nm with a ThermoScientific model 4100 photospectrometer for detection of the DFBA. After the tracer concentrations in the effluent increased to the 'tread' concentration of the step injection the temperature was incrementally raised to 160° C while fractions of the effluent were collected for subsequent HPLC analysis. HPLC analysis consisted of using a Waters 600 pumping system with a model 474 fluorescence detector monitoring emission at 340 nm with 224 nm excitation as well as a model 996 PDA detector. Flow was terminated at the end of the first day's temperature treatment and flow of the AD/DFBA solution was resumed on the next work day for 30 minutes so that retardation of the amaranth at 25° C could be double-checked during column unloading of the dyes from the column.

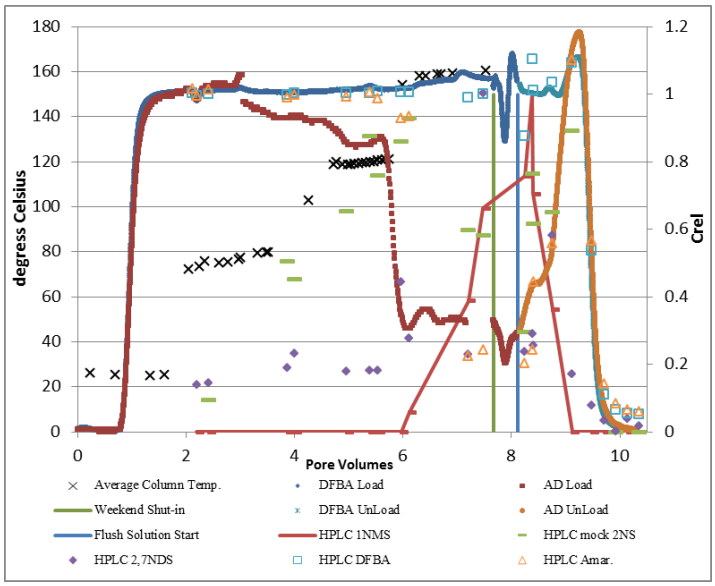

Figure 12. Plot showing the breakthrough of amaranth & DFBA prior to heating the column in stages up to 160C.

The amaranth dye was slightly retarded relative to the conservative tracer as seen in Figure 13 indicating that it reacted with the 177 m^2 of quartz surface area in the column at the solution pH of 8.5. The retardation factor during column loading as determined by the ratio of the flow until the median concentration of each tracer eluted was 1.02 and it was 1.03 when unloaded from the column. The pore volume in the column was 91ml as determined by the method of moments for the loading and unloading of the DFBA with a coefficient of variation of 0.86%. This could not be done for the unloading curve of the AD since the column had been shut-in over the weekend resulting in it not having an initial condition of a step injection.

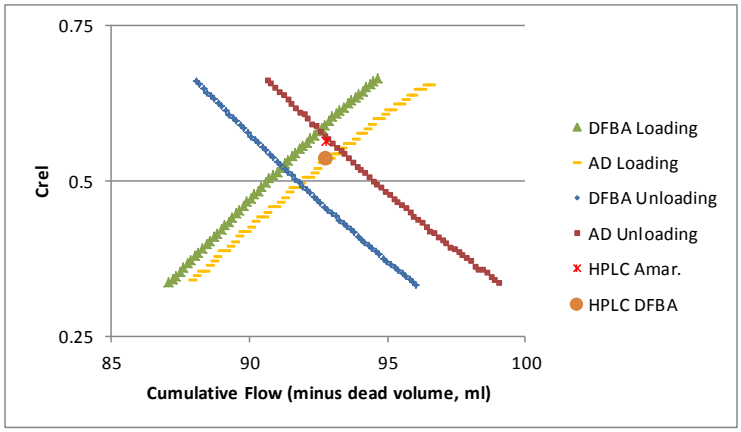

Figure 13: Linear portion of the breakthrough curves showing retardation of the amaranth dye relative to the 3,4-difluorobenzoic acid.

This retardation factor, while not large, does indicate that with this solution pH the amaranth dye interacts with the surface of the Ottawa sand. Since geothermal waters are so well buffered by the reservoir mineral assemblages it is possible that adjusting the pH of the injection fluid would not be sufficient in order to induce reactivity of such weak cations. Adding fluoride to the injection fluid would increase the density of negatively charged surface sites on the rock surfaces because (at least in near-surface groundwater temperatures) it reversibly exchanges with hydroxyl acting to both increase the surface reactivity by raising the solution pH and creating temporary negatively charged sites on the mineral surfaces. Quartz has very low surface activity compared with most geothermal reservoir minerals. The amaranth (or similar candidate reactive tracers) would probably demonstrate the same trend as the other candidate molecules tested of being retarded to a larger extent by more reactive minerals like mica, illite, or plagioclase. Also, as demonstrated for all of the reactive tracers tested to date in our lab, the molecules' reactivity with the surfaces decreases with increasing rock surface temperatures, so the breakthrough of these thermosensitive tracers needs to be examined at elevated temperatures.

The main aspect that makes this type of reactive tracer worth exploring despite its relatively high thermal decay rate is the potential for the decay products to be thermally stable detectable tracers that behave conservatively to the reservoir media. After the parent molecule has reacted (stalled) on the newly created fracture surfaces and subsequently breaks down, the daughter products can flow with the reservoir (or fracking) fluid either back to the injection well in an injection/backflow type withdrawal or on to a connected well within the same system as in an interwell tracer test. As shown on Figure 12, 2,7-naphthalene disulfonate was in the first

fractions collected and it appeared at a high enough concentration to verify its identity with a PDA spectrum (Figure 14). 1-naphthalene sulfonate didn't start to appear until 2 pore volumes after the column temperature was raised to 120° C, but didn't show up in a high enough concentration for PDA spectrum collection. There was a fluorescent compound that eluted almost identically as 2-naphthalene sulfonate (Figure 15) soon after raising the column temperature, but its spectra indicates that it is not 2-naphthalene sulfonate (Figure 16). The formation pathway for 2-naphthalene sulfonate from the amaranth dye molecule would be more complex than for the other two naphthalene sulfonates. It would be beneficial to examine rate coefficients and stoichiometry of the chemical reactions to help interpret return curves.

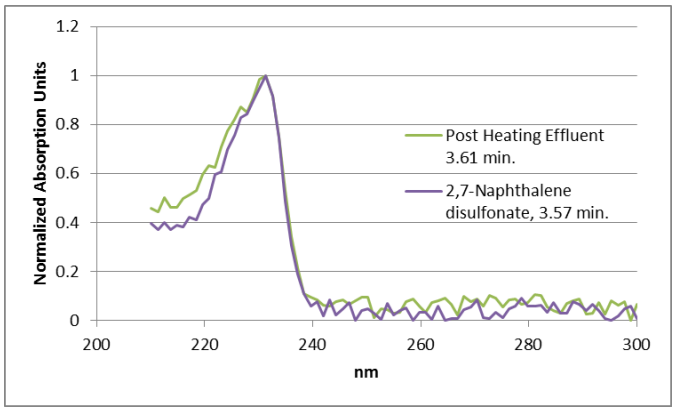

Figure 14: Spectra of 2,7-naphthalene disulfonate and a sample collected from heated column flowing amaranth dye confirming its formation in the simulated geothermal reservoir.

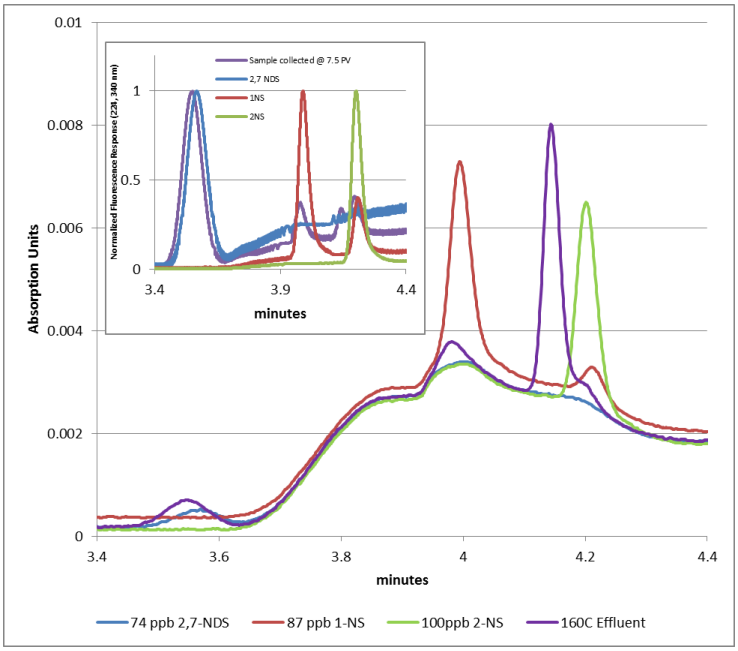

Figure 15: Chromatograms of 2,7-naphthalene disulfonate, 2-naphthalene sulfonate, 1-naphthalene sulfonate and a sample collected from heated column flowing amaranth dye.

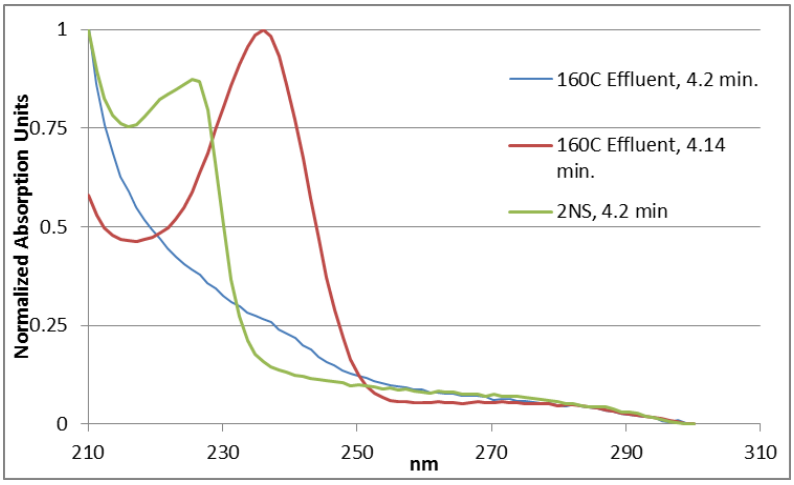

Figure 16: Spectra of 2-naphthalene sulfonate and a sample collected from heated column flowing amaranth dye indicating that this fluorescent compound is not 2-naphthalene sulfonate.

A new preheating system was designed and built for the interwell reactor in order to try to avoid the persistent leaks that form in it. A solid state relay burned out, almost literally as it got stuck in the on position and confirmed the benefit of having a separate temperature limiter installed in series with the heaters. Para-toluene sulfonic acid and PFBS were also evaluated this quarter for use as conservative tracers, but detection of these compounds with our lab's equipment would not provide a low enough detection limit as they both have maximum absorption in the deep UV range.

Mike Mella, EGI

This quarter we evaluated Rhodamine WT as an adsorbing tracer. Flow experiments were conducted on shale, rhyolitic tuff, and Ottawa sand. In each of these experiments the same type of column and packing procedures were used as in previous experiments. In each case the flow rate for these experiments was 2.0 ml/min. Individual samples were collected and analyzed via UPLC rather than by inline detection. Discrete sampling results in loss of tracer resolution; however, for this series of experiments chromatographic separation was necessary due to the presence of two different isomers of Rhodamine WT. Rhodamine WT dye typically comes as a mixture of two different isomers as shown below in Figure 17.

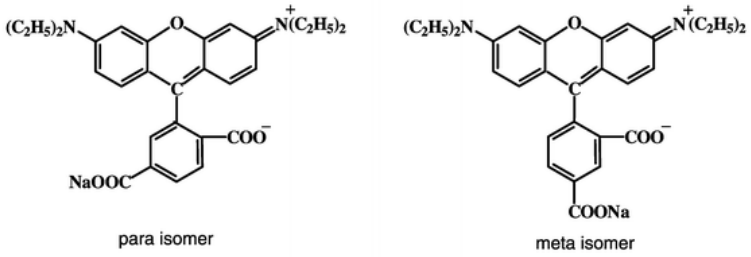

Figure 17. Para and meta isomers of Rhodamine WT.

These two isomers fluoresce at the same wavelengths and therefore it would be difficult to separate the signal of one from the other inline. It was also apparent that the two isomers adsorb differently. The para isomer (RWT 1) was more conservative than the meta isomer (RWT 2).

The first experiments were conducted on a shale column. The shale in this column was cuttings obtained using diesel-based mud. These cuttings were washed with DCM to remove most of the organic material, but it is likely that some organics remained. The results on the shale showed that both isomers were retarded at room temperature and at an elevated temperature of 170°C. The Rhodamine WT isomers in the room temperature experiment adsorbed so well that the experiment had to be stopped at the end of the day and resumed the next 2 days. The plot for the room temperature shale experiments is given below as Figure 18.

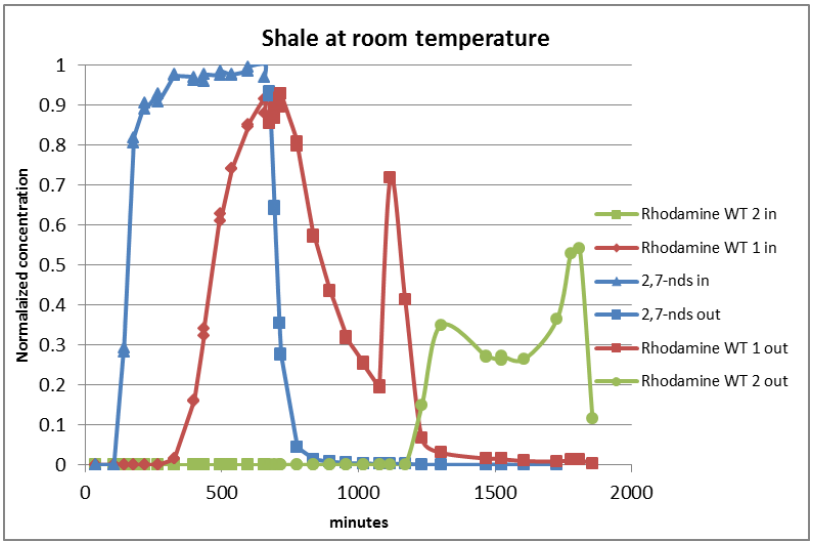

Figure 18. Rhodamine WT flow experiment through shale column at room temperature.

This experiment showed that RWT 1 was strongly adsorbed at room temperature and RWT 2 was even more strongly adsorbed. The experiment was repeated at 170°C and once again the same trend of adsorption was seen. The plot for the Rhodamine WT through this column is shown below and labeled as Figure 19.

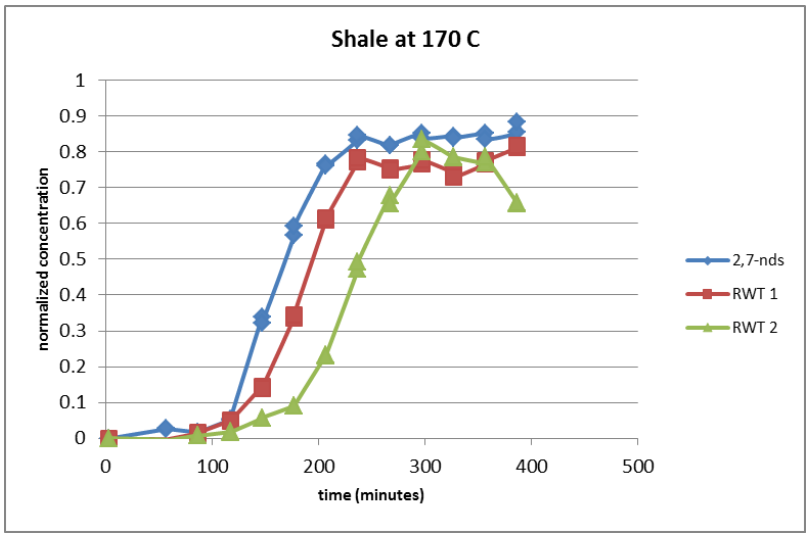

Figure 19. Rhodamine WT flow experiment through shale column 170°C.

We encountered some difficulties in the flow-out portion of this experiment so the out curves were not available. We used a step input for the introduction of tracer. However, the step input led to very long tracer loading and unloading from the column. We decided to try a pulse-type tracer injection to see if it would be feasible. A pulse of 2,7-nds and RWT was injected and discrete samples were again collected. The results are plotted below in Figure 20.

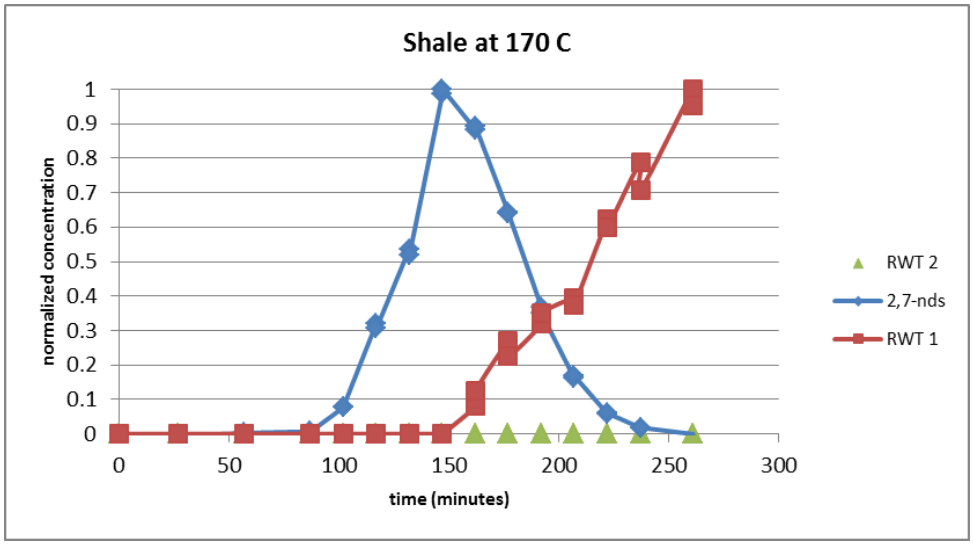

Figure 20. Rhodamine WT impulse injection flow experiment through shale column 170°C.

From the plot it can be seen that the pulse method does not give the same resolution as the step input method but it does seem to give enough resolution to screen for adsorption of tracers. In this experiment we once again saw that RWT 1 was retarded relative to 2,7-nds, but the experiment was not run long enough to see RWT-2 come off the column.

Experiments of RWT on an Ottawa sand column were run at 170°C as well to see how well RWT adsorbed in a more quartz like formation. A pulse injection was used again and the return is plotted below in Figure 21.

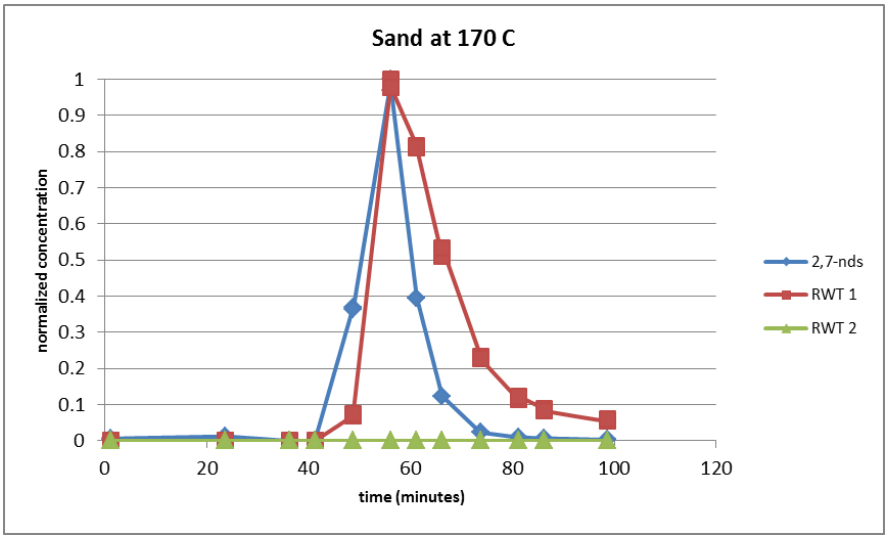

Figure 21. Rhodamine WT injection in sand column at 170°C.

From the plot it can be seen that RWT 1 may have been retarded a little bit with respect to 2,7-nds but RWT 2 never was detected.

A test of RWT sorption was also made with a column filled with rhyolitic tuff. A pulse injection was made into this column and run at 170°C at 2 ml/min flow rate. The results of the test are shown below as Figure 22.

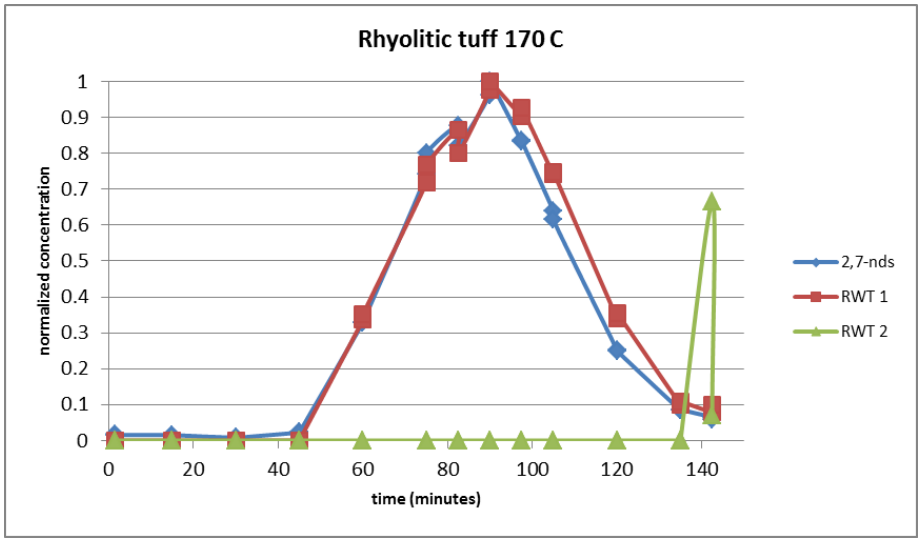

Figure 22. Rhodamine WT injection in rhyolitic tuff column at 170°C.

The RWT 1 isomer showed little if no retardation relative to 2,7-nds and RWT 2 may have been coming out when the experiment was terminated but it is difficult to tell. It is possible that this isomer is not as thermally stable or if may irreversibly adsorb to rock.

Overall it would appear that Rhodamine WT is not a good candidate for a reactive tracer in traditional geothermal fields. RWT 1 isomer looks like it would not be retarded much it at all and RWT 2 isomer looks like it would be retarded too much or would not return at all. Rhodamine WT, however, might be a good tool to evaluate the surface area interrogated by a hot water or steam pulse.

Fourth Quarter

Newberry Injection-Backflow Reactive Tracer Test

Preliminary progress has been made with evaluation of the reactive tracer/mineral interaction in support of the Newberry EGS injection/backflow test. A reactive tracer will travel into and out of a reservoir slower than the bulk injection fluid due to its interaction with the rock surface. This will be manifest in the breakthrough curve (BTC) relative to a conservative tracer (Figure 23).

The difference in the transport of the surface-sorbing reactive tracer relative to that of the transporting fluid is related to the amount of surface that the reactive tracer interrogates and in a flow and transport model can be described by a distribution coefficient. The tracer/surface area interaction is governed by the fluid chemistry, mineralogy, and physical conditions, so the coefficient should be determined under conditions similar to those in the field or by adjusting the coefficient to account for the effect of different field conditions on the reactive tracer's retardation. Estimating and bounding this coefficient has been the focus of this quarter's research.

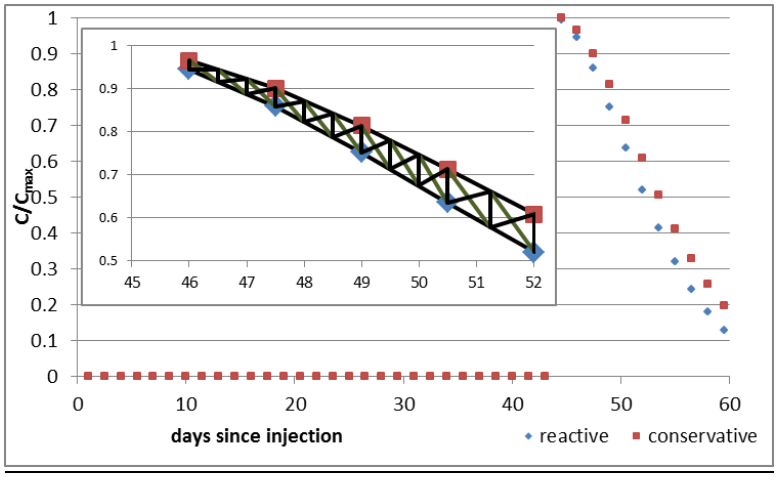

Figure 23: Hypothetical production curve from an injection-backflow tracer application after shut-in. Assuming that the conservative tracer behaves identically to the bulk fluid, the area of the difference between the reactive and conservative tracer production curves represents the amount of reactive tracer retained within the formation. The relationship between surface area and retention has to be established

for the mineralogy, chemistry, pressure, temperature, and the flow regime encountered by the injection fluid.

Methods

Based on the assumption that the Newberry hydraulic fracturing will be performed with groundwater collected from well 29, we attempted to recreate an analogue solution for use in laboratory experiments. Analysis of the pad 29 water for major constituents indicates that it has high concentrations of Mg and Si. The reported concentrations (mg l^{-1}) of major cations and anions are: Na (44), Ca (19), Mg (25), K, (5), SiO_2 (60), HCO_3 (290), Cl (3.5), and SO_4 (2.5) with a pH of 8. Initially a similar solution was made from: 17 mg $KHCO_3$; 88 mg $(MgCO_3)_4$-$Mg(OH)_2$-$(H2O)_5$; 43 mg $CaCO_3$; 235 mg $NaHCO_3$, 175 mg H_4SiO_4; 30 mg HCl, and 6 mg H_2SO_4. The pH of this solution was brought to 8 by adding additional HCl. It wasn't possible to dissolve all of the material so it was filtered to remove particulate matter prior to pumping it through the geomedium. This recipe was adjusted for reasons discussed in the results and discussion section below.

A preliminary geomedium was constructed from available material for performing initial tests of the alkali/halide salt tracers. The medium was mixed together from 33% (by weight) each of ground and sieved particles of calcite and albite and sand grains of quartz that had been sieved to be between 0.425 – 0.5 mm. Assuming smooth spherical particles of a radius of 0.023 cm and a density of 2.65 g cm^{-3} the specific surface area ($SA_{sphere} = 3/\rho r$) would provide a nominal surface of 49 cm^2 g^{-1}. This medium, labeled trimix461, was 'annealed' overnight at 400° C; then 344 g was packed with borosilicate glass wool filter plugs at both the inlet and outlet into a 1" x 20" SS column to a bulk density of 1.35 g cm^{-3}. After equilibration of the trimix461 geomedium to the simulated pad 29 water, inter-well column retardation experiments were performed.

Two pulses each of tracer solutions were constructed by diluting the readily available alkali salts LiBr and $CsCO_2H$ at the same concentration of 1.2 millimolal into the flush solution. Disodium 1,5-naphthalene disulfonate (NDS) was added to both solutions to act as a conservative tracer. The lithium solution had 30 micromolal NDS while the cesium solution's NDS concentration was only 4.7 micromolal. The solutions were pumped through the column at a nominal rate of 2 g min^{-1} of effluent measured gravimetrically. Inlet and outlet column temperatures were maintained at 120° C as measured by K type thermocouples embedded at least 1 cm into the porous medium. Liquid water conditions were supported by a back pressure regulator set to 100 bar as measured by the Beckman M114 HPLC pump. Fractions of effluent were collected in flint glass test tubes in aliquots of either 4 or 8 ml and samples from selected test tubes were filtered and analyzed by cation exchange and/or reverse phase chromatography by conductivity, UV absorption at 195 nm, and fluorescence at 224 nm excitation and 340 nm emission wavelengths.

The least squares optimization program CXTFIT ver. 2.1 (Toride *et al*, 1995) was used from within the graphical user interface STANMOD ver. 2.2 (Simunek *et al*, 1999) to estimate the average pore water velocity and dispersion coefficient from the BTC of each of the conservative tracers. The analytical solution for pulse input boundary condition with constant initial concentration condition used by CXTFIT for the equilibrium ADE is (van Genuchten and Alves, 1982):

$$c(x,t)=\begin{cases} c_i+(c_0-c_i)A(x,t) & 0 < t < t_0 \\ c_i+(c_0-c_i)A(x,t)-c_0A(x,t-t_0) & t > t_0 \end{cases} \quad (1)$$

where c(x, t) is the concentration at distance x from the inlet at time t, c_i is the initial effluent concentration, and c_0 is the tracer solution concentration. A(x,t) equals

$$A(x,t)=0.5\left(erfc\left[\frac{Rx-vt}{\sqrt{4DRt}}\right]+\exp(P)erfc\left[\frac{Rx+vt}{\sqrt{4DRt}}\right]\right) \quad (2)$$

where R, v, and D are the retardation factor, pore water velocity, and dispersion coefficient, respectively, P is the Peclet number ($P=vx/D$), and erfc is the complementary error function ($erfc(x)=\frac{2}{\sqrt{\pi}}\int_x^\infty e^{-t^2}dt$). Retardation of the conservative tracers was evaluated by performing optimization of R, but it did not appear to be substantial since this resulted in values very close to unity (data not reported) with no systematic difference between whether they were greater than or less than 1. Therefore a tracer-medium interaction was assumed not to occur (i.e. $R_f = 1$). The mean v and D estimated values of the 11 conservative tracer BTC's from the four experiments were used for the modeling of the additional parameters for retardation and nonequilibrium coefficients. This helps to avoid estimation of too many parameters from the small sets of data available from collected fractions and to increase the confidence of the estimates.

Non-linear least squares optimization with CXTFIT was also used to estimate the geomedium's retardation of the reactive trac.. The non-equilibrium ADE provided a better fit to the data than did the equilibrium ADE. Since conservative tracer analysis revealed no physical disequilibrium, the two-site non-equilibrium advective dispersion equation (NADE) was fitted. Van Genuchten (1976) provided analytical solutions of the NADE used in CXTFIT for these initial and boundary conditions:

$$\lim_{x\to 0+}\left(c_{eq}-\frac{1}{P}\frac{\partial c_{eq}}{\partial x}\right)=\begin{cases}1 & 0\le T<T_1\\ 0 & T\ge T\end{cases} \quad (3)$$

$$\lim_{x\to\infty}\left[c_{eq}(x,T)\right]=0 \quad (4)$$

$$c_{eq}(x,0)=c_{neq}(x,0)=0 \quad (5)$$

as:

$$c_{eq}(Z,T)=\begin{cases} c_1(Z,T) & 0 \le T < T_1 \\ c_1(Z,T)-c_2(Z,T-T_1) & T \ge T_1 \end{cases}$$
$$c_{neq}(Z,T)=\begin{cases} c_2(Z,T) & 0 \le T < T_1 \\ c_2(Z,T)-c_2(Z,T-T_1) & T \ge T_1 \end{cases} \quad (6)$$

where Z and T are the dimensionless variables for distance (z/L) and time (vt/L), respectively. The concentrations of solutions in contact with equilibrium sites (c_1) and disequilibrium sites (c_2) are:

$$c_1(Z,T)=G(Z,T)\exp\left(-\bar{\alpha}T/\beta R\right)+\frac{\bar{\alpha}}{R}\int_0^T G(Z,T)H_1(T,\tau)d\tau \quad (7)$$

$$c_2(Z,T)=\bar{\alpha}\int_0^T G(Z,T)H_2(T,\tau)d\tau \quad (8)$$

where α is the first-order rate coefficient for the time dependent sites(T^{-1}), G(x,t) and $H_2(T, \tau)$ are defined below, and the dimensionless variables are defined in table 1.

$$G(Z,T)=\frac{1}{2}erfc\left\{\sqrt{\frac{P}{4\beta RT}}(\beta RZ-T)\right\}$$
$$-\frac{1}{2}\left(1+PZ+\frac{PT}{\beta R}\right)\exp(PZ)erfc\left\{\sqrt{\frac{P}{4\beta RT}}(\beta RZ+T)\right\}$$
$$+\sqrt{\frac{PT}{\pi\beta R}}\exp\left\{\frac{-P(\beta RZ-T)^2}{4\beta RT}\right\} \quad (9)$$

$$H_1(T,\tau)=\exp(-u-v)\left\{\frac{I_0(\xi)}{\beta}+\frac{I_1(\xi)\left(u/v\right)^{1/2}}{1-\beta}\right\} \quad (10)$$

$$H_2(T,\tau)=\exp(-u-v)\left\{\frac{I_0(\xi)}{1-\beta}+\frac{I_1(\xi)\left(v/u\right)^{1/2}}{\beta}\right\} \quad (11)$$

where I_n is the modified Bessel function to the n^{th} order.

Table 1: Dimensionless variable definitions for the two-site chemical NADE used in CXTFIT to estimate retardation factors and rate constants of the sorbing tracers.

$C_1 = \frac{C - C_i}{C_0 - C_i}$	$C_2 = \frac{S(1-f)(C - C_i)}{(1-f)(C_0 - C_i)}$	$\beta = \frac{\theta + \rho k_d R_n}{\theta + \rho k_d R} = \frac{R_n}{R}$
$\bar{\alpha} = \alpha L / q$	$u = \bar{\alpha} / \beta R$	$v = \frac{\bar{\alpha}(T - \tau)}{(1-\beta)R}$
$R_n = 1 + \rho k_d / \theta$	$\xi = \sqrt{4uv}$	$\omega = \omega(1-\beta)\rho k_2 / v$

With accurate and complete breakthrough curve data (Leij & Dane, 1991), the most robust method for estimating transport parameters is with the method of moments (MoM) (Yu, et al, 1999). The first product moment of a breakthrough curve is the mean residence time (MRT), provided by the equation

$$MRT = \frac{\int_0^\infty tC_N dt}{\int_0^\infty C_N dt} - \frac{t_o}{2}$$

where t is time, C_N is the normalized concentration, and t_o is the application pulse length. The ratio between the MRT's of the reactive and conservative tracers provides the retardation of reactive solute in relation to the solvent. An alternate method (Yu, et al, 1999) to calculate the first moment from a step input is

$$MRT = \int_0^1 t dC_N \ .$$

When the integral is calculated with cumulative flow instead of elapsed time the first moment provides the mean residence volume or the pore volume (V_p) of the porous medium. Mass flow rate measurements are converted to volume based on standard temperature and pressure conditions of water. Cumulative flow is corrected to represent the column travel time by subtracting the dead volume of the system (i.e. pump pulse dampener, preheater and cooling tube volumes). Conversion back to a time basis for analysis with the ADE and NADE is performed by division by the estimated average flow rate. Integrals are estimated by the trapezoid method.

Results and Discussion

Initial column flow was performed at lower temperatures as there was a malfunction with the heaters, but even near room temperature the interaction of the solution with the medium resulted in elevation of the pH of the effluent to 9. So in order to obtain a solution that would be in equilibrium with the geomedium minerals, the effluent was collected, filtered, pH adjusted, and re-eluted through the column. This still did not result in stabilization of the pH (Figure 24). As seen in the downward trend of pH of the effluent between the 2nd and 3rd elutions, it appears that

successive recirculation may have eventually produced an equilibrated solution, but the decision was made to not spend the time in order to be able to begin the retardation experiments.

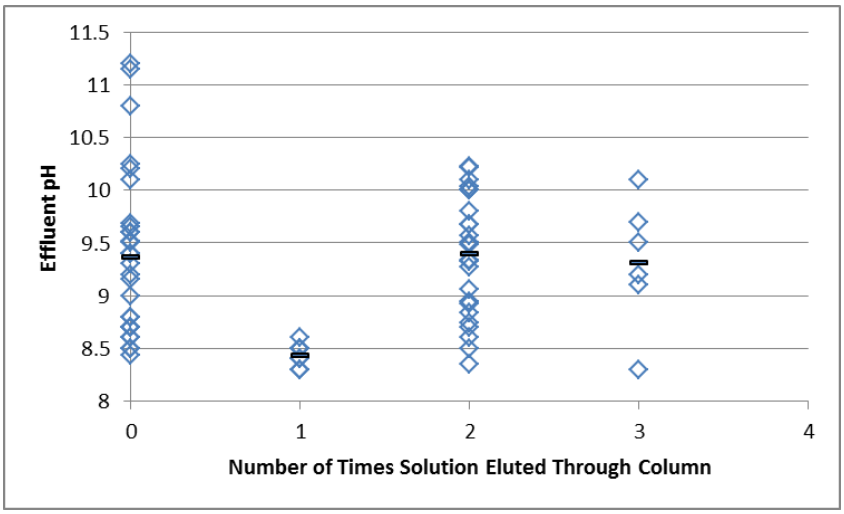

Figure 24: Measured pH of effluent from column filled with 461trimix. Wide variation of the measurements is due to the variety of temperatures to which the solutions were subjected. The steady pH values from one-time-through were from when the column was consistently held at 50° C.

These pH results are not necessarily indicative of how the injected fluid in the field will behave as this geomedium doesn't provide an exact analogue for the minerals that will be exposed during the Newberry stimulation. The injection fluid in the field will not have been equilibrated with the mineralogy either. So these conditions, with an increase in pH, may simulate the field response better than would an equilibrated flow solution. Another observation was that even though these solutions were filtered they accelerated deterioration of the pump's piston seal. The increase of the pH caused by the interaction between the pore water and these minerals is similar to what we've encountered when eluting through geomedia constructed of just quartz (Figure 25) and is assumed to be due to quartz dissolution.

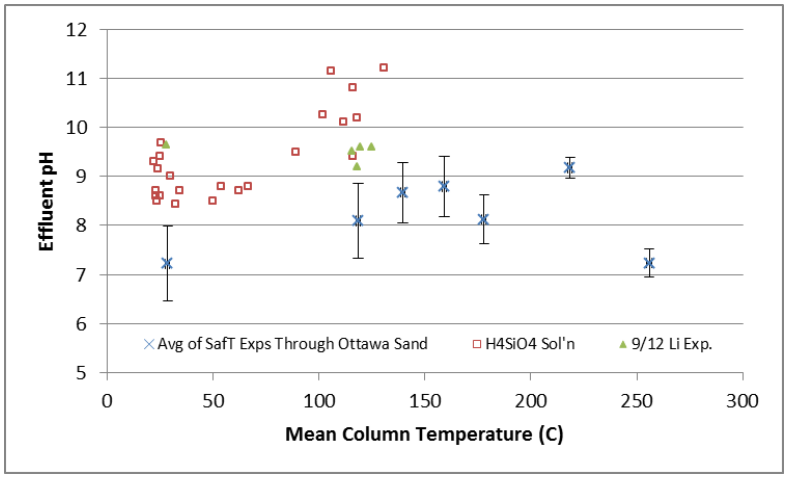

Figure 25: Increase in the pH of the column effluent from two geomedia. The pH of the eluent in the safranin T experiments was 5 whereas in the Newberry tests the eluent pH is 8, but otherwise there seems

to be a similar trend. There is some indication that another reaction begins to occur at the higher temperatures moderating the pH elevation.

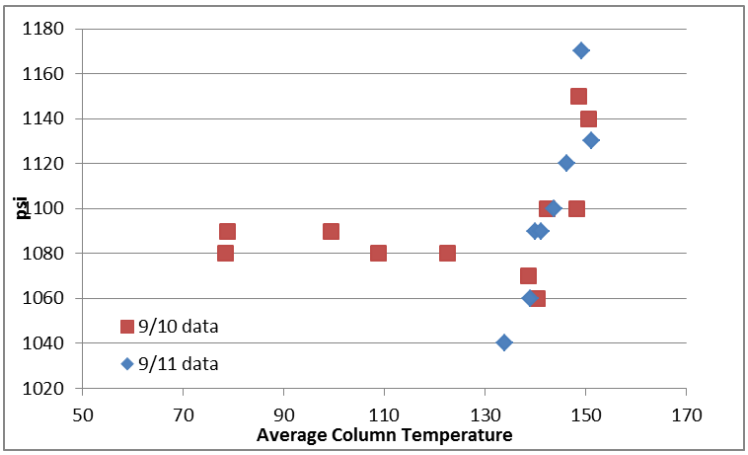

Figure 26: Increase in pressure necessary to maintain flow at 2 g min-1 as the column was heated indicating scale formation within the preheater or porous media.

Another potentially important observation was that the pressure necessary to maintain the standard flow rate of 2 ml m^{-1} increased while pumping (Figure 27), potentially caused by a decrease in permeability. Two of the most likely causes for the decrease in permeability are either precipitation of minerals and/or thermal expansion. Thermal expansion of the quartz sand was experienced in the safranin T experiments as indicated by a decreasing pore volume with temperature (Figure 27). In the sand experiments we didn't observe this increasing backpressure with temperature and since quartz has a coefficient of thermal expansion more than twice that of calcite and albite (Mukhopadhyay, 2009) thermal expansion wouldn't seem to be responsible for the decrease in permeability. An additional indication that scaling may be occurring is provided by thermodynamic modeling of the solution chemistry. Chemical speciation simulation of water with component concentrations as reported for the pad 29 groundwater samples using Minteq indicates that it is supersaturated for quartz and dolomite at 25 °C and predicts that talc would begin to precipitate by 75 °C, at equilibrium. The pump pressure increase over the course of the first Li experiment is shown in Figure 28.

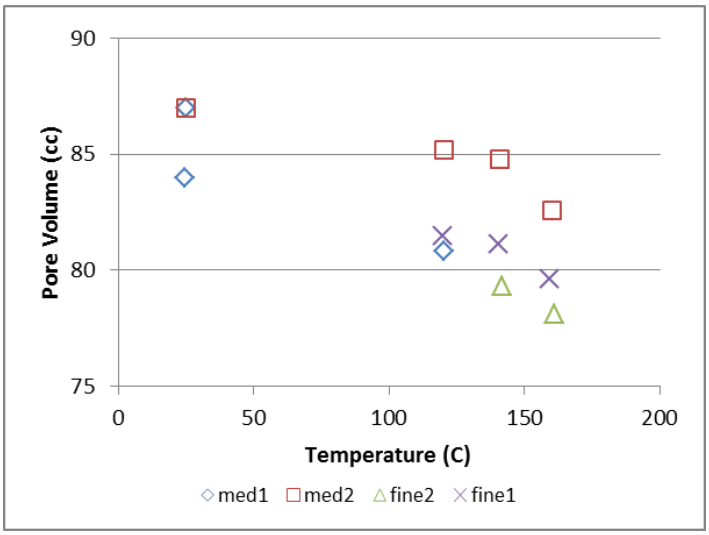

Figure 27: Decrease in Ottawa sand pore volume from thermal expansion of the quartz grains as measured by the first moments of the conservative tracer breakthrough.

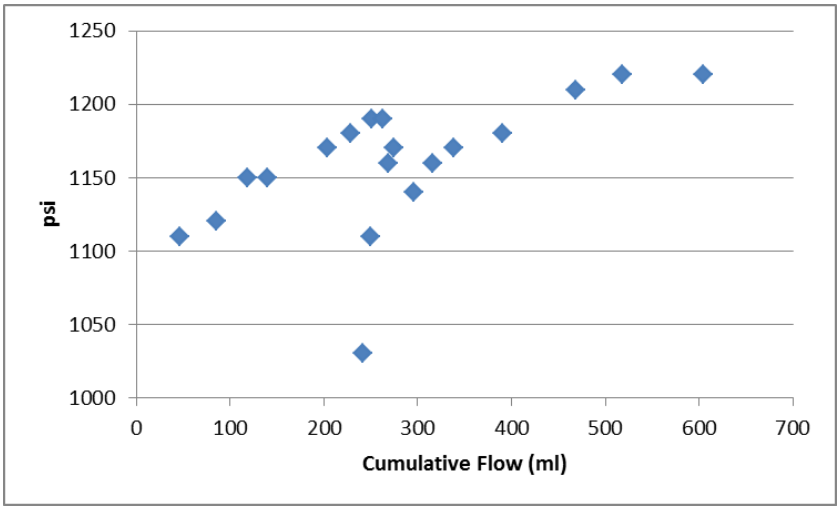

Figure 28: Pressure increase over the course of a Li retardation experiment at 120° C through 461trimix on 9/12/12 indicating scale buildup.

Because of the difficulty dissolving all of the components in the first well 29 analogue solution-chemistry recipe and because the solution required pH adjustment every day in order to lower its pH back to 8, we next made a well 29 analogue solution using sodium metasilicate for the Si in the solution and didn't use any sodium bicarbonate, adding carbonate to the system by sparging with carbon dioxide to lower the pH to 8. This solution still formed precipitates and the pH increased during overnight storage so we decided to lower the Si and Mg concentrations as well as that of Ca. After a few iterations, the final recipe selected for the initial trial alkali-metal-salt retardation experiments decreased the Ca, Mg, and Si salts by ½, ¾, and $^{5}/_{6}$ respectively: 12 mg $KHCO_3$; 25 mg $(MgCO_3)_4$-$Mg(OH)_2$-$(H_2O)_5$; 25 mg $CaCO_3$; 25 mg Na_2SiO_3-$(H_2O)_5$; 14 mg HCl, and 4 mg H_2SO_4. The resulting component concentrations are (mg l^{-1}): Na (5.4), Ca (10),

Mg (6.3), K, (4.7), H_4SiO_4 (31), CO_3 (34.5)* prior to sparging with CO_2, Cl (13.6), and SO_4 (3.2).

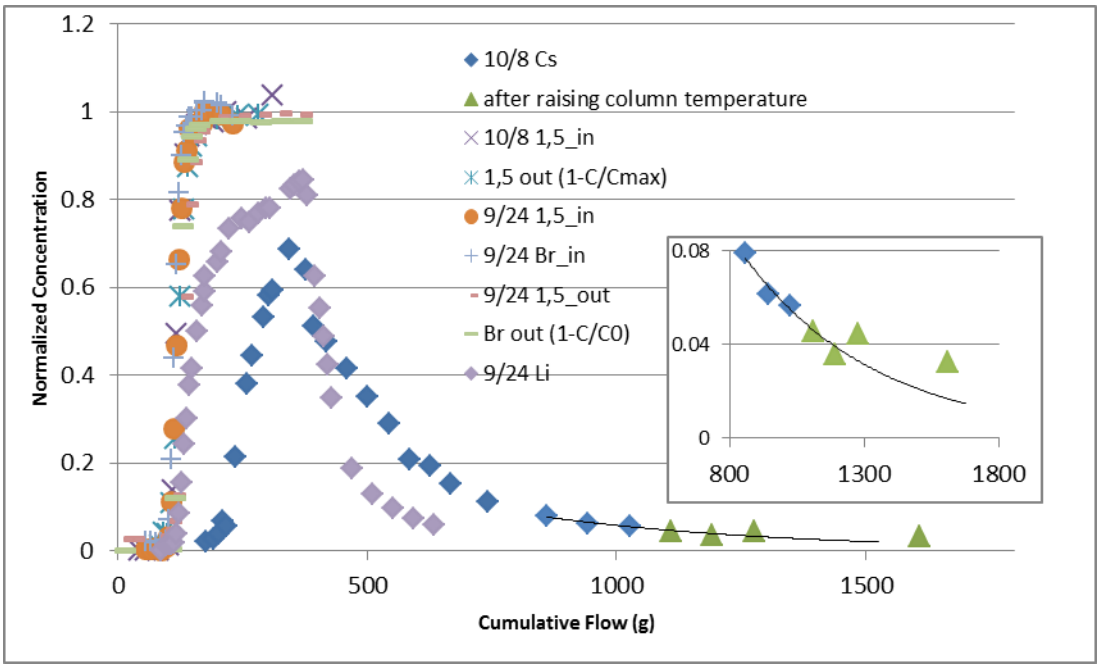

Figure 29: Breakthrough curves from the 272 g pulse of LiBr and the 260 g pulse of CsCO2H through the trimix461 geomedia at 120°C showing expected lyotropic series behavior of the cations. The inset graph focusing on the section of the Cs BTC just before and after increasing the temperature of the column indicates that the geomedia will exhibit less retardation of the alkali metals at higher temperatures.

Cesium was retarded by the trimix461 geomedium to a greater extent than Li as seen in the example BTC shown in Figure 29. Li begins to elute soon after the conservative Br and NDS plus is desorbed from the column sooner than the Cs despite having had a 5% larger pulse applied. The ADE described the conservative tracer BTC well with coefficients of determination greater than 0.99 whereas the reactive tracers' transport was not well described by the ADE (Figure 30). The 2-site NADE provided a much better fit and could probably be made significantly better through weighting the observations (Tang, 2010), especially around the inflection points. This NDS curve demonstrates the general concern when collecting fractions for use in estimating model parameters that there should be enough data points along the BTC to exceed 10 times the number of parameters being fit.

Using the method of moments, the parameter estimation (like MRT) is significantly affected by sample frequency and duration (Das *et al*, 2005). Mass recovery estimates of the otherwise fairly well characterized curve from the 80-minute Cs pulse were 111% for the conservative tracer and 44% for the reactive tracer, but all of these reactive tracer curves should be exponentially extrapolated and integrated to obtain better moment estimates. For many types of BTC's, earlier experience has shown that integrating splined polynomials fit over portions of the curves can improve estimates compared to simple trapezoids (data not shown).

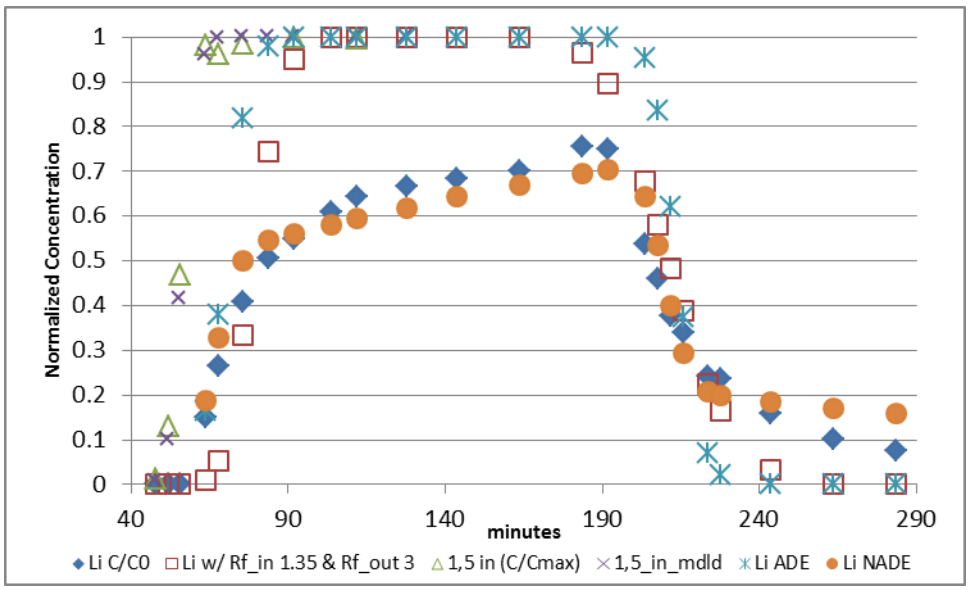

Figure 30: Observed and modeled data from the 300 g pulse of LiBr showing that the NADE linear optimization fit model best describes the data. While the ADE provides a good fit to the conservative tracer there is a paucity of data for confidently estimating flow parameters from a single BTC. There appeared to be a significant difference in the desorption and adsorption portions of the BTC so an attempt was made at fitting the curve by using different R_f's for the construction of the curve prior to and after the tracer pulse. While it 'fit' the data better this approach may not be appropriate and besides it still didn't help describe the tailing that the 2-site NADE or dual porosity models better predict.

Table 2 provides calculated moments and ADE parameters calculated from the BTC's through the trimix461 at 120 °C. There is good agreement between separate experiments and the calculated pore volume as well as no apparent trend over time so there doesn't seem to be significant, lasting change in the porosity caused by the scale formation. This indicates that the scale may be forming in the preheater and this would also support a thermally induced precipitation reaction as the preheater subjects the fluid to a higher temperature than the one targeted for the column medium.

Values of K_d for this geomedium under these conditions calculated as $n/\rho(R_f - 1)$ are listed in Table 3. As seen in the table the values are higher than when Li was eluted through a column filled with only Ottawa sand, experimental conditions were reported in previous quarterly, and correlate well with Cs distribution coefficients reported by Akiba and Hashimoto (1989) for a suite of minerals. Figure 31 shows the values they measured along with the ones from this study. There is a large difference of 1 to 2 orders of magnitude difference that could indicate a significant temperature effect on sorption or could be due to other different conditions between the studies. Typically at near-surface temperatures there is an increase in the distribution coefficient with temperature due to faster reactions and higher diffusion rates, but as temperatures increase above ion specific critical points the ion's inertial energy exceeds the forces driving surface adsorption and diffuse double layer retardation from van der Waal interactions. This decrease in sorptivity with temperature is indicated in the later part of the Cs BTC in Figure 29 that shows an increase in the Cs concentration above the exponentially predicted amount after the column temperature was raised above 120°C.

Table 2: Alkali metal salt retardation by column filled with calcite, albite, and quartz particles between 450 - 500 μm.

	Li 9/12		Li 9/24		Cs 9/26		Cs 10/8	
	Mean	CV	Mean	CV	Mean	CV	Mean	CV
Average of inlet & outlet temperatures over course of experiment (C)	120.15	1.97%	119.82	1.30%	119.41	0.85%	120.04	1.47%
Average flow rate (g min^{-1})	2.06	0.47%	2.05	na	2.063	na	2.08	2.02%
Pulse mass (g)	297		272		82.5		260	
Vp, MoM (ml)	116	2.57%	113	5.53%	129	na	113	3.49%
Rf, MoM	1.39	na	1.54	na	2.59	na	5.89	na
Rf, ADE	1.19	na	1.19	na	1.85	na	4.87	na
Rf, NADE	3.19	na	2.02	na	6.33	na	5.46	na
v, average pore water velocity (cm min^{-1})	0.88	8.98%	0.87	5.40%	0.88	na	0.88	2.73%
D, dispersion coeffcient (cm2)	0.19	42.58%	0.19	31.04%	0.18	na	0.22	36.84%
β, fraction of equilibrium sites	0.36	na	0.55	na	0.33	na	0.73	na
ω, 1^{st} order rate coefficient (cm min^{-1})	0.013	na	0.012	na	0.040	na	0.037	na
	pH	EC (μS)	pH	EC (μS)	pH	EC (μS)	pH	EC (μS)
Equilibration & flush solution	8.0	136	8.0	189	8.1	199	8.3	123
Tracer solution	8.1	287	8.1	285	8.2	368	8.1	335
Pre-pulse eflluent	9.4	209	8.2	212	8.2	237	8.3	219
Post-pulse effluent	8.8	242	8.6	230	8.8	226	8.7	262
EC stands for electrical conductivity and CV for coefficient of variation.								

There is some indication that the injection backflow transport modeling may use CEC instead of the volumetric based retardation factor. Consideration of how to provide this value for site specific conditions led to the realization that the difference between the conservative and reactive tracer's step injection BTCs provides the amount of reactive tracer retained by the geomedium. These experiments didn't provide step injections so estimated parameters were used to extrapolate with the NADE out to Heaviside inputs (Figure 32) to provide preliminary CEC values from the difference between the mass recovery rates of the two tracers. Preliminary calculation of CEC from the Cs curve has begun, but work will continue this quarter to evaluate the effectiveness of this approach to potentially provide these values.

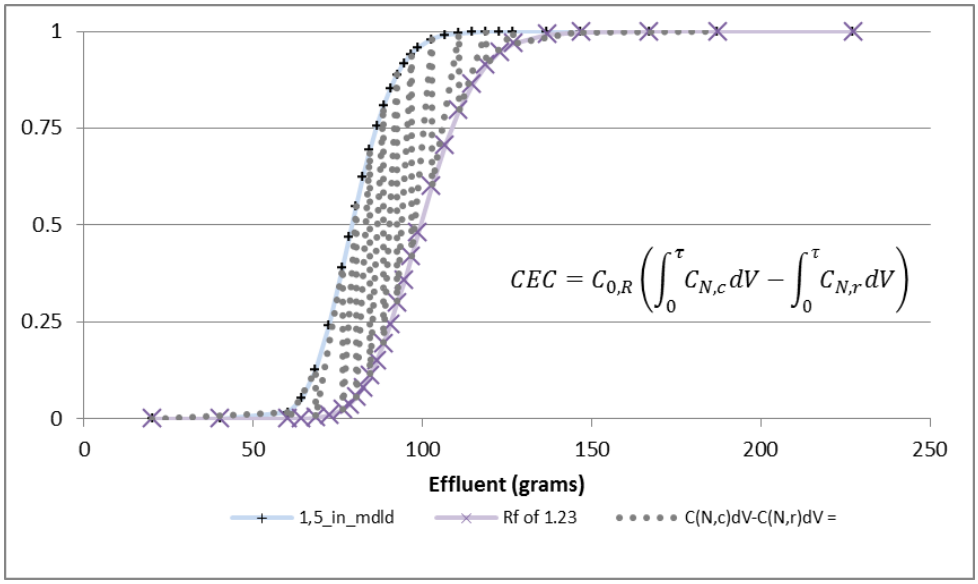

Figure 32: Prospective method to determine CEC for a reactive tracer from Heaviside injection curves of a conservative and reactive tracer's BTCs. $C_{0,r}$ is the reactive tracer concentration, $C_{N,r}$ is the normalized concentration of reactive tracer, $C_{N,c}$ is the normalized concentration of conservative, and τ is the total volume that both curves are integrated under.

Table 3: Values and coefficients of variation determined from different methods. The initial estimate of CEC_{Cs} from this technique appears to be orders of magnitude too large compared with that reported by Akiba and Hashimoto, 1989 and the theory and technique will require additional effort.

	Li mean	CV	Cs mean	CV
Kd, MoM (l kg-1), quartz only	0.015	68.17%		
Kd, MoM (l kg-1), trimix461	0.077	20.50%	0.552	65.01%
Kd, ADE (l kg-1)	0.032	3.52%	0.398	84.89%
Kd, NADE (l kg-1)	0.268	53.63%	0.866	21.56%
CEC, NADE (meq g-1)	nd	na	0.1051	na

Task 4.2: Purchase Tracers (Conservative and Adsorbing) and Initiate Interwell Tracer Test

First Quarter

Task complete.

Task 4.3: Collect and Analyze Samples

First Quarter

Task complete.

Task 4.4: Invert the Tracer Data to Determine the Fracture Surface Area Between the Injection and Production Well Pair

First Quarter

Mark Williams (PNNL):

Numerical models are being developed using the ToughReact code for interpretation of the two-well tracer test conducted in September 2011 at the Soda Lake site and for investigation of the efficacy of using single-well injection/withdrawal tests at the site for fractured reservoir characterization. Site characterization and tracer parameters from fitting the two-well tracer test data are used for the single-well injection-withdrawal test models. The ToughReact code was selected to take advantage of the MINC option for simulating a fractured reservoir and options for simulating sorbing and thermally decay of tracers.

Current efforts have involved developing a preliminary two-dimensional model (constant thickness) for fitting the September 2011 Soda Lake tracer test with conservative (1,6 NDS) and reactive (Safranin-T, sorption with thermal decay) tracers. A slightly different two-dimensional plan-view model has also been developed for simulating single-well injection-withdrawal tests at the site along with a one-dimensional, radially symmetric model, which is more computationally efficient and provides similar results. Results of these preliminary models are provided in the 2012 Stanford Geothermal Workshop paper ("Use of Tracers to Interrogate Fracture Surface Area in Single-Well Tracer Tests in EGS Systems," Paul REIMUS, Mark WILLIAMS, Vince VERMEUL, Peter ROSE, Kevin LEECASTER, Bridget AYLING, Raphael SANJUAN, Morgan AMES, Cynthia DEAN, and Dick BENOIT").

Continuing efforts include updating numerical models based on laboratory measurements of Safranin T sorption with Soda Lake site materials and at reservoir conditions. This will help constrain estimates of fracture volumes / areas from fitting of the September 2011 two-well tracer test data. Additional site characterization information will be evaluated for inclusion in the site-specific model. Sensitivity studies will be run to investigate the impact of fracture spacing and volumes on test responses for evaluation of parameter uncertainty. This range of parameters will then be used to run a suite of single-well injection-withdrawal simulations for different operational scenarios to help design field tests where the field results would be useful for determining fracture spacing/area at a specific site. A preliminary example of the responses of a single-well injection-withdrawal test for two operational conditions (one hour tracer pulse vs. continuous tracer injection for three days) using the current fitting of site parameters from the two-well tracer test data is shown below (Figure 33).

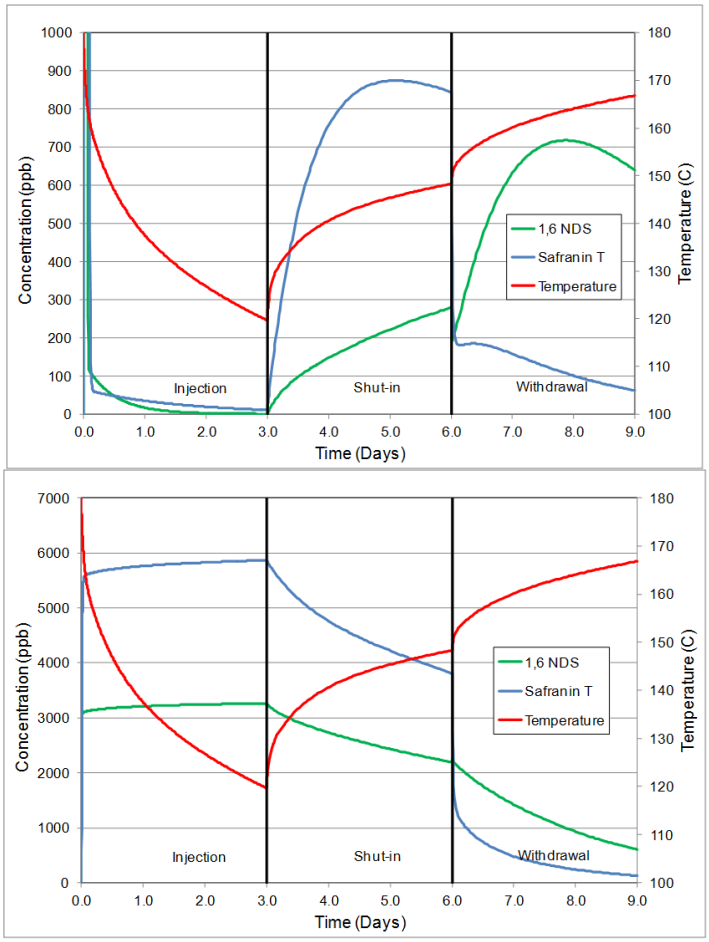

Figure 33. Single-Well Injection-Withdrawal Simulation. (a) 1 hour tracer pulse followed by fresh water during injection stage (b) constant tracer concentration during injection stage (same mass as a). Simulated concentrations and temperature in injection/withdrawal well.
Second Quarter

Mark Williams, PNNL

Work is continuing on developing a site-specific ToughReact model for simulating / fitting the results of the Soda Lake tracer test conducted in the fall of 2011. The model is a two-dimensional plan view grid (constant thickness of 300m) that has 10-m grid spacing between and around the injection and production wells with increased grid spacing to a far-field boundary. The MINC option selected is the dual porosity option and subdivided into 5 interacting continua (1 for the fracture and 4 for the matrix). The wells are spaced 550 m apart. We used ½ symmetry (see Figure 34) for the problem with corresponding reductions in injection and withdrawal rates (full values were 800 gpm injection and 885 gpm production) and tracer mass.

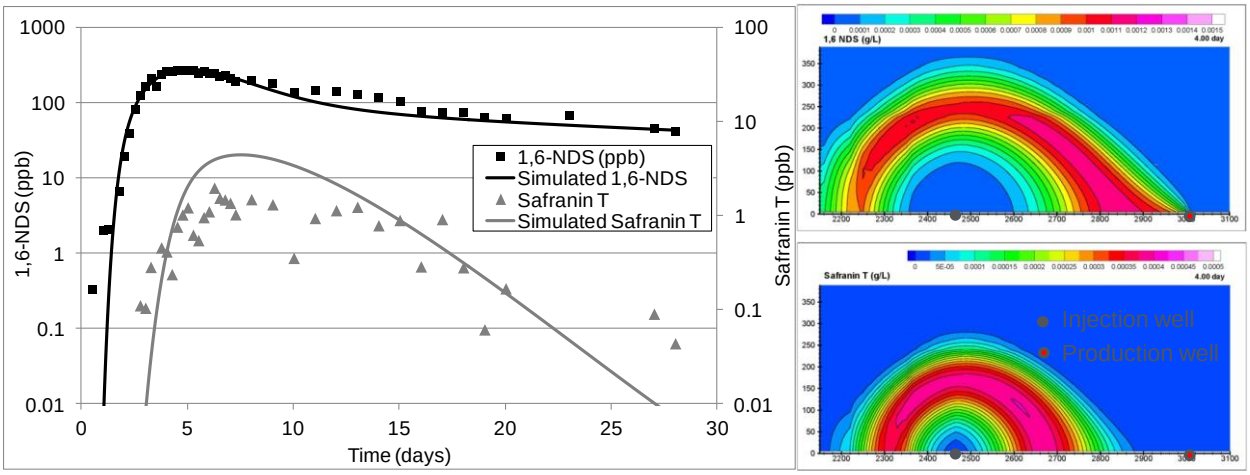

Figure 34. Preliminary results of two dimensional (x,y) ToughReact simulation of Soda Lake Tracer Test (conducted in fall of 2011) showing (a) comparison of simulated and measured production well tracer concentrations and (b) tracer concentrations (1/2 y-plane symmetry) at T=4 days. Note that thermal decay and sorption are simulated for Safranin T so measured results are shown for direct comparison with simulated values.

The simulation includes a conservative tracer (for 1,6-nds) and a reactive tracer (Safranin T) pulse injection followed by continuous injection of water (at 71^{o}C) and withdrawal from the production well. Current assumptions / limitations of this numerical model include tracers injected only during an initial 1-hr pulse (Safranin T injection took longer due to injection difficulties), tracer recovered from the production well is not recycled back into the system, and the initial temperature distribution in the reservoir is set to 180^{o}C. Safranin T is simulated as a sorbing and thermally decaying tracer. Arrhenius parameters for the thermal decay of Safranin-T were set based on bench-scale measurements.

A manual calibration process was used for this initial model. Parameters were varied based on visual comparison of simulated results with the tracer concentration measurements from the production well. The parameters varied during this fitting process included fracture and matrix volumes, matrix porosity, matrix diffusion coefficient, and Saf T partition coefficients (different values for fractures and matrix). An initial fracture spacing of 10 m was used but was not varied. The current fit is of the preliminary model is shown in Figure 34 which has generally good agreement between the measured and simulated tracer concentrations. The biggest discrepancy apparent in Figure 34 is with the Safranin T concentrations after ~20 days. Work is continuing on parameter fitting and sensitivity of fracture area and fracture volume on the simulated breakthrough curves. Additional work is planned for comparison of the parameters determined from the ToughReact modeling with the RELAP modeling results. Lastly, incorporating ongoing results of bench-scale testing of Safranin-T sorption with reservoir and fracture minerals (or surrogates) would help to constrain the field-scale tracer test numerical modeling for estimating fracture surface area / volume (current modeling has both Kds and fracture area/volume as fitting parameters).

Paul Reimus, LANL:

Bounding estimates of surface area to volume ratios from the Soda Lake sorbing tracer test

A detailed analysis of the Soda Lake sorbing tracer test was conducted to obtain bounding estimates of surface area to volume ratios in the geothermal flow system based on differences between the breakthrough curves of 1,6-Naphthalene Disulfonate (nonsorbing) and Safranin T (sorbing). The biggest assumptions in the analysis were that the volcanic tuff at Soda Lake had specific surface areas comparable to specific surface areas of tuffs at Yucca Mountain, NV and that the surface-area-based partition coefficients estimated for Safranin T in sand-packed column experiments at EGI also applied to the Soda Lake tuffs. Other parameters in the analysis (e.g., matrix porosity of the tuffs, matrix diffusion coefficients) were uncertain, but they were varied systematically over reasonable ranges to evaluate sensitivity of surface area estimates to these parameters. The analysis was ultimately not highly sensitive to the thermal decay rate of the Safranin T, although this was accounted for using thermal decay data generated at EGI.

It was concluded that the conceptual model most consistent with the observed tracer breakthrough curves was a "rim-zone" model in which a thin porous layer on the fracture surfaces provides the surface area for sorption of the Safranin-T (see Figure 35). With this model, a significant delay in the first arrival of a sorbing tracer relative to a nonsorbing tracer (as observed in the tracer test) can be simulated without invoking unrealistically large fracture surface area to volume ratios (or alternatively, unrealistically small fracture apertures).

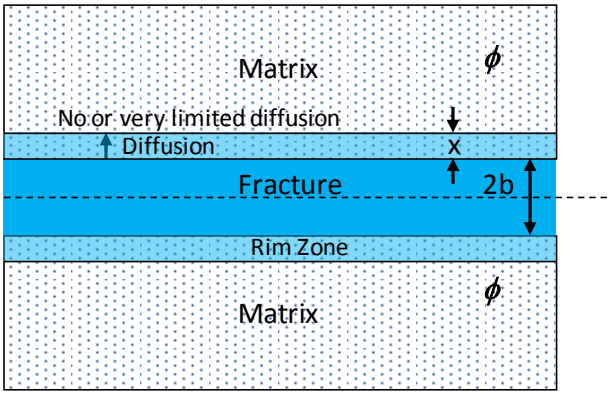

Figure 35. Schematic of the rim-zone model.

Figure 36 shows examples of model fits to both the 1,6-Naphthalene Disulfonate and Safranin T breakthrough curves assuming different conceptual models (either single-porosity or dual-porosity). This figure illustrates the nonuniqueness of the test interpretations; note that the rim-zone model most closely matches the single-porosity model in this figure.

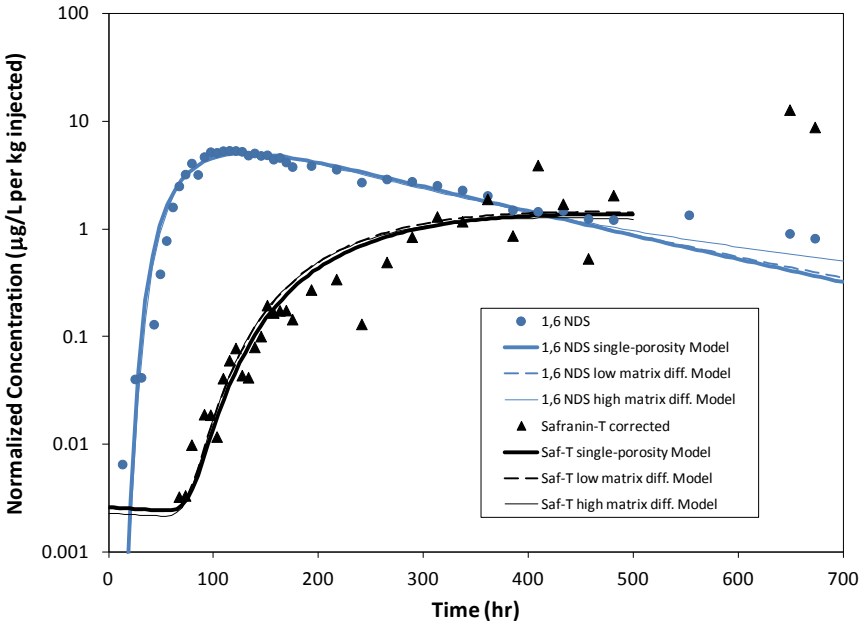

Figure 36. Single- and dual-porosity model fits to the 1,6-nds and decay-corrected Safranin T breakthrough curves. Note that the last three Safranin-T data points (beyond 500 hrs, including one covered by the legend) were not fitted because these points are highly uncertain due to thermal decay of the tracer.

Table 2 gives the best-fitting rim-zone model parameters as a function of assumed rim zone porosity (first column), with the final column being an estimate of the maximum average fracture half-aperture in the flow system that is consistent with the data. The fracture half-aperture estimate is equivalent to an estimate of the volume-to-surface-area ratio in the flow system (that is, the reciprocal of the surface-area-to-volume ratio). The values of Table 2 were obtained assuming a specific surface area of the Soda Lake tuff equal to a mid-range value (35,000 cm^2/g) for Yucca Mountain tuffs.

The above analysis method provides only an upper-bound estimate of the maximum fracture half-aperture (minimum value of surface-area-to-volume ratio); any value smaller than this will also provide a good fit to the data. To obtain a lower-bound estimate of fracture half-apertures, hydraulic resistance calculations were conducted to determine the smallest apertures that are still consistent with the observed head difference between the injection and production wells during the tracer test. These calculations resulted in lower-bound fracture half-aperture estimates of 0.0025 to 0.004 cm; i.e., roughly an order-of-magnitude lower than the half-aperture estimates of Table 2.

Table 2. Rim zone model parameters, including upper bound estimates of fracture half apertures (b_{max}), yielding good fits to the Soda Lake Safranin T breakthrough curve assuming a tuff specific surface area in the rim zone of 35,000 cm^2/g.

ϕ_{rim}	D_m, cm^2/s	τ, hr	*Pe*	*mass frac*	R_{rim}	*x/b*	b_{max}, cm
0.1	1e-6	229	3.9	0.2725	21.4	1.46	0.024
0.15	1.4e-6	206	4	0.2675	13.9	1.69	0.03
0.2	2e-6	184	4	0.2675	10.1	2.01	0.0375
0.3	4e-6	132	4	0.27	6.30	3.21	0.0375
0.4	8e-6	61	4	0.2675	4.41	8.07	0.024

ϕ_{rim} = assumed rim zone porosity
D_m = assumed tracer diffusion coefficient in the rim zone
τ = mean nonsorbing tracer residence time
Pe = Peclet number = distance between wells divided by longitudinal dispersivity
mass frac = mass fraction of tracers deduced to be participating in the tracer test
R_{rim} = calculated Safranin-T retardation factor in the rim zone (based on porosity, assumed specific surface area and surface-area-based partition coefficient of Safranin-T
x/b = thickness of rim zone (x) divided by fracture half aperture (b)
b_{max} = maximum (upper-bound) estimate of fracture half aperture

Fourth Quarter

Mark Williams

Work was started in the fourth quarter on developing a numerical model for the planned reactive tracer testing in support of the Newberry EGS demonstration being conducted by AltaRock Energy Inc. The objective of this tracer testing is to help estimate the fracture surface area and fracture volume created by the stimulation. Up to 3 stimulation zones could be created during the EGS demonstration with tracer injections planned following each stimulation event (but before the diverters used for the first and second stimulation). A backflow test is planned after all stimulation activities have been completed and when sufficient time has elapsed for the diverters to degrade. Three different conservative tracers are planned (1,6-NDS, 2,6-NDS, and 1,5-NDS), one for each stimulation zone, along with two sorbing cation tracers (Li^+ and Cs^+) to be used for two of the stimulation zones. Rates and durations were estimated based on discussions with AltaRock and the project team. The table below shows the nominal design used in these initial preliminary scoping simulations.

The ToughReact (version 2.0) code was selected for developing these numerical simulations. Efforts during this period have been focused on setting up the grid and the pre/post processing for the different run stages (e.g. stimulation water injections, tracer injections, diverter injections, and final backflow) which require separate runs for each stage using results from an earlier stage for initial conditions. While the permeability changes created during the stimulations and diverter are not being simulated, the water injections used for these operations are focused into

different permeable vertical layers. An eight-layer, radially-symmetric grid was developed. The layering/potential stimulation zones and initial temperature gradients were based on planning documents provided by AltaRock. Sorbing tracers are initially being simulated with a linear K_d using non-site specific values for Li^+ and Cs^+. These parameters can be updated when site-specific values are determined from laboratory experiments for these cations and site mineralogy.

Future simulations will also use the ToughReact capability for simulating cation exchange reactions for the reactive tracers. Preliminary scoping numerical simulations planned with this model will look at the range of potential conservative and reactive tracer concentrations in the backflow sample stream and cumulative mass recovery with different fracture surface area and volumes. The simulations will also enable investigation of potential benefits in modifying the tracer test operations (e.g. use higher sorbing tracers during the first or last stimulation).

Nominal Test Design for Preliminary Modeling

	Start (day)	Flow Rate	Tracers	Duration
Cycle 1				
Stimulation 1	0	800 gpm	None	7 days (~8M gal)
Tracer 1	7.0	800 gpm	Conservative Tracer = 20 mg/L 1,5-nds (also Cl^- from sorbing tracer ~ 100 mg/L) Sorbing Tracer = 20 mg/L Li^+ (0.5 mL/g Kd)	6 hrs (288K gal)
Diverter 1	7.25	300 gpm	None	6 hrs
Wait 1	7.5	None		12 hrs
Cycle 2				
Stimulation 2	8	800 gpm	None	7 days (~8M gal)
Tracer 2	15.0	800 gpm	Conservative Tracer = 20 mg/L 1,6-nds Sorbing = none	6 hrs (288K gal)
Diverter 2	15.25	300 gpm	None	6 hrs
Wait 2	15.5	None		12 hrs
Cycle 3				
Stimulation 3	16	800 gpm	None	7 days (~8M gal)
Tracer 3	23.0	800 gpm	Conservative Tracer = 20 mg/L 2,6-nds (also Br^- from sorbing tracer ~14 mg/L) Sorbing Tracer = 20 mg/L Cs^+ (5 mL/g Kd)	6 hrs (288K gal)
No Diverter 3	----	-----		---
Wait 3	23.25	None		18 hrs
Backflow	24	800 gpm		5.2 days (~6M gal)

Task 4.5: Re-deploy the Field Fluorimeter to Demonstrate Both Fracture Activation and Downhole Measurements of Flow Rate

Background

The original design of the field fluorimeter was analyzed and considered to be too risky to pursue. It was to consist of a spectrometer (complete with fiber optics, a CCD camera and a laser light source) located at the surface near the wellhead. One of the problems identified with the design, however, was the need to mount the spectrometer on the coiled-tubing drum that will be used to deploy the fiber optic cable. The optical fiber would be deployed within the coiled tubing in order to protect it from the harsh environment within the wellbore. However, there are many problems associated with deploying 10,000 ft of optical fiber—even if that fiber is enclosed within capillary tubing. Not only is the fiber quite expensive to deploy in this fashion, any break in the fragile fiber would of course render the tool inoperable. Given these risks, an alternative design was developed that will allow for the deployment of the spectrometer downhole on a wireline, thus avoiding the problems associated with deploying optical fiber over long distances within EGS wellbores. The drawback of this approach is that the tool will now have to be designed and fabricated in such a fashion that it can be deployed downhole and through a lubricator, limiting the diameter of the tool to about 2.6 inches. As described below, excellent progress is being made towards the design and fabrication of the tool.

Current Design

A cartoon sketch of the tool design is shown below as Figure 37 including the optical fiber bundle that will serve as excitation light delivery and emission light collection.

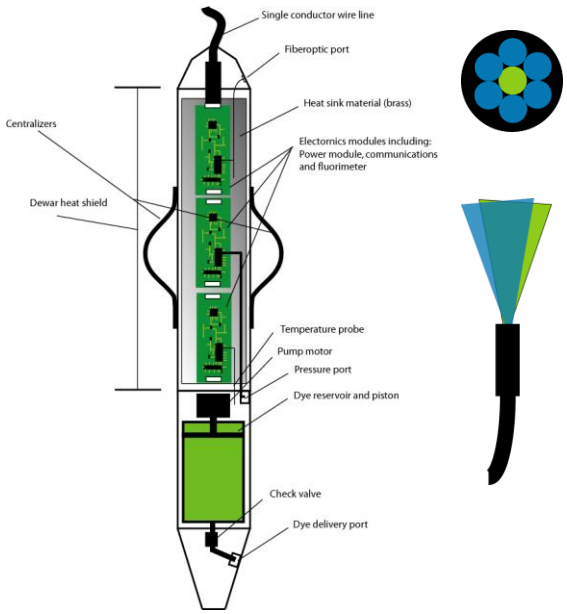

Figure 37. Cartoon sketch of purposed tool and fiber optic bundle.

A simple laboratory prototype of the tool was completed during FY2011 (see annual report for FY2011). A second generation version is being fabricated in anticipation of the design and fabrication of the flasked, field-hardened tool.

First Quarter

Work has continued on the electronics to capture emitted light and the electronics to communicate with the surface. A test fixture was made and water reservoirs have been procured for use as soon as the prototype electronics are finished. The test tool will be larger in diameter than the final product but should give a good indication of any changes that may need to be made in the final version.

Work has also continued on a dye delivery pump. The two sketches below give an indication of what the pump will look like. Figure 38 gives the basic dimensions and overall length in inches of the pump.

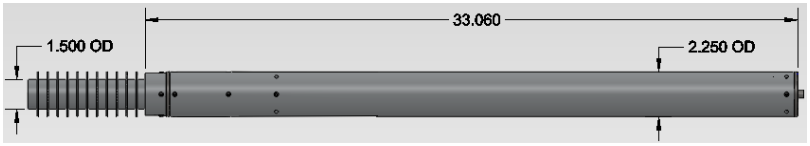

Figure 38. Sketch of pump.

The pump will attach to the end of the flasked tool. The high temperature motor and pump hardware are designed for use at temperatures in excess of 300° C. The pump consists of 4 piston/cylinder chambers which can deliver a metered dye flow at reservoir pressures. A close up look at the motor and pump chamber interface is seen in Figure 39.

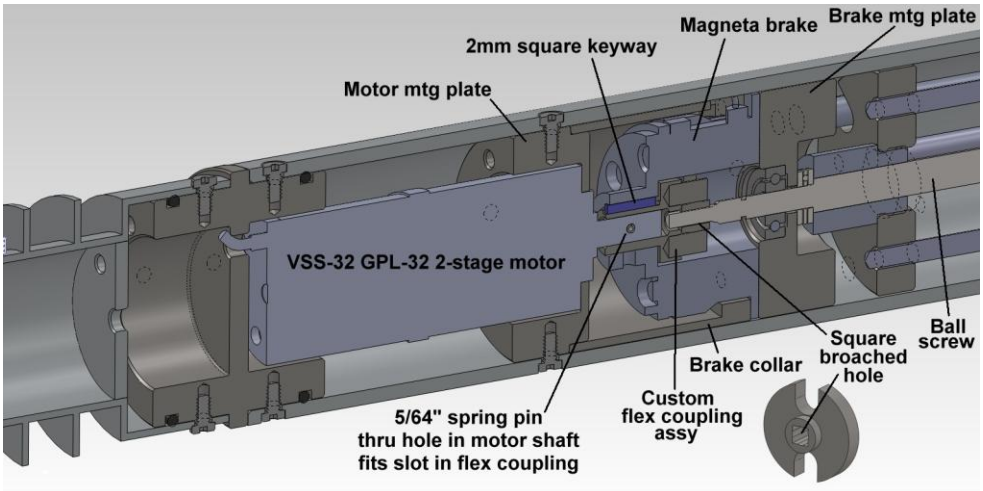

Figure 39. Close-up view of motor and pump interface.

For the prototype a cooler motor can be installed at a much lower cost. Once the concept is proven the high temperature motor can be installed and used without need for much change.

Second Quarter

Mike Mella, EGI:

This quarter a detector and improved light source were completed. Both of these new components have been tested in the lab. The light source appears to be more than bright enough for our purposes. The thermal output of the LED looks like it will be acceptable even at 100% duty cycle and intensity. The test detector produced uses a photodiode and does not look like it will be sensitive enough. Work on a photo multiplier tube detector will continue as this looks like it will be necessary for future work.

Bruce Boyes, Systronix:

Our off-the-shelf Arduino-based development is proving a good choice since we only need to design and build the more esoteric modules. The second revision of the LED modulator (with a monitor diode at the source) is now working as expected. Also the second revision of a photodiode fluorescent detector is working well enough that there's hope that it could be used instead of a PMT at less than 1/10 the cost and volume, with lower power consumption and no high-temperature rapid deterioration.

Wireline telemetry circuitry might be available through partnership with Admyr Wireline or a company in the Netherlands. This has to be considered with the power supply since both of these circuits share the wireline and must coexist peacefully. Getting power and data over 18,000 feet of single-conductor wireline is a challenge and there are no current open standards or open-source designs we can leverage.

Eliminating the pump in the first implementation of the borehole fluorimeter is a huge simplification of the power supply and control electronics.

The second revision of the LED modulator and the solid-state photo-diode detector are up and working and installed at the EGI lab. We are ready to gather data with test samples and proceed with higher-gain stages for the detector.

So far, the performance of the LED modulator continues to exceed specifications, and we have working temperature- and light- based feedback stabilization circuits, which will be essential to maintain performance over the full range of well temperatures. The solid-state photodetector is working well enough to justify continuing along that path and add better analog signal conditioning and amplification to it.

Detail

PMT Electronics.
This has been set aside a bit due to the focus on a much more promising solid-state photodiode detector. See that item for details.

LED Modulator Rev 2.

This design so far has exceeded expectations. Michael Mella reports that it is much better for our task than the much more expensive Ocean Optics LED source. Firmware to use all feedback paths is complete. Rise and fall time are less than 10 usec with no over- or under-shoot. This means that we can pulse the LED fast enough for our purposes. Currently the code uses a granularity of 1 millisecond which is more than adequate for our task. This means we can have a pulse of a few milliseconds at a period of say one second or less, and the duty cycle and power use will be low, but we will still get a big "blast" of light to stimulate the tracer. The LED monitor feedback circuit is working properly, and the Arduino bug has been fixed.

Photodiode Fluorescence Monitor
This is a larger-area photo-diode which might replace the PMT, at least in the lab, and possibly in the borehole. A single blue-sensitive second revision is up and working with a quick and low-cost transimpedance amp using National generic opamps LM7715. This is working well enough that it appears possible that it could have enough sensitivity for use instead of a PMT. But this is a very preliminary anecdotal test. This month we will quantify its performance with the new optical power meter.

There are much better transimpedance amplifier components available, still at a tiny fraction of the price of a PMT. We have added these parts to our electronic CAD package and are ready to move ahead with this.

If we can pull this solid-state photodector design off, it would be a huge win. It would be less than 1/10 the cost and size of a PMT, with none of the high temperature deterioration of the PMT, and no need for a 1500 volt bias supply. The solid-state PD is so small and inexpensive that we could imagine using several in a single fluorimeter, to support multiple wavelengths. This would be impractical with a PMT.

Analog path research
We may end up using a Cypress PSoC device as the analog gain stage for the solid-state PD or the PMT, prior to analog-to-digital conversion. The Cypress analog PSoCs are like analog Legos and would give us programmable configurability in the field as a gain and filtering block. Devices are available up to 125^{o}C. We can also use a high-resolution analog to digital converter with a precision programmable gain amplifier instead of, or in addition to, the PSoC-based front end. All parts under consideration are available at 125^{o}C.

High Temperature (125^{o}C) Components
At the Embedded Systems Conference I received confirmation that we can use Xmega at 105^{o}C and most likely at 125^{o}C.

Solid-State Gamma Detector
It recently came to my attention that it is possible to build a gamma detector with a solid state photodiode as the scintillometer instead of a fragile glass Geiger-Muller tube. Amazingly, the preferred diodes are blue-sensitive types such as we are already using in the LED monitor and sold-state photodetector! It appears possible to put together a prototype using low-cost off-the-shelf components such as Arduino and an Earth LCD touch screen.

Probe power supply and telemetry interface
We have a first pass at a power supply design which will accept up to 400V on the wireline and regulate it down to 48V or less, and can handle over 100 watts. If there is no pump in the first fluorimeter, this means we can regulate down to 12 volts as a bus, and don't need to start with 400V at the well head. This no-pump option greatly simplifies our power supply design (but of course when we add the pump we will need a new power supply design to support it). Recently I have been working on the related topic of the telemetry link, since the power supply is an integral part of that design: the wireline has to support both power and data transmission simultaneously. So it has to be a wholistic design approach.

Wireline telemetry link:
Designing the telemetry interface to the wireline is another big task which remains to be done, and this becomes part of the main wireline power supply board, since the telemetry needs to couple in on the 400V side of the supply. We got a lot of useful information from Rochester Wireline. I have also started some detailed discussions with Admyr Wireline, and their engineer in Columbia.

Pump design:
We made some significant progress on the architecture of the pump brake. This whole topic has been set aside for the first implementation of the fluorimeter, which greatly simplifies many aspects of the electronics and mechanics.

Embedded Systems Conference in San Jose March 27-28
I attended a DOE LED lighting talk which was quite fascinating and has some bearing on our work. I met with some LED vendors and have some contacts and information. The Luxeon Rebel series we are using now as our stimulation source is still a good choice. I met with technical people from Atmel and other companies and came away with some fresh information and contacts. I met with LCD touch panel people from EarthLCD and came away with a demo loaner. This could be useful in the lab and possibly in the final system.

Third Quarter

Mike Mella, EGI:

This quarter most of the work was intended to improve the optical path for the system. Several improvements were made including better filters and collimators. Tests made using a full spectrum desktop spectrometer showing that too many different wavelengths were making it through the optical path. Any detector that will be incorporated in this device, whether it is a photodiode or a photomultiplier tube, will not be able to distinguish wavelengths and will only be an indication of light intensity. If there is too much light from the excitation wavelength allowed to reach the detector, we would get a false signal or one that is so high that it would completely overwhelm any fluorescence emissions. With an improved optical path the hope is that a better design for the photodiode detector can be made. Once this detector is finished then lab tests can be conducted using the wellbore simulator we have constructed in previous quarters.

Bruce Boyes, Systronix:

This quarter work focused on improving the analog signal path, particularly the solid-state fluorescence detector, and on the design of the optical path, particularly the fiber optic to beam interfaces and optical filtering. Significant progress has been made in both areas.

Solid-State Photodetector

All transimpedance amplifiers (these convert the current output of a photo-diode to a voltage) have been converted to use the much better Analog Devices AD8605/6 series opamps . This includes the photodetector and also the LED monitor circuit. These have better than an order-of-magnitude improvement in terms of voltage and current noise and offset voltage.

High-resolution ADC with PGA

Our original choice for the analog-to-digital converter (ADC), which also includes a programmable-gain amplifier (PGA) was causing problems due to a development board software incompatibility. We studied ADC data sheets and then contacted the manufacturer (Analog Devices) who confirmed that we could change to a similar member of the family, and use the AD7193 evaluation board. We did so and were able to extract what seemed to be a fluorescence signal from a Fluorescein sample (see Figure 40).

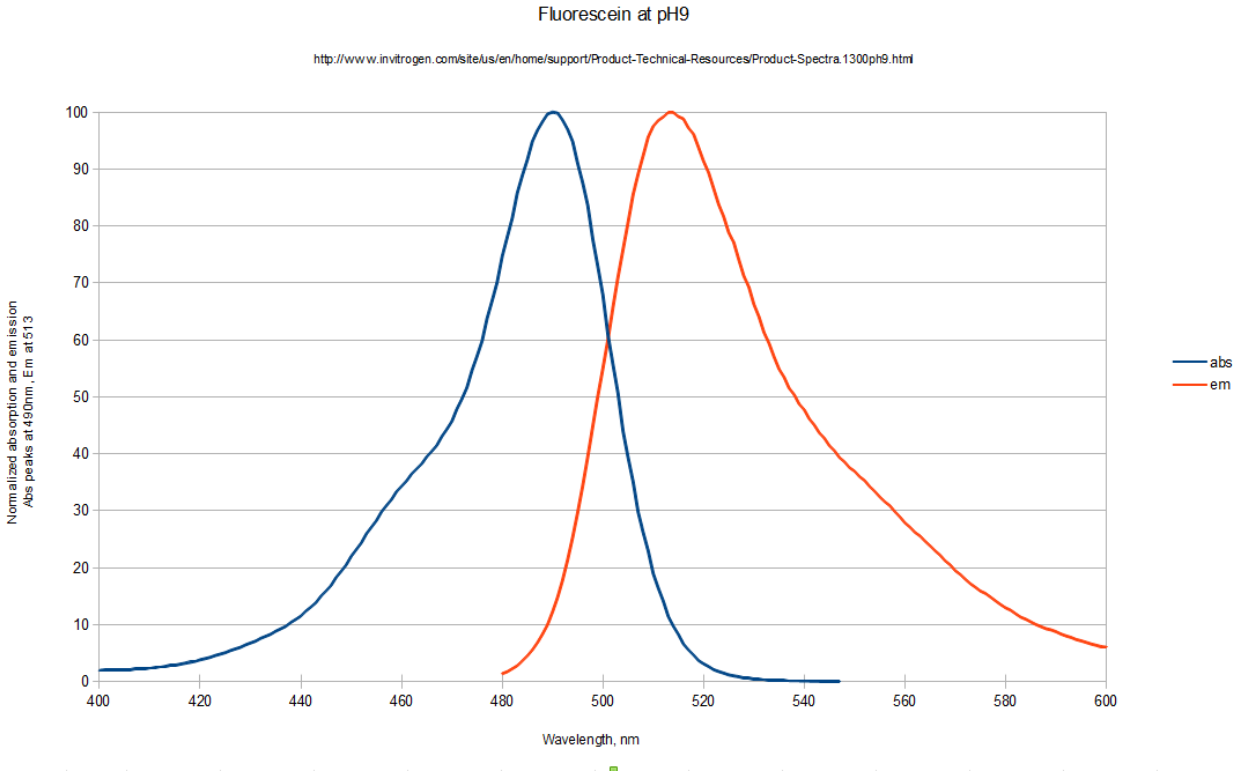

Figure 40. Fluorescein absorption and emission in a medium with pH of 9

Optical Path and Wavelength Isolation

However further testing raised the suspicion that what we were seeing (at least in part) was excitation wavelength in the emission path. Our optical path uses filters to isolate the excitation and emission wavelengths of fluorescein, so something was clearly amiss.

Here is the manufacturer-provided filter data in the only form available on their product website: a linear scale.

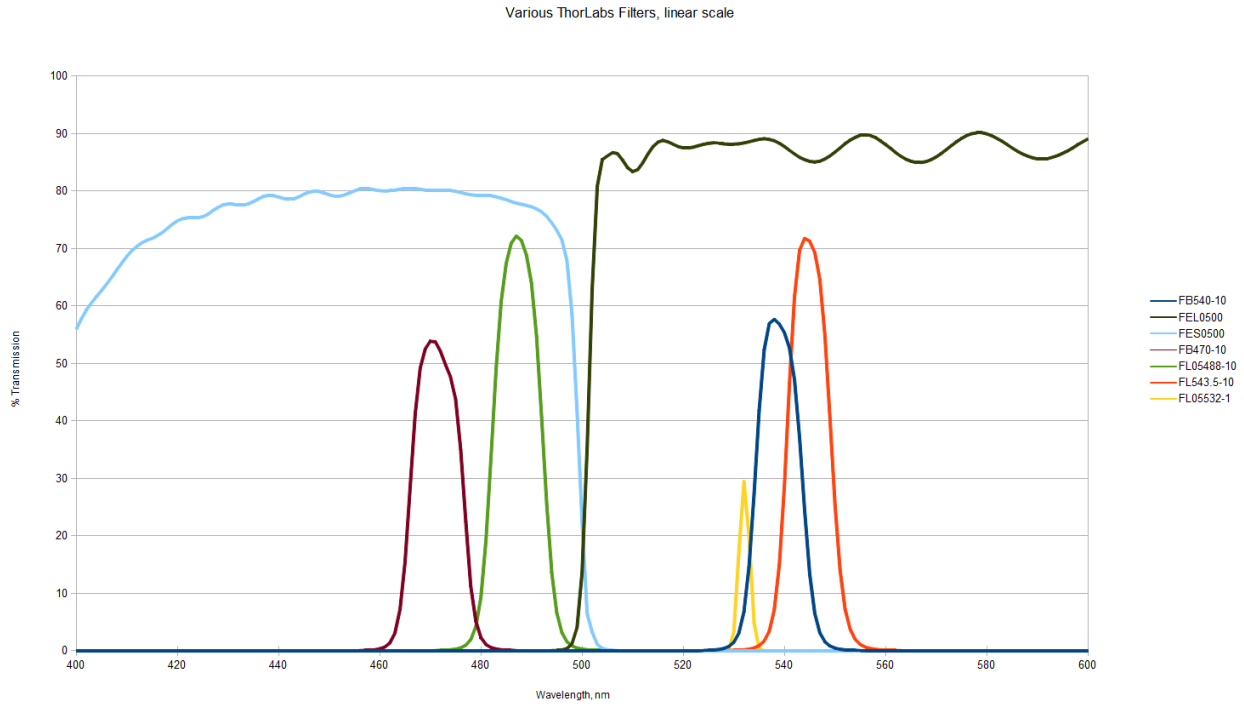

Figure 41. Thorlabs filters, Thorlabs data files, linear scale

We were using the FL05488-10 blue bandpass filter on the LED (green data), and the FL05532-1 green bandpass (yellow data) on the emission return path. These curves look almost ideal (except for peak transmission being less than 100%). However this linear transmission scale only encompasses about two orders of magnitude. Our photo-diode detectors can accommodate a range from tens of milliwatts to tens of picowatts, nearly six orders of magnitude.

It turns out that Thorlabs publishes the raw data files for all their filters. This data is not especially easy to find, and not all their application engineers (in particular the two who spoke with me) even know that it exists. We downloaded this data and plotted it with a logarithmic transmission (Y-axis) scale. The same filters above look much less ideal when more of their dynamic range is viewed.

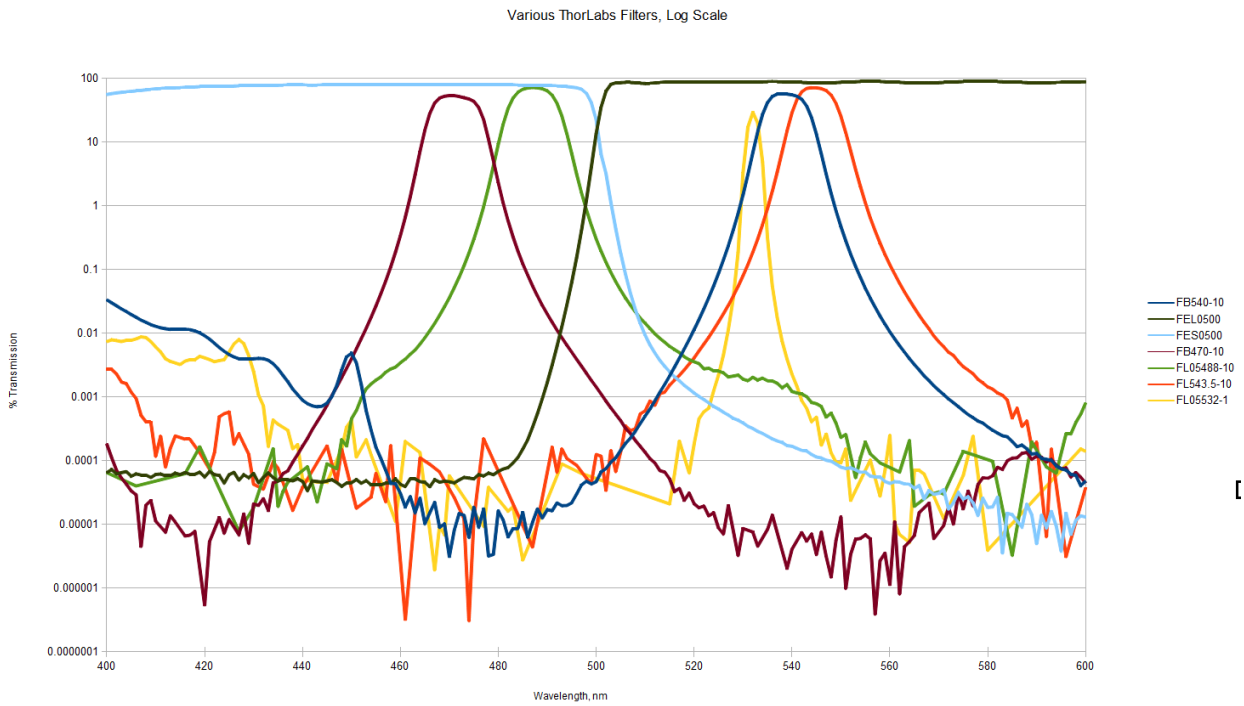

Figure 42. Thorlabs filters, same data files as linear plot, but with logarithmic scale on Y-axis

The filters we chose (olive green and yellow plots) cross over at a bit better than 1%, which means a blue-green wavelength will not be sufficiently extinguished. This could explain why we see our LED excitation in the emission path. Also you can see that the maroon 470 nm bandpass is about two orders of magnitude better.

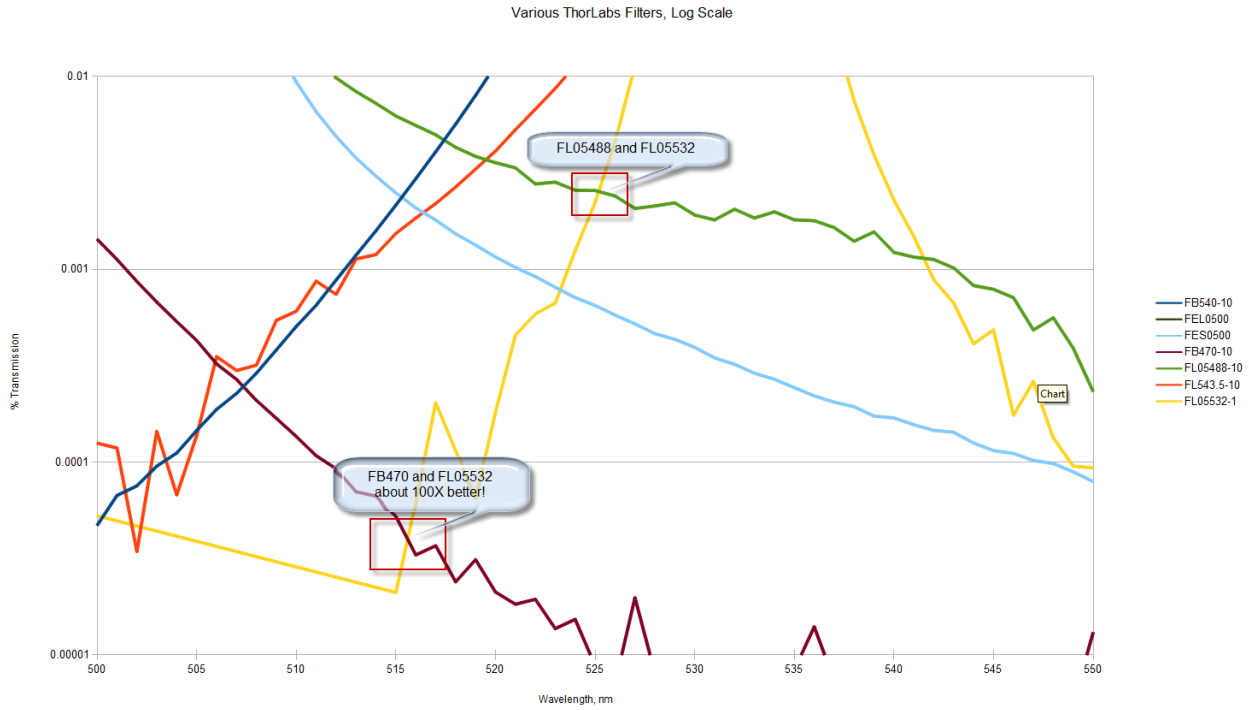

Figure 43. Logarithmic filter plot, zoomed in to show the two sets we used

We confirmed this theory with an Ocean Optics USB2000 spectrometer. We also confirmed that using the FB470-10 filter removed the excitation blue from the emission green optical path. This test also let us see the 940 nm Raman emission of water, which we need to be sure is filtered out; it is with the 532 nm bandpass but would not be removed with a single longpass filter.

However, our 532 nm bandpass filter is too selective, and we give up too much of the Fluorescein emission, which is partially to blame for our low fluorescence signal. We are currently working to preserve much more of that signal with improved optical filtering and improved sample chamber optics.

Fiber Optic Coupling Efficiency Improvement

Another significant improvement this quarter was applying the new Thorlabs pre-aligned collimation lenses such as F671SMA-405 for the blue excitation path and F240SMA-A for the green fluorescence path. These are much more effective than our first attempt at aligning unmounted optics in lens tubes.

Current Results

We can now detect a delta of 50 picowatts from a 10ppm aqueous fluorescein solution, excited with 90 microwatts from a lens-less Mella Y-fiber (excitation core is 600 um, surrounded by six 200 um fibers to collect the emission signal. The USB2000 spectrometer can sample this 532 nm signal to a value of 3000 counts with an integration time of 400 msec.

Fourth Quarter:

Mike Mella, EGI:

This quarter significant work has been made on both the optics and mechanical parts of the tool prototype--mechanical pieces that will hold the circuit boards, lens tubes, photo diode and LED boards. A plastic tube with the same exterior dimensions as the interior of the heat shield was obtained and a tray to hold all the components was machined. Figure 44 shows some components on the metal tray that will hold the components inside the heat shield.

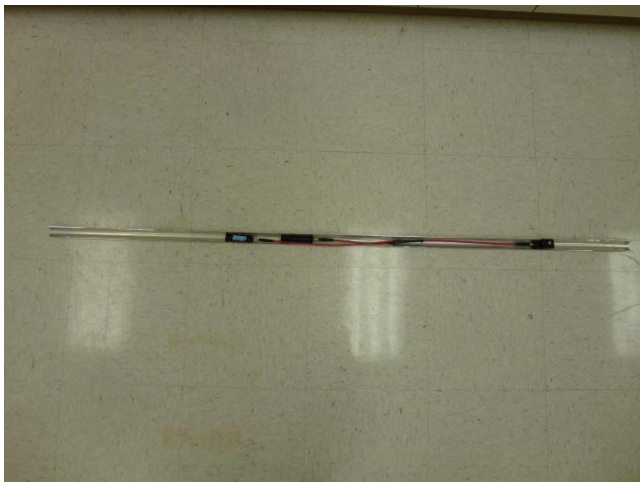

Figure 44. A few components in the metal tray.

The entire apparatus slides inside the plastic tube as pictured in Figure 45. The bottom is closed and the top is open to allow wires to exit at the top. The rest of the tube will be water tight and can be tested in our lab flow tester.

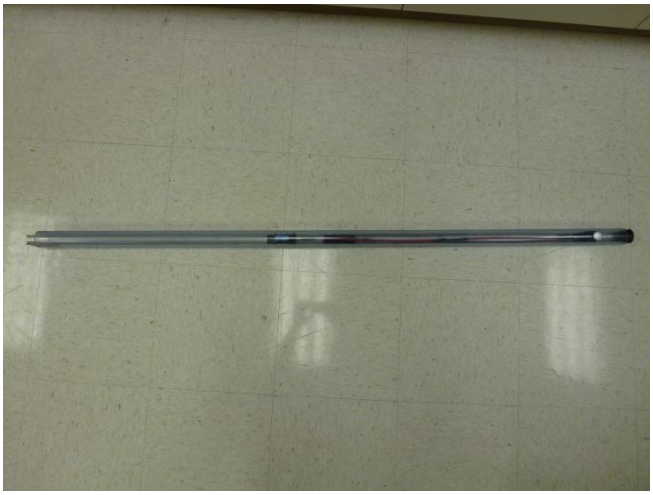

Figure 45. Lenses, fiber optic and prism on metal tray inside of plastic tube.

An improved fiber optic was made and tested in conjunction with a series of lenses and a prism. Testing with the lenses, filters and prisms showed that with the candidate LED and photodiode combination will produce quantifiable results to around 4 parts per billion of fluorescein. Qualitatively the detector can detect the presence of tracer in concentrations of less than 1 part per billion.

All components of the tool will now fit in the same form factor as the heat shield in which the final tool will be housed. The heat-shielded tool is now ready to be designed and fabricated.

Bruce Boyes, Systronix:

Optical Power Efficiency and Sensitivity:
We made a much better fiber optic to power meter adapter based on some COTS components. This has made it much easier to take power measurements along our optical path, and has made those measurements more repeatable.

We experimented with improving the coupling of our LED source into an optical fiber. Using ThorLabs collimator F240SMA-543nm we get 17 mW coupled into a 1000-um fiber, up from 14.3 mW (an increase of 19%). As a result we have improved the design of the LED and photodetector mounting and fiber interface to incorporate these aspheric lens modules.

Improving our alignment procedure we later achieved a coupling of 19.3 mW, an increase of 5 mW (+35%) over the initial best of 14.3 mW.

Continuing last quarter's research into filters we are able to derive some first-order target values for blue vs green extinction, and photodetector sensitivity. Working with Joel Harris and Mike Mella, we found some MUCH better filters (made by Semrock), which give almost textbook-perfect results for the stimulation bandpass and emission longpass.

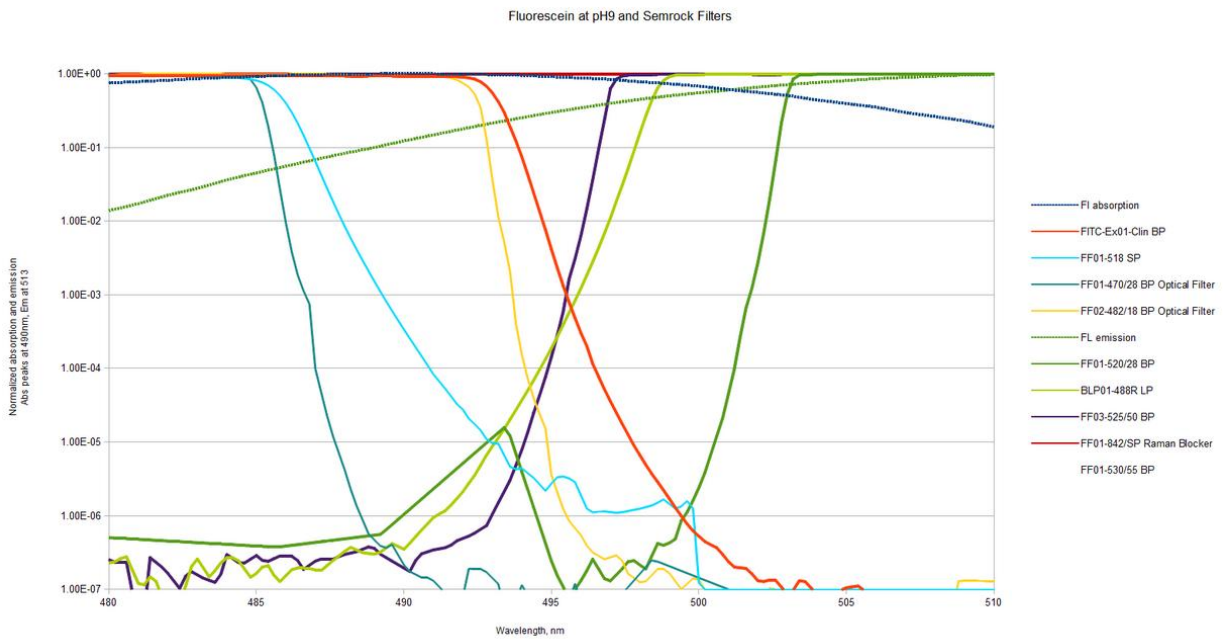

Figure 46. Fluorescein spectra overlaid with Semrock filters we considered. Compare to Figure 42 and notice the vastly better extinction. We settled on the 470/28 and 525/50 filters.

With the improved optical filters, we were able to make significant progress on the sensitivity of the solid-state photodetector. We made some additional discoveries such as learning that the jacket of the optical fiber we use is not opaque enough at the low light levels we can now detect.

We also collected a spectral plot of our actual fiber-coupled stimulation source:

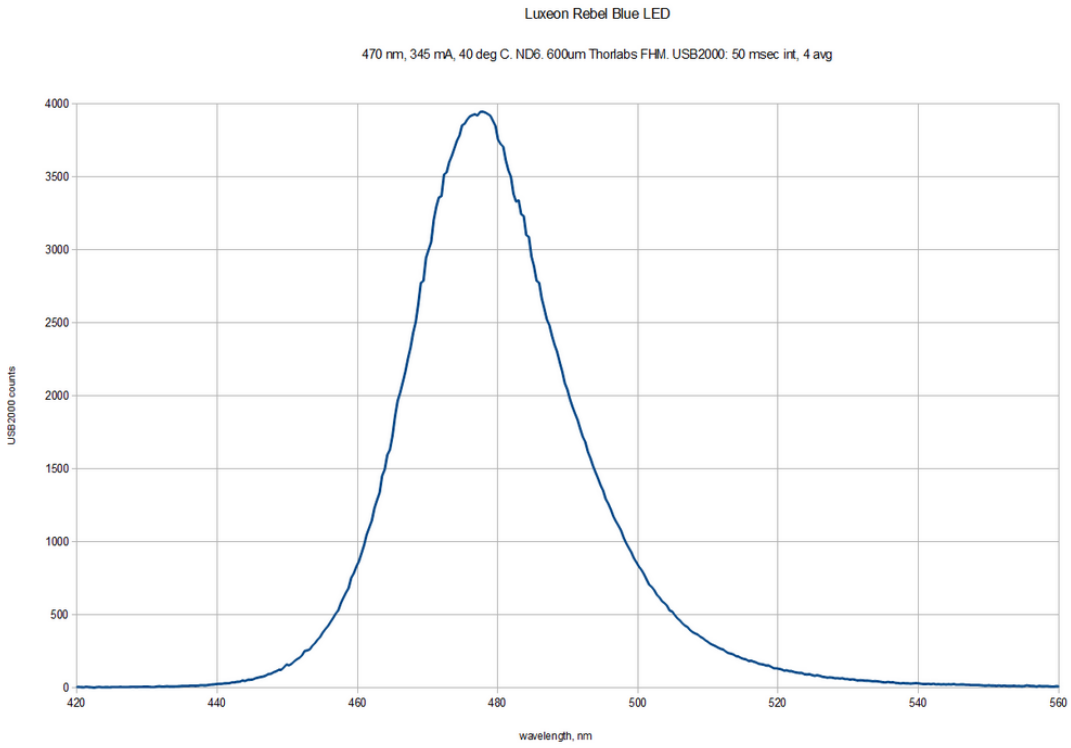

Figure 47. Spectrum of actual blue stimulation source

Now we can plot our actual source with the array of Semrock available filters.

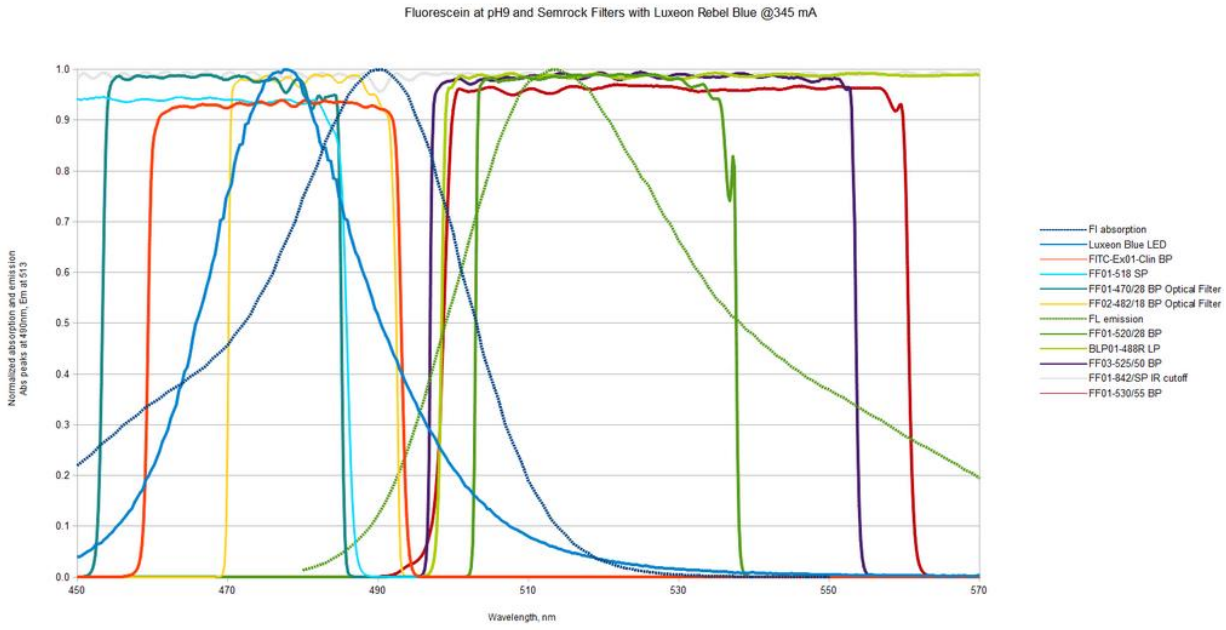

Figure 48. Semrock filter spectra overlaid with measured blue LED spectrum

We moved this version of the optics and electronics into the EGI lab where Mike Mella could make sensitivity measurements (see his report for details). All these developments make the use of the solid-state photodetector look very practical.

Electronics and Related Optics and Mechanics

Now that the optical path is vastly improved we can turn our attention to fitting the electronics into the small (approximately one inch diameter) flask. This has proven to be challenging on several fronts. Due to the nature of the LED and photodetector mechanics and their fiber coupling, some of the circuit boards must be circular and oriented perpendicular to the long axis of the tool. These boards must also have a portion cut away to allow optical fiber and electrical wires to pass.

The LED board also needs to pass up to two watts (peak) from the LED into a heatsink. After considering heat pipes and other difficult but conventional solutions to get heat out of the back of the LED, we hit on the solution of using the collimation lens tube assembly as the heatsink – effectively on the front of the LED. This turned out to be a breakthrough: the collimation tube (a relatively large aluminum cylinder) must be present anyway, and we prefer to have the rear of the LED left open for drive and monitor electronics.

After a bit of struggle thinking of how we can quickly and inexpensively make mechanical structures for the optics and electronics we hit on the idea of fabricating them from FR4 fiberglass PC-board material. This takes advantage of the quick and inexpensive techniques which are used in the manufacture of PC boards.

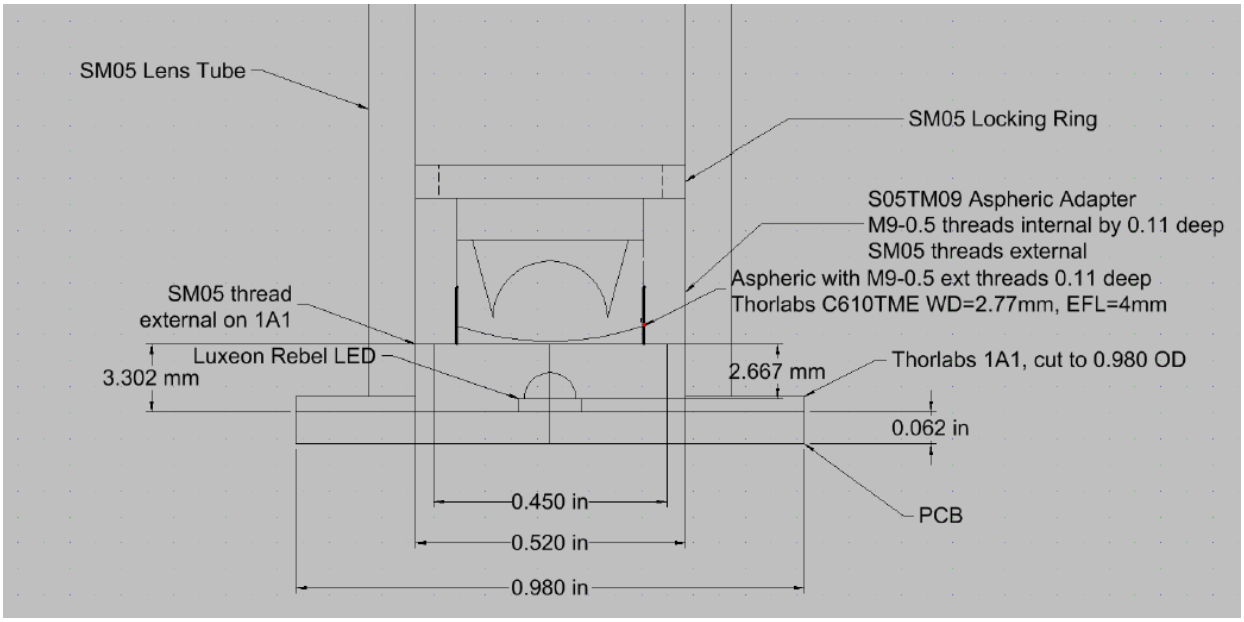

Figure 49. Side view showing how LED and its circuit board mount to the collimation lens tube which also acts as heatsink.

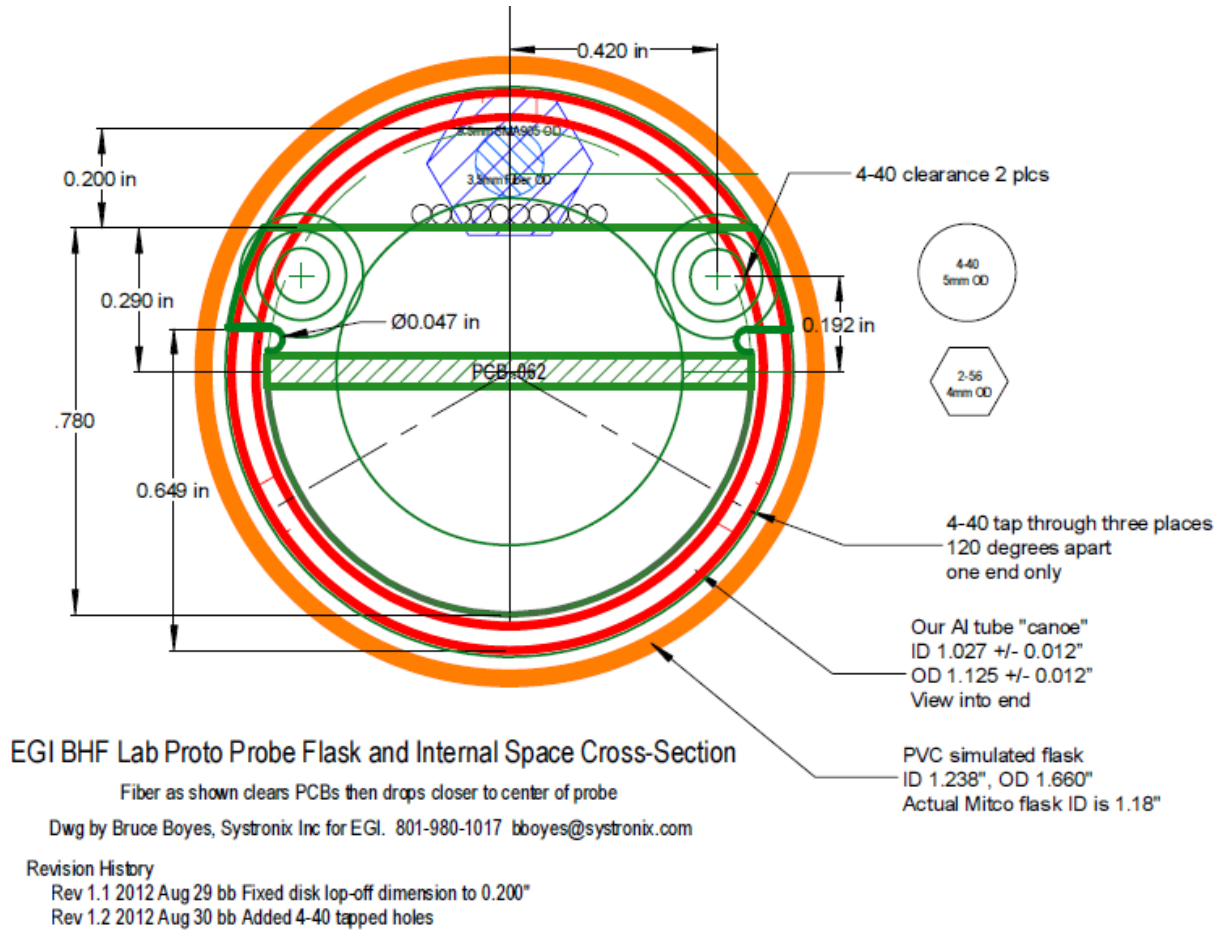

Figure 50. View looking along long axis of tool, showing PC-material circular boards, rectangular boards, and tool bores

Finally here are some 3D views of the front and the back of the LED board, which is nearly complete. In the front view, component PD1 is a new, very small, 125C-capable monitor photodiode, and in the back view components P1 and P2 are very small 9-contact connectors.

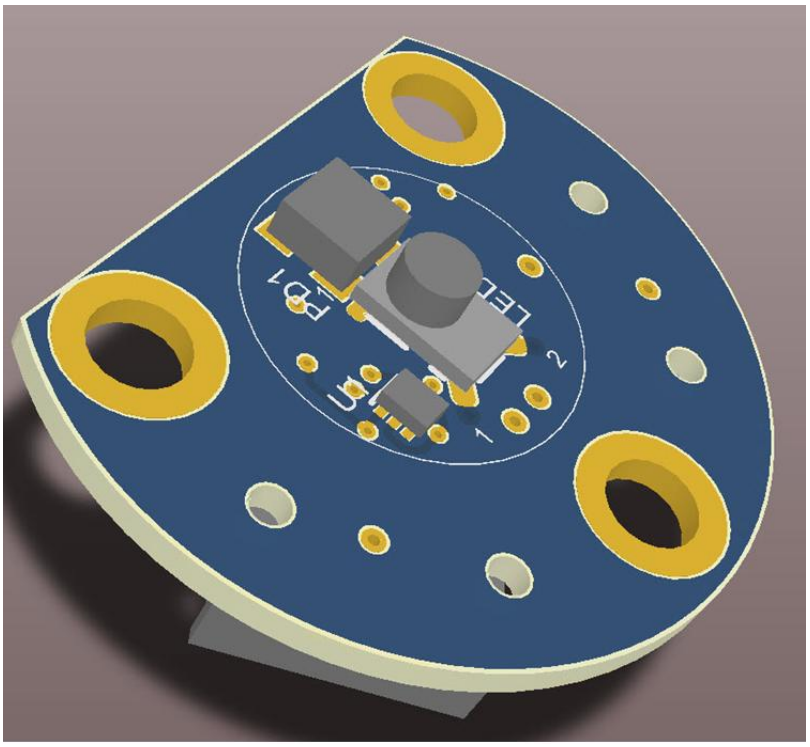

Figure 51. LED board, front side

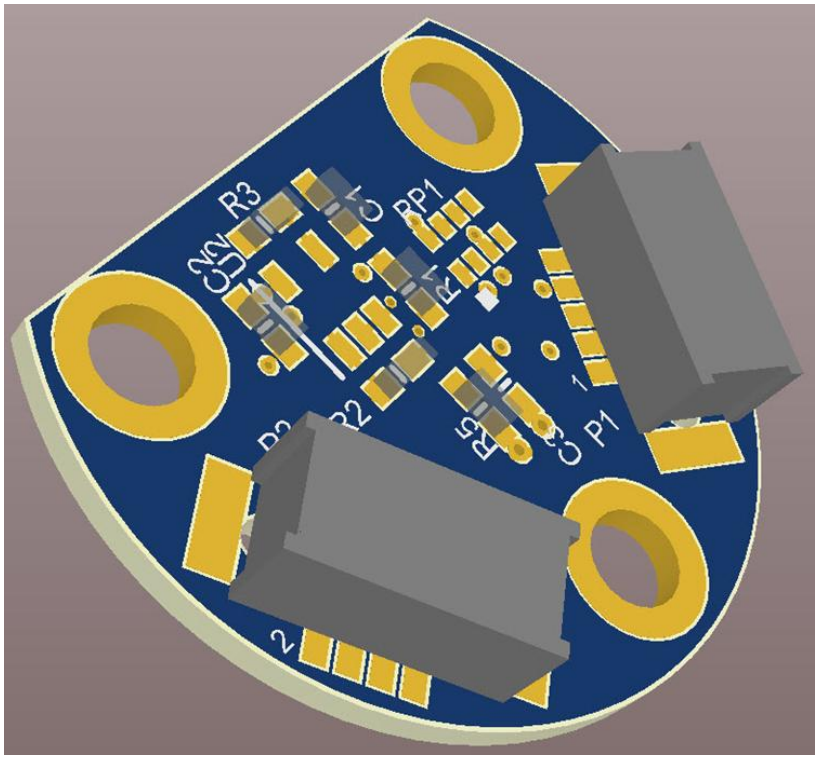

Figure 52. LED board, back side

This board, in turn stacks onto a second board which includes both electronics and a connector which mates one on the rectangular board.

We also found a commercial microcontroller module which is only 0.700” wide, and as short as 1.2 inches long. These will fit onto the rectangular circuit boards. And, they can even be programmed with the easy-to-use Arduino tools!

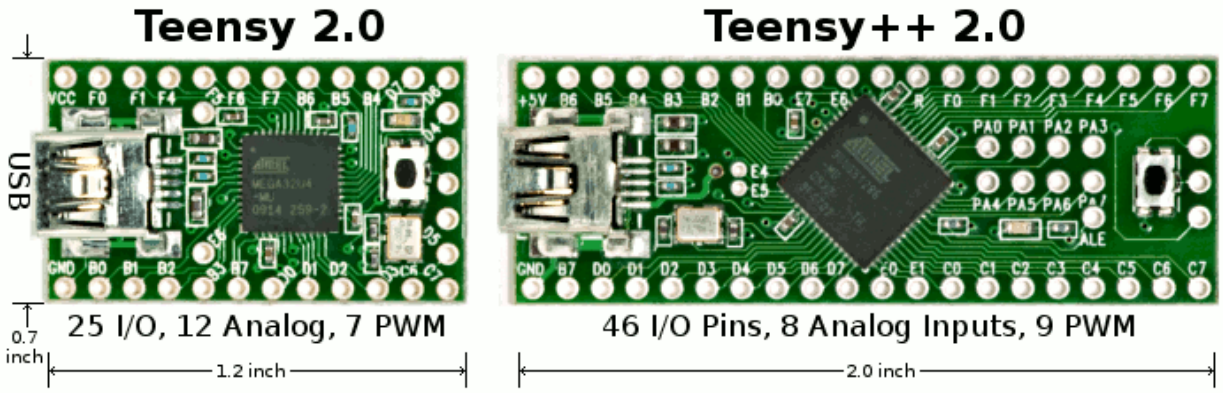

Figure 53. Very small AVR micrcontroller boards from PJRC.

This quarter we also successfully used a development board for a high-resolution 24-bit analog to digital converter (ADC) which has a built-in programmable gain amplifier (PGA). This will be a key component in the solid state photodetector system.

Phase II, Year 5

Progress Report for Year Ending September 30, 2013:

Tracer Methods for Characterizing Fracture Creation in Engineered Geothermal Systems

GO18193

Peter Rose[1], Principal Investigator; Joel Harris[2], Co-Investigator;

Mike Mella[1], Scott Clausen[1], Jeffrey Oates[1], Paul Reimus[5], Cindy Dean[5], Mark Williams[6], Vince Vermeul[6], Bruce Boyes[3], Susan Petty[4]

[1]EGI, University of Utah
[2]Department of Chemistry, University of Utah
[3]Systronics, Salt Lake City
[4]AltaRock Energy, Seattle
[5]Los Alamos National Laboratory
[6]Pacific Northwest National Laboratory

Table of Contents for Phase II, Year 5

Project Objectives

The aim of this project is to develop, through novel high-temperature-tracing approaches, three technologies for characterizing fracture creation within Engineered Geothermal Systems (EGS). The objective of a first task is to identify, develop and demonstrate sorbing tracers for characterizing interwell reservoir-rock surface areas and fracture spacing. The objective of a second task is to develop and demonstrate a methodology using reactive tracers for measuring fracture surface areas adjacent to single wells. The objective of a third task is to design, fabricate and test an instrument that makes use of tracers for measuring fluid flow between newly created fractures and wellbores. In one method of deployment, it will be used to identify qualitatively which fractures were activated during a hydraulic stimulation experiment. In a second method of deployment, it will serve to measure quantitatively the rate of fluid flowing from one or more activated fracture during a production test following a hydraulic stimulation.

Task 4.1: Select an Adsorbing Tracer for a Field Test for Characterizing Interwell Fracture-Surface Area in a Geothermal Reservoir

First Quarter, 2013 (Kevin Leecaster and Jeff Oates)

Alkali Metal Ion Reactive Tracer Evaluation

Summary

Retardation of lithium and cesium ions on the minerals expected on the fracture surfaces exposed during the Newberry stimulation was further examined. We continued our investigation of their hold-up by performing 'interwell' flow tests at higher temperatures on the same geomedium and with the same solution as last quarter. A different solution chemistry was also tested and another geomedium was constructed that includes the minerals chlorite and epidote.

Methods

The alkali metal ion retardation examination was conducted on the trimix461 geomedium constructed from approximately equal masses of quartz, calcite, and albite described last quarter while the new mixture of materials was being prepared at LANL by other team members. This new five part medium was constructed from minerals that were ground, annealed, and sieved to be between ½ and ¼ mm. The mixture of equal parts quartz, calcite, epidote, chlorite, and albite was homogenized by repeatedly passing through a sample splitter and then 407.2 g were packed into one of our 20" long 1" id SS column with ~0.5 g of borosilicate glass wool packed on both ends. We used both the alkaline earth metal-rich-modified pad 29 analogue solution previously described last quarter as well as a new solution iteration with more carbonate, silicate, sodium, and potassium, but without any addition of Ca or Mg salts (Table 4). All the experiments described in this report had flow rates of approximately 2 ml/min as monitored by weighing a portion of the effluent fractions collected. Fractions were collected in aliquots of 4 – 8 ml and analyzed by high pressure liquid chromatography using a conductivity and fluorescence detector for the cations and 1,5-NDS respectively.

Table 4. Newberry field sample and laboratory solution chemical concentrations (millimolal).

	Ca^{+2}	Mg^{+2}	K^{+1}	$*Na^{+1}$	Li^{+1}	Cs^{+1}	$*CO_3^{-2}$	$*Cl^{-1}$	SO_4^{-2}	Br^{-1}	$1,5\text{-}NDS^{-2}$	CHO_2^{-1}	H_4SiO_4
pad 29 reported analysis	0.47	1.02859	0.128	1.914			4.754	0.10	0.026				2.13523
Ca/Mg flush solution	0.270	0.25748	0.12	0.247			0.596	0.40	0.0341				0.336
Ca/Mg Li solution	0.26	0.26263	0.127	0.329	1.23		0.602	0.38	0.0332	1.23	0.0373		0.345
Ca/Mg Cs solution	0.27	0.25748	0.125	0.333		1.377	0.601	0.38	0.0332		0.0426	1.38	0.336
K flush solution			3.076	3.89			4.84	0.09	0.0523				2.69
K Li solution			3.087	3.99	1.22		4.84	0.48	0.0575		0.0430		2.69
* Concentration prior to sparging with CO2 or adusting with NaOH and/or HCl to the target **pH 8**													

It was observed that the method-of-moments technique of retardation estimation had a high error (large coefficient of variation) for these experiments. The previously described method of using linear interpolation to compare the volume of flow required to elute equal tracer concentrations was not available due to the low resolution provided by the fractions collected. The curves were fit to the advective-dispersion equation (ADE) using the analytical solution:

$$A(x,t) = 0.5\left(erfc\left[\frac{Rx - vt}{\sqrt{4DRt}}\right] + \exp(P)\, erfc\left[\frac{Rx + vt}{\sqrt{4DRt}}\right]\right)$$ (van Genuchten and Alves, 1982)

where x, t, R, v, and D are the transport distance (51.5 cm), time (when fraction half collected), retardation factor, pore water velocity, and dispersion coefficient, respectively. P is the Peclet number ($P = {vx}/{D}$). R was maintained at unity for the conservative tracers and the 'best' fit was determined by minimizing the squared difference of the observed and predicted effluent concentrations using Excel's solver macro. The graphical user interface Stanmod (Simunek *et al*, 1999) was used to fit the observed data to the two-site chemical non-equilibrium convective-dispersion model (NADE) within the CXTFIT program (Toride *et al*, 1995) for the reactive tracers using the average dispersivity (λ) determined from the mean of the values from both the loading and unloading step curves for the conservative tracers' ADE-derived average-pore-water velocities and hydrodynamic dispersions, D = λv. This provided an indication of how far from equilibrium behavior the alkali metal ion curves exhibited through the two model parameters β & ω. These parameters represent the proportion of sites exhibiting instantaneous equilibrium behavior and a first-order rate parameter for the other fraction of reactive sites, respectively.

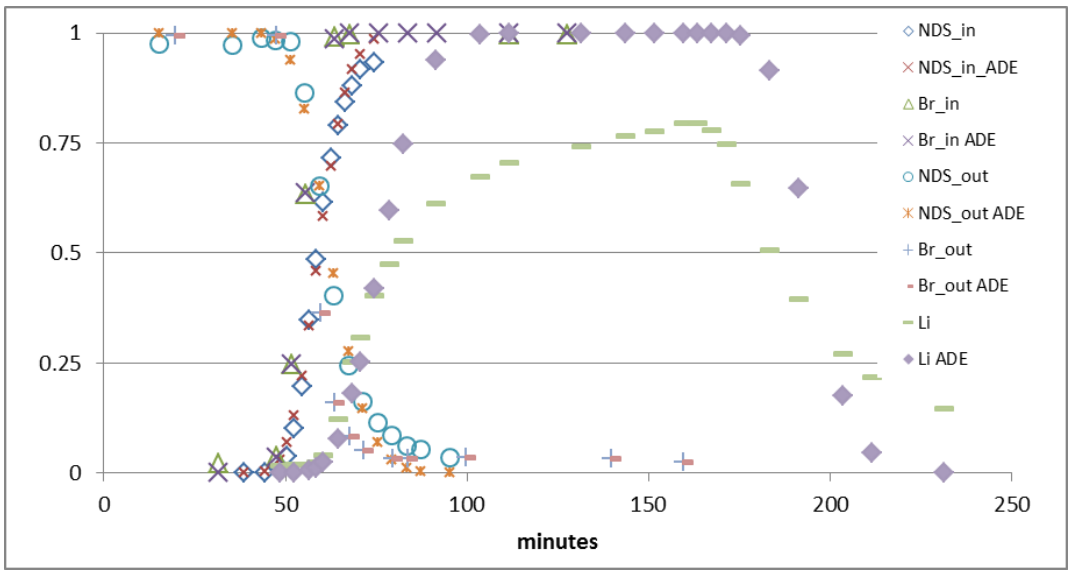

Figure 3: Breakthrough curve of 119 minute pulse at flow rate of 2.02 g min^{-1} of Li^{+} and 1,5-NDS in Ca/Mg pad 29 analogue solution through trimix461 geomedium at a mean column temperature of 134.9 °C between the column inlet and outlet over the course of the experiment with a coefficient of variation (CV) of 1.2%.

The ADE model worked well for the conservative tracer breakthrough curves examined during the course of this project. Therefore, based on a departure from ADE observed in the Li and Cs experiments on the trimix461, these reactive tracers did not exhibit equilibrium-type behavior (Figure 1). In order to further assess this apparent finding we reexamined some of the earlier reported Li^{+} tests performed on a geomedium constructed from only 425 to 500 µm quartz Ottawa sand grains for indications of non-equilibrium in these experiments. These experiments were performed by flowing 9 ppm tetraethylsilicate flush solution and using the same flush spiked with 20 ppm LiBr and 100 ppm disodium naphthalene disulfonate (1,5-NDS). The experiments were performed at flow rates of 2 ml min^{-1} with pH's of 5.1 (Figure 2). These breakthrough curves exhibited apparent equilibrium-type adsorptive (loading) behavior at the three lowest temperatures (Table 5), but there appears to be non-equilibrium mass transport in the 90 °C experiment. For all of the experiments there was a low (~20%) proportion of the reactive sites, as model described, that exhibited non-equilibrium mass transfer between the stationary and mobile phases during desorption (unloading) keeping in mind that a mathematical model-fit doesn't independently infer appropriate physical model selection.

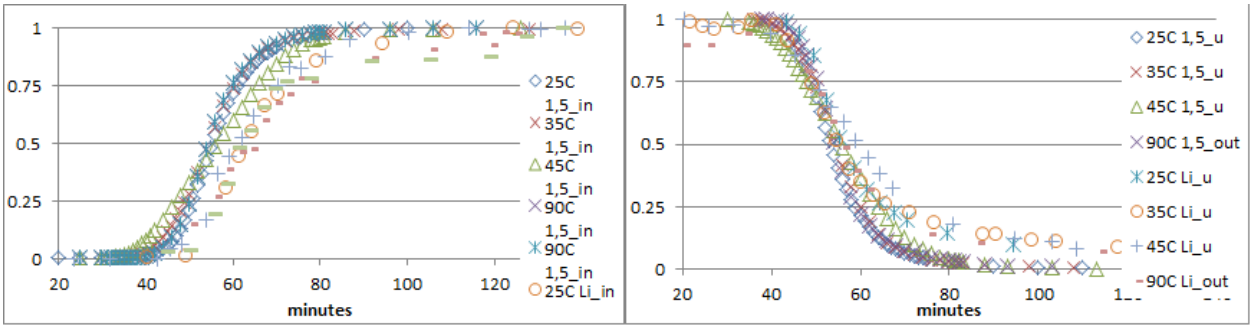

Figure 4: Breakthrough curves of step injections of lithium in simple solution of TEOS spiked with 1,5 NDS and LiBr through column filled with Ottawa sand. No clear trend was seen between temperature and Li retardation in these experiments on quartz.

Table 5: Advective-dispersion equation derived parameters from experiments on quartz at different temperatures. Results indicate that there is some moderate kinetic sorption behavior exhibited in the unloading curves and in both curves as the temperature increases. There is significantly anomalous dispersivity of the 45 °C that did not appear in the following experiment on the same column so probably represents spectrometer drift.

	Loading					Unloading				
Temp (°C)	λ	Rf (ADE)	Rf (NADE)	β	Ω	λ	Rf (ADE)	Rf (NADE)	β	Ω
44.8	1.4	1.147	1.113	0.9999	100	1.2	1.07	1.15	0.8560	0.0097
24.9	0.505	1.14	1.19	0.959	0	0.5022	1.0697	1.2170	0.8409	0.0042
35.0	0.667	1.13	1.12	0.9999	100	0.5852	1.0290	1.2250	0.7796	0.0060
89.2	0.501	1.16	1.34	0.833	0.0044	0.4488	1.0218	1.1310	0.8457	0.0076

In contrast to the equilibrium or near equilibrium retardation behavior seen on the quartz-only experiments performed below 100^{o}C, all of the column experiments using mineral mixtures and solutions representing more 'natural' water chemistry definitively did not fit the equilibrium-based ADE model as evidenced by the poor fit with equilibrium-based curves shown in Figures 1 and 3.

Table 6 provides the determined NADE model parameters for this series of experiments. The solution without the divalent alkaline earth metals showed the lowest retardation as well as behavior that could more closely be represented by the model with instantaneous adsorption (ADE), but still there was obvious deviation from simple cation exchange reactions with the particle surfaces (Figure 3). Nonlinear Li sorption might be expected on the more reactive minerals based on previous investigations (for example Anghel *et al*, 2009), but this will make interpretation of injection backflow signals subject to significant reliance on the flow model selection and parameter estimation certainty leading to ambiguity in surface area estimates (Behrens *et al*, 2002).

All of the reactive tracers tested to date during this research have shown increasing nonlinear behavior with increasing temperature as shown in Tables 5 & 6 for the alkali metal ions (data not shown for previously reported rhodamine, safranin, or erioglaucine experiments). Other project

team members are working to address this issue through development, calibration, and verification of selectivity-coefficient-based transport models.

Table 6: Results of interwell alkali metal ion reactive tracer tests supporting the Newberry EGS stimulation project on trimix461 geomedium consisting of quartz, calcite, and albite. There is a clear trend in the Li experiment results of increasing retardation with temperature in the tested range as well as increasing proportion of non-equilibrium character (1-β). The trend (if there is one) in the Cs experiments may be somewhat 'smeared' by the significantly shorter 40 minute tracer pulse applied on 9/26/12.

Date	Solution	temp (°C)	Rf(NADE)	β	Ω	λ, in	λ, out
01/03/13	Li K sol'n	119.4	1.502	0.777	0.003	0.250	0.359
9/24/12	Li Ca/Mg	119.8	2.015	0.555	0.012	0.199	0.245
9/12/12	Li Ca/Mg	120.2	3.296	0.356	0.013	0.130	0.286
11/14/12	Li Ca/Mg	120.3	2.089	0.531	0.007	0.253	0.315
12/5/12	Li Ca/Mg	134.9	2.361	0.491	0.010	0.292	0.421
10/22/12	Li Ca/Mg	149.3	4.615	0.258	0.020	0.296	0.486
12/10/12	Li Ca/Mg	174.5	7.081	0.141	0.058	0.502	0.691
9/26/12	Cs Ca/Mg	119.4	6.374	0.329	0.040	0.208	na
10/8/12	Cs Ca/Mg	120.0	4.638	0.423	0.015	0.177	0.313
12/26/12	Cs Ca/Mg	148.4	8.801	0.217	0.029	0.395	0.892

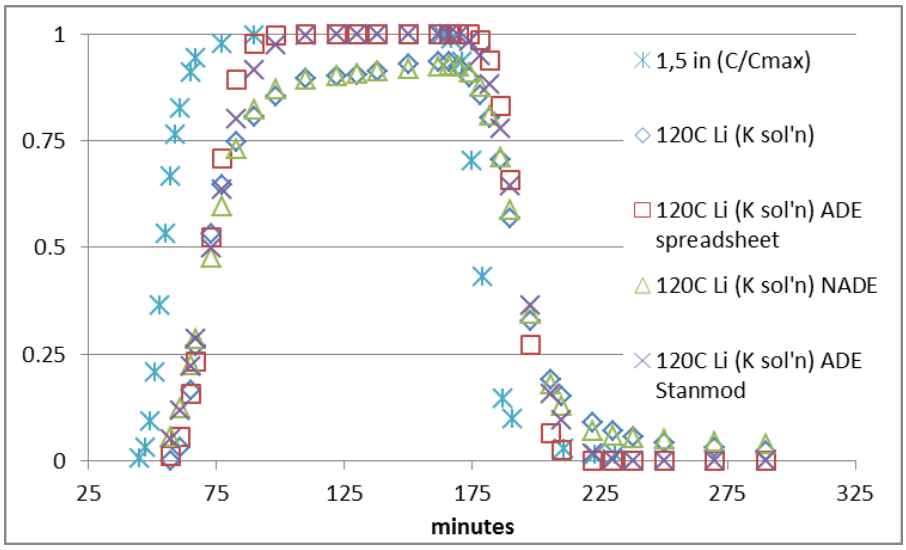

Figure 5: January 3rd, 2013 2 ml min-1 interwell experiment through trimix461 geomedium examining the effect of changing the solution chemistry. The Li was retarded less compared to when the divalent cations were included in the flow solutions and while the adsorption still did not exhibit instantaneous, linear sorption it exhibited less non-equilibrium behavior than with the alkaline earth metals in the solutions.

For the alkali metal ions, a significant proportion of the non-linear transport would be expected to be caused by precipitation reactions in the solutions with high carbonate concentrations (Caley and Baker, 1939). A preliminary, screening investigation was made by heating the test solutions in quartz ampules in order to monitor whether a change in the alkali metals would be apparent.

These results showed no difference in the Li concentration of the solutions caused by heating. This might indicate that if precipitates formed when the temperature increased then they re-dissolved during the cooling period prior to the sampling the fluid for analysis. Examination of the cation concentrations for the analyzed components from two interwell experiments (Figure 4) shows a general trend of an initial increase in Na and K concentrations as the Li concentration of the effluent increases followed by a distinct decrease in the K concentration following the switch to the flush solution. The Na concentration also decreased as the pore water Li concentration decreased too, but less distinctly and appeared to establish a relatively stable concentration whereas the K concentration steadily increased following its initially rapid decline following Li unloading from the column.

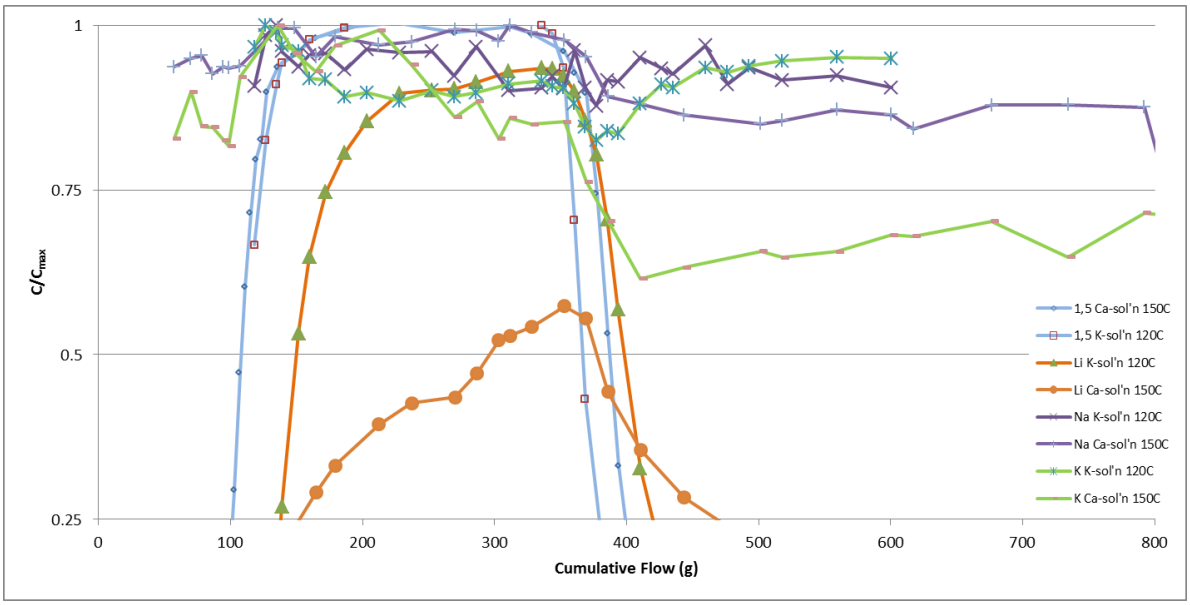

Figure 6: Potassium and Na concentration overlain on BTC's from two interwell Li tests on the trimix461 geomedium. The 120 °C experiment was with the K-rich solution while the 150 °C experiment used the solution containing Ca and Mg. The initial increase in K concentration in the effluent after the Li is introduced would appear to relate to reactive site selectivity, but precipitation reactions should not be ignored including less common ones with very limited thermodyanamic data available e.g. $KLiCO_3$ (Kirfel et al, 2000). The rapid K decline after Li pore water concentrations began to decrease could also be explained by K adsorption as the Li desorbs, but its decline below the initial 'steady' state and its apparent slow return will probably require further investigation with reactive transport models which can simulate precipitation reactions.

References

Anghel, I., H. J. Turin, and P. W. Reimus, 2002, Lithium sorption of Yucca Mountain tuffs, *Applied Geochemistry*, **17**: 819-824.

Behrens, H., I. Ghergut, M. Sauter, and T. Licha, 2009, Tracer properties, and spiking results (from geothermal reservoirs), Proceedings: 34th Workshop on Geothermal Reservoir Engineering, Stanford University, CA.

Caley, E. R. and A. L. Baker, Jr., 1939, Sensitivity of the carbonate test for lithium, Industrial and Engineering Chemistry, **11**(2):101-102.

Kirfel, A. H. Euler, B. Barbier, E. Hägele, and H. Klapper, 2000, Potassium lithium carbonate, $KLiCO_3$: Single-crystal x-ray structure analysis and thermal expansion, Crystalline Materials, **215**(12): 744.

Simunek, J., M. Th. van Genuchten, M. Sejna, N. Toride, and F. J. Leij, 1999, The STANMOD computer software for evaluating solute transport in porous media using analytical solutions of convective-dispersion equation, Version 2.0, US Salinity Laboratory, Agricultural Research Service, United States Department of Agriculture, Riverside, California.

Toride, N., F. J. Leij, and M. Th. van Genuchten, 1995, The CXTFIT code for estimating transport parameters from laboratory or field tracer experiments, Version 2.0, Research Report 127, US Salinity Laboratory, Agricultural Research Service, United States Department of Agriculture, Riverside, California.

van Genuchten, M. Th., and W.J. Alves, 1982, Analytical solutions of the one-dimensional convective-dispersive solute transport equation, *Technical Bulletin 1661*, U. S. Department of Agriculture.

First Quarter, 2013 (Scott Clausen)

We have been testing new candidates for interwell tracers for use in geothermal reservoirs. We purchased three new tracer candidates (Figure 5). Of these candidates, we have only done preliminary analyses on Tinopal CBS-X. Our tests have shown Tinopal CBS-X to be quite stable at high temperatures, with 86.4 ± 3.5% remaining after baking at 230°C for two days in pH 7 buffered solution. Tinopal CBS-X also appears to sorb strongly onto silica at ambient temperatures. While we did see a small breakthrough, the mass recovery was very low (Figure 6). Further tests will need to be performed at higher temperatures to assess this compound's potential as a geothermal sorbing tracer.

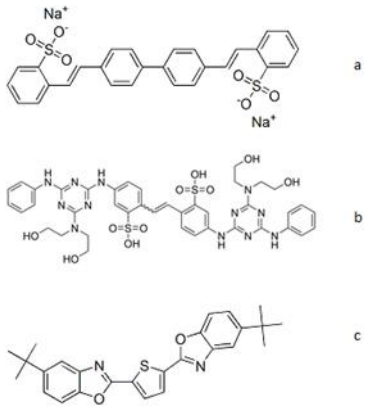

Figure 5. Chemical structures of three tracer candidates. a) Tinopal CBS-X. b) Fluorescent Brightener 28. c) Fluorescent Brightener 184.

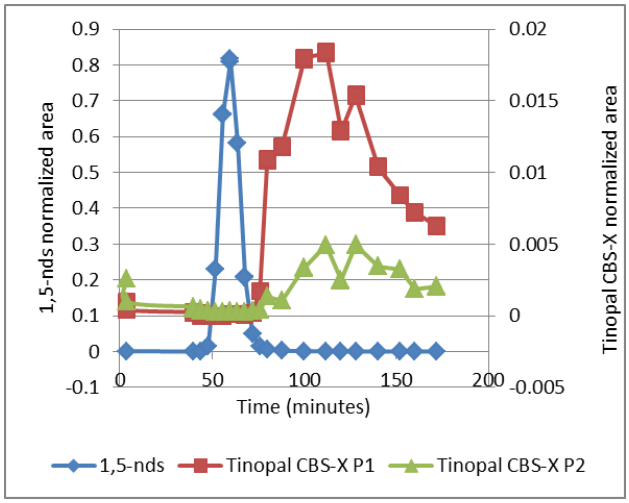

Figure 6. Breakthrough curves of 1,5-nds (conservative tracer) and Tinopal CBS-X (potential reactive tracer) through a silica-sand column at ambient temperature. Red and green lines represent the two different compounds of Tinopal CBS-X.

Second Quarter, 2013

Jeff Oates, EGI

Interwell flow-through experiments were conducted to determine the retardation of Li with respect to temperature. Three experiments were done, one at each temperature of 125°C, 150°C, 175°C. The experiment conditions were meant to complement the work at LANL, where higher temperature experiments were being conducted. For this reason a similar geomedium was constructed from equal parts by mass of 500-250 µm albite, chlorite (this was pre-sieved to avoid the clogs that LANL experienced), calcite, epidote, and sand, all of which were annealed at 450°C for 48 hours. The flush solution chemistry replaced all divalent cations found in the Newberry well solution chemistry with potassium salts. The potassium solution chemistry was:

7.5 mg/L KCl, 298.7 mg/L $KHCO_3$, 156.4 mg/L $NaHCO_3$, 7.4 mg/L Na_2SO_4, 96 mg/mL H_4SiO_4. The tracer solution was made from the flush solution with the addition of LiCl and 1,5-naphthalene disulfonate, 51 mg/L and 10 mg/L respectively.

Experiments were run at a flow rate of 0.2 ml/min for the 125°C and 0.5 mL/min for the 150°C and 175°C runs. The tracer was run as a step through the column. The effluent of the run was collected as fractions that were analyzed by HPLC using conductivity and fluorescence detectors. The resulting data was then plotted versus flow volume to produce the breakthrough curves of the analytes. Figure 7 contains the breakthrough curves for the three runs.

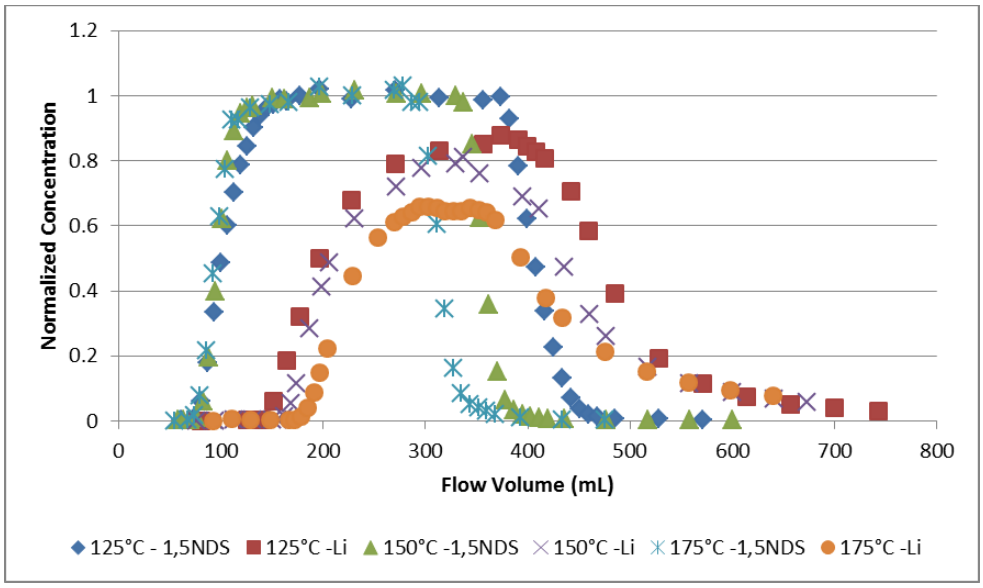

Figure 7. Plots of the tracer responses for the three experiments. Note that as the temperature increased the Li loading curves were retarded incrementally.

Using the method of moments and the break-through-curve data, the retardation factors (R_f) were calculated with respect to the 1,5-NDS curves. The R_f value of the three experiments are listed in Table 1.

Table 1: Retardation factors of LiCl relative to the conservative tracer 1,5-naphthalene disulfonate at three temperatures

Temperature (^oC)	R_f
125	1.98
150	2.30
175	2.73

Cindy Dean and Paul Reimus, LANL

Laboratory experiments were conducted to estimate cation exchange parameters for lithium and cesium ions to facilitate interpretations of tracer tests at Newberry Crater, OR. The materials used in the experiments included a crushed (250-500 μm) and annealed (450ºC for 48 hr) mineral

assemblage representing reservoir fracture coatings comprised of roughly equal mass fractions of chlorite, albite, calcite, epidote and quartz and a synthetic water having chemistry matching that of Newberry Crater injection water. Batch sorption experiments using lithium were performed at room temperature to obtain estimates of site-specific cation-exchange parameters. In addition, to study cation-exchanging tracer transport relative to that of a conservative tracer (1,5 naphthalene disulfonate (NS)), flow-through column transport experiments were performed at EGI and LANL using a synthetic Newberry water with potassium salts substituted for magnesium and calcium salts to reduce mineral precipitation. The experiments were performed using the above mineral assemblage at temperatures ranging from 125 ºC to 275ºC. A more detailed description of the materials (LANL and EGI) and methods for the LANL experiment can be found in Dean, Reimus et al. (2013). These experiments were conducted to verify that the parameters determined in the batch experiments can be effectively applied under the dynamic flow conditions and temperatures expected in the field tracer tests.

Conservative tracer data from the Newberry laboratory experiments were fit using the semi-analytical model RELAP described in Section 4 to determine column parameters of residence time (τ) and Peclet number (Pe). EGI laboratory experimental data using LANL column parameters were simulated using MULTRAN described in Section 5. For these simulations the transport of cation exchanging tracers is simulated using the mass action expressions in Equation 1 for the cation-exchange reactions in Equation 2, while maintaining the surface cation balance and solution charge balance in Equations 3.

$$K_{Na/I} = \frac{[NaX][C^{i+}]^{1/i}}{[Na^{+}][CX_i]^{1/i}} \tag{1}$$

$$Na^{+} + \frac{1}{i}CX \Rightarrow NaX + \frac{1}{i}C^{i+} \tag{2}$$

where C = cation with charge = *i and X = surface site with charge -1*,

$$CEC = \frac{\varphi}{\rho_B}\sum_{all\ C}[CX_i] \qquad \sum_{all\ C}[C^{i+}] = \sum_{all\ A}[A^{i-}] \tag{3}$$

where $[A^{i-}]$ = concentration of surface species of charge *i*
CEC = measured cation-exchange capacity

Room Temperature Lithium Batch Experiments

Figure 8 contains the mineral surface areas, lithium CEC calculation, and average K_d of the mineral fractions contained in the mineral assemblage (mix) for Li^+ (left) and Cs^+ (right). The combined fractional surface area of the minerals (sum of the product of fractions and specific surface areas) is twice that measured by BET for the mix, which is most likely due to sample inhomogeneity. The combined fractional Li^+ CEC of the minerals (sum of the product of fractions and CECs) is 3.49 meq/kg, slightly lower than that measured in the mix (4.40 meq/Kg). The combined fractional Cs+ CEC of the minerals (sum of the product of fractions and CECs) is

4.86 meq/kg, slightly higher than that measured in the mix (4.39 meq/Kg). Chlorite, having the greatest surface area and CEC, contributes most to cation exchange in the mix. Additional batch experiments were performed with the mineral mix using a synthetic water in which all the calcium and magnesium salts in the Newberry water recipe were substituted with potassium salts. This K-substituted water was used in all high-temperature flow-through experiments because calcite ($CaCO_3$) and magnesite ($MgCO_3$) were predicted to be significantly supersaturated at the higher temperatures, and we were concerned that such precipitation could interfere with lithium and cesium transport via co-precipitation reactions and also that it might significantly decrease the permeability of the reactor, possibly leading to plugging. The sorption of Li^+ (left) and Cs^+ (right) in the mineral mix using the K-substituted water and the water containing Ca and Mg is shown in Figure 9. The Li^+ K_d value for the mineral mix in the K-substituted water is slightly higher at 1 and 5 ppm starting concentrations and slightly lower in the 25 ppm starting concentration than in the original Newberry water; both are quite low and the difference is most likely attributable to experimental error. The Cs^+ sorption for the mineral mix in the K-substituted and original Newberry is similar to the Li^+ result.

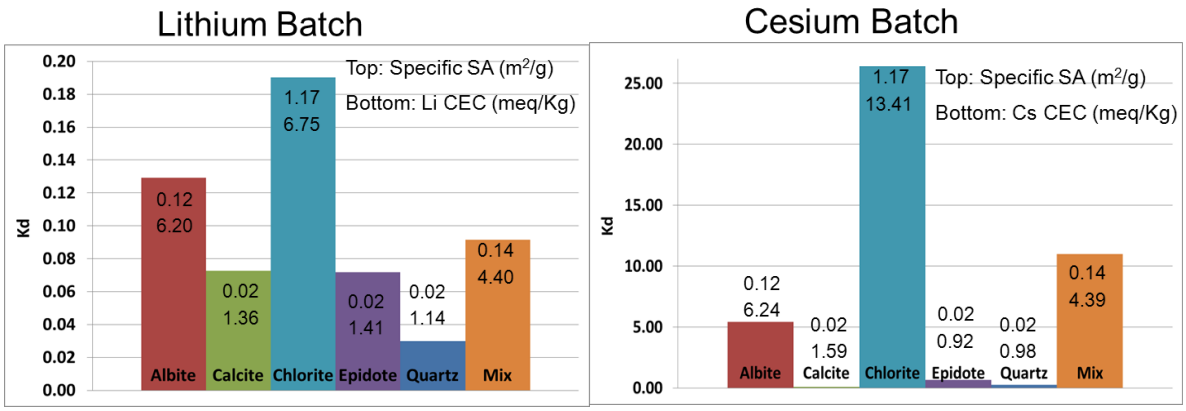

Figure 8. Lithium (left) and cesium (right) room temperature batch experimental results.

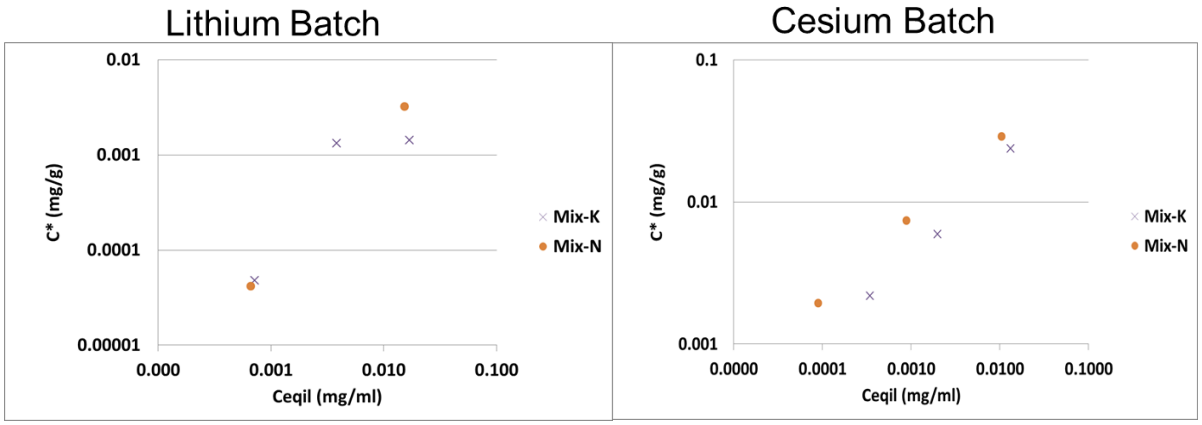

Figure 9. Log-log plots of Li (left) and Cs (right) batch experiments at ~1ppm, ~5ppm and ~25ppm comparing sorption in K-substituted water in the mix (mix-K) and in the original Newberry water (mix-N).

Column Transport Experiments and Modeling

Figure 10 shows the EGI and LANL dynamic column flow through experimental data at various temperatures along with the RELAP fits of the conservative tracer and MULTRAN fits of the Li^+ breathrough curves. The NS tracer responses were reproducible at different temperatures in both the LANL and EGI experiments, although the residence times and tracer pulse times were quite different in the LANL (~10 hr residence time, ~2.5 hour tracer pulse) and EGI (~8 hr residence time, ~22 hour tracer pulse) experiments. The increased Li^+ retardation with increased temperature indicates a temperature depence for Li^+ cation-exchange. The Li^+ data for all four temperatures were fit using the same cation exchange parameters, execpt for the selectivity coeficient, $K_{Na/Li}$, which is expected to have a dependence on temperature (Gaines 1955; Kraus and Raridon 1959). Also, the matching of the Li^+ breakthrough curves was possible only if cation-exchange was assumed to occur in a diffusive/sorptive boundary layer on grains, as shown in the schematic below.

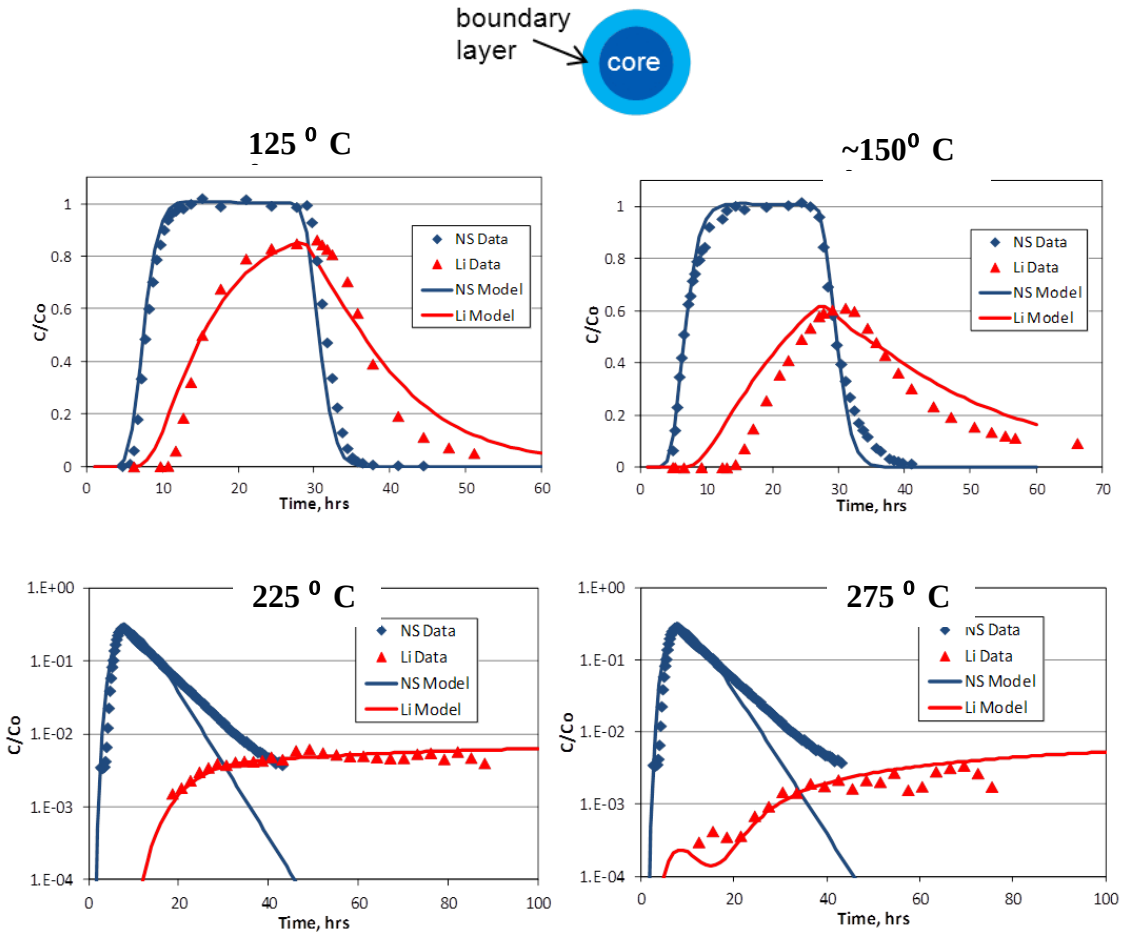

Figure 10. NS and Li^+ experimental data and model fits (normalized concentration vs. time). Upper left: EGI T=125ºC, ~8 hr residence time, ~22 hour tracer pulse; Upper right: EGI T=~150ºC, ~8 hr residence time, ~22 hour tracer pulse; Lower left: LANL T=225ºC, ~10 hr residence time, ~2.5 hour tracer pulse; Lower right: LANL T=275ºC, ~10 hr residence time, ~2.5 hour tracer pulse;

Figure 11 shows the NS, Li^+ and Cs^+ experimental data and model fits at 225^{0}C in the LANL columns. A minor modification of the CEC value was required to fit the Cs^+ data. This may be due in part to mineral alteration during the 275 ^{0}C Li^+ experiment before the temperature was decreased to 225 ^{0}C for the Cs^+ experiment. Cesium is a stronger cation exchanger than lithium at room temperature, therefore it was expected that cesium would be more retarded in the column experiment than lithium. However, it is apparent that the cesium was slightly less retarded than the lithium at 225^{0}C. A possible explanation for this result is that higher temperatures tend to disrupt the waters of hydration that surround alkali metals (Li, Na, K, Cs) at lower temperatures (Gast and Klobe). Being the smallest cation (highest charge to size ratio), lithium tends to be the most hydrated of the alkali metals, which is widely believed to be why it is the weakest exchanger of all the alkali metal cations. In contrast, cesium exchanges very strongly with other cations because it is poorly hydrated. However, as temperatures increase, thermal energy disrupts the waters of hydration surrounding the cations, and this effect is biggest for lithium. A higher ionic strength flushing solution was introduced after approximately 80 hours (see note on Figure 11) that resulted in a subsequent increase in Cs^+ breakthrough, which was qualitatively reproduced by MULTRAN. This inadvertant increase in ionic strength of the flushing solution provided a validation test of sorts for MULTRAN.

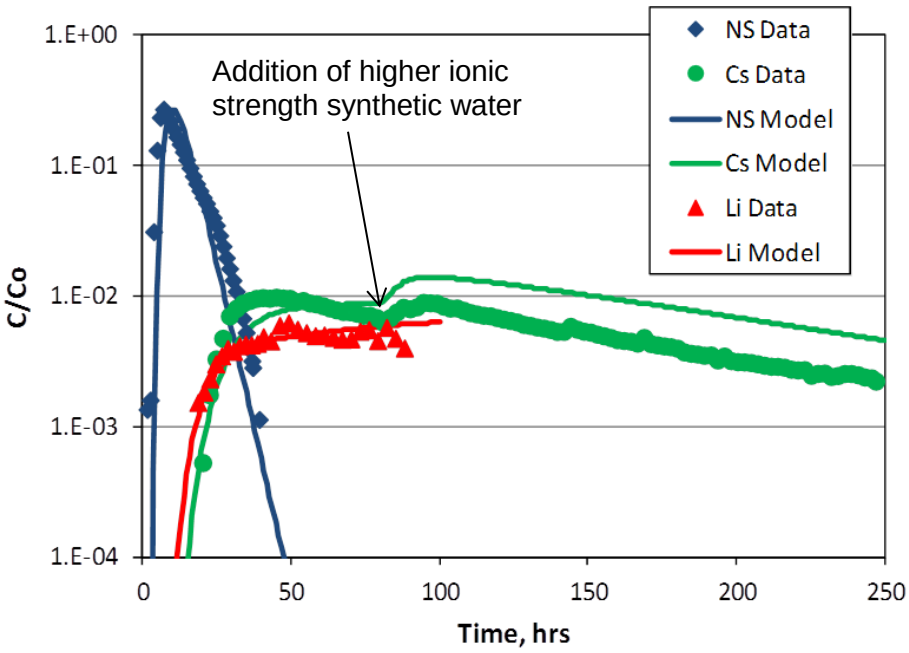

Figure 11. NS, Li^+ and Cs^+ experimental data and model fits at 225 ^{0}C in the LANL columns (~10 hr residence time, ~2.5 hour tracer pulse) (Normalized concentration vs. time).

Figure 12 shows Li^+ breakthrough curves from MULTRAN simulations assuming that all experiments were conducted with 2.5-hr tracer pulses and 10-hr residence time (the LANL experimental conditions). The Li^+ breakthrough at 25^{0}C, predicted using a retardation factor of

1.3 based on the batch sorption data, overpreditcs the lithium breakthrough at higher temperatures. These simulations illustrate the extreme temperature dependence of Li^+ in the column transport experiments. The only adjusted parmater in the simulations is $K_{Na/Li}$, which decreases with increasing temperature. A plot of Log $K_{Na/Li}$ as a function of inverse temperature (Figure 12, right) shows a nearly linear dependence. This is advantageous in predicting Li^+ breakthrough at temperatures that differ from those in the experiments.

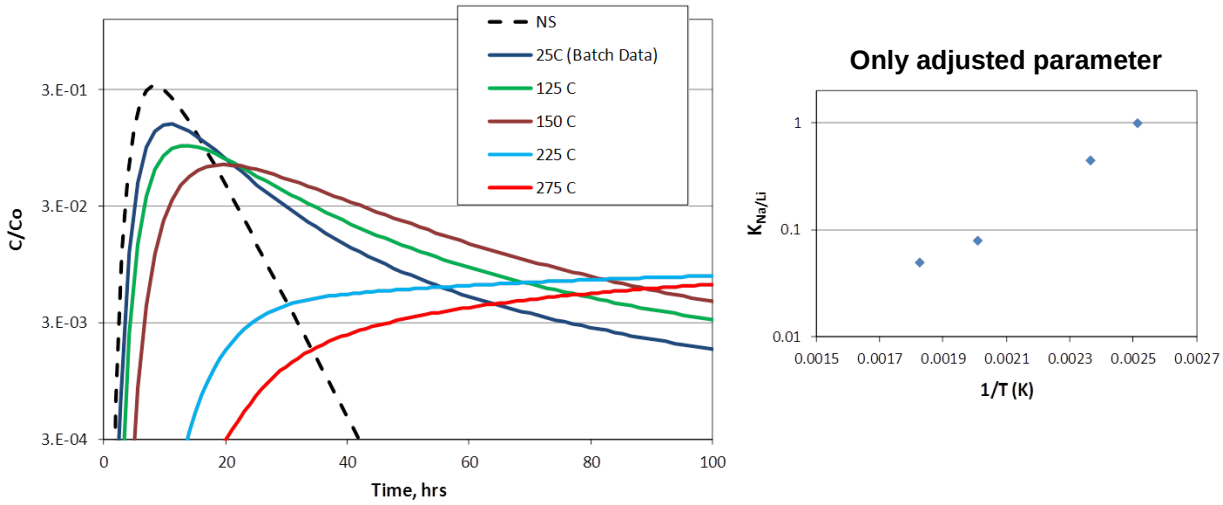

Figure 12. Left plot: NS and Li^+ breakthrough simulations from 25 ºC to 225 ºC assuming LANL column experimental conditions (~10 hr residence time, ~2.5 hour tracer pulse). Right plot: selectivity coefficient ($K_{Na/Li}$) as a function of inverse temperature (1/T) from the simulations.

Conclusions

The results of this study underscore the importance of evaluating tracer transport behavior at target geothermal system temperatures rather than relying on laboratory data obtained at lower temperatures. The room temperature batch experiments on individual minerals and a mineral assemblage representative of Newberry Crater reservoir fracture coatings significantly under-predicted lithium cation-exchange in column transport experiments under simulated reservoir conditions. Also, the relative retardation of lithium and cesium in the high-temperature column experiments was unexpected in that the retardation of lithium was greater than that of cesium. We hypothesize that the change in hydration characteristics of lithium ion as a function of temperature are responsible for the dramatic differences seen in lithium transport behavior over the range of temperatures studied here. We also hypothesize that cesium sorption/retardation in the Newberry mineral-water system will exhibit less temperature dependence than lithium because cesium ion has a much smaller temperature dependence of hydration than the lithium ion. This hypothesis is supported by the unexpected smaller retardation of cesium relative to lithium at 225ºC reported here (it is well established in the literature that cesium sorbs much

more strongly than lithium to virtually all minerals at low temperatures). Experiments are currently in progress to further test these hypotheses.

References

Dean, C. A., P. W. Reimus, et al. (2013). Laboratory Experiments to Characterize Cation Exchanging Tracer Behavior at Newberry Crater, OR. Thirty-Eighth Workshop on Geothermal Reservoir Engineering Stanford University, Stanford, California, ; 2013-02-11 - 2013-02-13 ; Menlo Park, California, United States. **LA-UR-13-20806:** 15 p.

Gaines, G. L. J. T., Henry C. (1955). "Adsorption Studies on Clay Minerals. V. Montmorillonite-Cesium-Strontium at Several Temperatures." The Journal of Chemical Physics **23**: 2322.

Gast, R. G. and W. D. Klobe "Sodium-lithium exchange equilibria on vermiculite at 25 degrees and 50 degrees C." Clays and Clay Minerals **19**(5): 311-319.

Kraus, K. A. and R. J. Raridon (1959). "Temperature Dependence of some Cation Exchange Equilibria in the Range 0 to 200°." The Journal of Physical Chemistry **63**(11): 1901-1907.

Third Quarter

Paul Reimus and Cindy Dean, LANL:

During the third quarter, two additional column transport experiments were conducted at room temperature in the same column that was used for the high-temperature experiments at LANL. One experiment was conducted using lithium as a cation-exchanging tracer and the other was conducted using cesium. The results of these experiments are still being analyzed, but the preliminary indication is that the transport behavior of both cations is in good agreement with what would be predicted using a single-porosity transport model with the sorption parameters determined in the room-temperature batch sorption experiments conducted with the Newberry mineral mix (see 2nd quarter results). This result suggests that the sorption parameters determined in batch experiments can provide reasonable predictions of column transport behavior provided the temperatures in the batch and column experiments are nearly the same. The higher-temperature experiments clearly demonstrated the inability to use the room temperature sorption data to predict high-temperature transport behavior.

The MULTRAN model was also used to predict the room-temperature column transport of lithium and cesium using the parameters deduced from the high-temperature experiments but allowing for an increase in the value of $K_{Na/Li}$ (in accordance with Figure 12) and a decrease in the value of $K_{Na/Cs}$ to match the column breakthrough curves. Good matches to the column data were obtained using a value of 1.2 for $K_{Na/Li}$, which was slightly larger than the value used to match the 125°C lithium column data (1.0), and a $K_{Na/Cs}$ value that was a factor of 4.5 times smaller than the value used to simulate the 225°C cesium column experiment. Given that the MULTRAN model assumed a dual-porosity system with a very small rim-zone porosity, these results suggest that the transition from dual-porosity cation transport behavior at higher temperatures to single-porosity behavior at low temperatures is primarily a function of the temperature dependence of the tracer diffusion coefficients in the rim zone. At lower temperatures the diffusion coefficients are small enough that diffusion into the rim zone has very

little influence on the tracer breakthrough curves, resulting in what appears to be single-porosity behavior. However, at higher temperatures, the influence of diffusion into the rim zone is more pronounced, and dual-porosity behavior is observed.

Fourth Quarter

Task complete.

Task 4.2: Purchase Tracers (Conservative and Adsorbing) and Initiate Interwell Tracer Test

First Quarter, 2013

A new candidate sorbing tracer is being investigated for its use in estimating the interwell fracture surface area in an interwell tracer test at the Soda Lake, Nevada geothermal field, which is planned for the second quarter. Likewise, another sorbing tracer, rhodamine WT (see the 2012 annual report), is planned for use in characterizing the fracture surface area resulting from hydrofracking a shale-gas reservoir. Tracer tests accompanying the hydrofracture are planned for the third quarter of this year.

Second Quarter

The new candidate sorbing tracer was not identified in time to be included in the tracer test at Soda Lake. The field experiment was therefore delayed until a new testing opportunity could be identified.

Task 4.3: Collect and Analyze Samples

First Quarter, 2013

Samples will be obtained and analyzed as part of the field experiments described in Task 4.2.

Task 4.4: Invert the Tracer Data to Determine the Fracture Surface Area Between the Injection and Production Well Pair

First Quarter (Mark Williams, PNNL and Eric Brauser, EGI):

During the first quarter of FY13 work continued on developing preliminary scoping simulations of the conservative and sorbing tracer injection tests for Newberry Crater based on the nominal stimulation/diverter operational design. Details of the nominal design for the ToughReact model were summarized in the FY12 Q4 report. In addition to these models being used to help plan the tracer tests; a ToughReact modeling framework is being set up for use in interpretation of the Newberry tracer test results. Limitations in this initial ToughReact modeling was the use of Kd linear sorption for the cations (i.e. Li and Cs). It was determined that a more realistic method for simulating the cation tracer transport was to implement cation exchange reactions (as was done in the preliminary Multran scoping simulations) into the ToughReact simulations.

Work was begun during this period to implement the cation exchange reactions into the ToughReact tracer simulations. For the initial development and to familiarize ourselves with the ToughReact cation exchange parameters we focused on simulating the four separate trimix column experiments conducted in September and October of 2012. These experiments included two LiBr and two $CsCO_2H$ sorbing tracer injections which also included conservative tracers. Details of these laboratory experiments were provided in the FY12 Q4 report.

The column transport experiments were conducted using a mix of ground calcite, albite, and quartz sand grains packed in 20" long, 1" diameter stainless steel column. Assuming a mean particle density of 2.65 g/cm^3 and a measured bulk density of 1.35 g/cm^3 provided a porosity of 49%. A groundwater analogue was prepared to mirror ion concentrations found at pad 29, but modified slightly after initial laboratory tests revealed large variations in effluent pH and pressure. Tracer solutes were then introduced as either LiBr or $CsCO_2H$ in order to study the retardation of cations through the column. The inlet concentrations used in the experiment can be seen in Table 8-1. The column was flushed with tracer-free groundwater to establish initial conditions before introducing tracer-containing groundwater. The pulse length and rates can be seen in Table 8-2.

Table 8-1. Simulated Groundwater (Pad 29)

Species	Ca	Mg	Na	K	HCO3	SO4	Cl	Li	Cs	Br	1,5-NDS
Exp't Conc [mM]	0.2500	0.2593	0.2348	0.1205	0.5750	0.1366	0.3836	1.2	1.2	1.2	0.03-4.7

Table 8-2. Experiments

	Li 9/12	**Li 9/24**	**Cs 9/26**	**Cs 10/8**
Pulse Length (min)	142.0	136.0	45.8	130.0
Pulse rate (ml/min)	2.060	2.050	2.063	2.080

ToughReact V2.0 was used to build 1-D simulations of these column tests. A 2mm node spacing was selected to match the small dispersion measured in conservative tracer breakthough curves. Cation exchange reactions were used to simulate the major cations and the Li and Cs tracer pulses.

The retardation of the cation breakthrough is determined by the concentration of exchange sites in the solid media and the varied magnitudes of selectivity for individual cations, which is analogous to an ionic-strength dependent rate constant. The CEC represents the potential number of cations which can be accommodated by the media interlayers, and is measured in charge equivalents per mass or volume of solid media. The actual affinity of the media for the particular

cations is seen in the selectivity coefficient K^*_{ij} and is dependent on the activities of species *i* and *j* both in solution and in the interlayers. Interlayer activities in ToughReact are defined using the Gaines-Thomas convention, which approximates activities using the fraction of total available sites. ToughReact incorporates these two aspects of cation exchange in the chemical.inp file through the CEC (measured in meq/100 g media) and the dimensionless exchange coefficients for each cation (relative to Na^+).

The ToughReact simulations of the CEC reactions for the trimix experiments are still in progress. Preliminary simulations are being updated based on feedback from other project members. Results for the CEC and selectivity coefficients will be reported along with a comparison of the simulated tracer responses to the measured laboratory values. Once adequate results are obtained for the trimix experiments, the preliminary Newberry Crater ToughReact simulations will be updated with the appropriate cation exchange processes and parameters. These parameters will also be updated based on ongoing laboratory experiments with these cation tracers and mineralogy similar to the Newberry Crater reservoir.

Third Quarter

Paul Reimus and Cindy Dean, LANL:

Several MULTRAN simulations were conducted to predict lithium tracer responses in single-well tracer tests performed during fracture stimulation at Newberry Crater, OR based on the results of laboratory experiments conducted at LANL and EGI. These are hypothetical calculations because tracer return curves were not yet available to invert at the time of this report.

Figure 13 shows predicted single-well tracer test breakthrough curves of both lithium and a hypothetical linearly-adsorbing tracer with a matrix partition coefficient of 0.5 ml/g along with breakthrough curves for both a halide and a naphthalene sulfonate. For these simulations it was assumed that there was a 5-hour tracer injection pulse starting at time zero, followed by injection of tracer-free water for 45 hours, followed by a 2-hour rest or non-flow period, after which the well was allowed to flow back. A linearly-adsorbing tracer response is shown in Figure 13 to illustrate how the response of a cation-exchanging tracer, which exhibits non-linear and hysteretic adsorption behavior, is expected to differ from that of an ideal linear, reversibly-sorbing tracer. Three plots are shown in Figure 13 for three different fracture half-apertures, *b*, (or fracture volume to surface area ratios) to allow a qualitative evaluation of how well the cation-exchanging tracer method is capable of distinguishing between different values of this key parameter.

The simulations of Figure 13 were conducted using the model parameters that yielded good simultaneous fits to the LANL and EGI column transport experiments described above in Section 4.1, 2nd quarter, 2013. The matrix was assumed to have a very low porosity (0.00001 or 0.001%) except for a very thin rim-zone layer (0.04 cm thick) at the fracture wall, and even this layer was only assigned a porosity of 0.0012 or 0.12%. However, this thin layer was also assigned a relatively large cation exchange capacity of 0.046 eq/kg. The fracture surfaces were assigned a cation exchange capacity of 0.0011 eq/kg. Matrix diffusion coefficients in the rim

zone were assumed to be 1×10^{-6} cm^2/s for the halide and the linearly-adsorbing tracer, 2.5×10^{-7} cm^2/s for the naphthalene sulfonate, and 6.7×10^{-7} cm^2/s for lithium. The temperature in all the simulations was set to 275°C, which is the approximate temperature at the depth of an interval that lithium ion was injected into at Newberry Crater during a stimulation in December 2012. The selectivity coefficient for exchange between sodium and lithium, $K_{Na/Li}$, was assumed to be 0.05 based on the value of this parameter deduced from the 275°C column experiment (see Figure 12).

As Figure 13 shows, the ability to use conservative tracers with different diffusion coefficients to distinguish between different fracture half-apertures is effectively lost because of the extremely low matrix porosities in the simulated system(s). The conservative tracer breakthrough curves effectively fall on top of each other despite the order-of-magnitude range in fracture half-apertures in the simulations. However, there are significant differences in the adsorbing tracer breakthrough curves for the different fracture half-apertures, implying that the adsorbing tracers could still be used to provide estimates of half-apertures in single-well tracer tests in such a system even though the conservative tracers fail to provide this information.

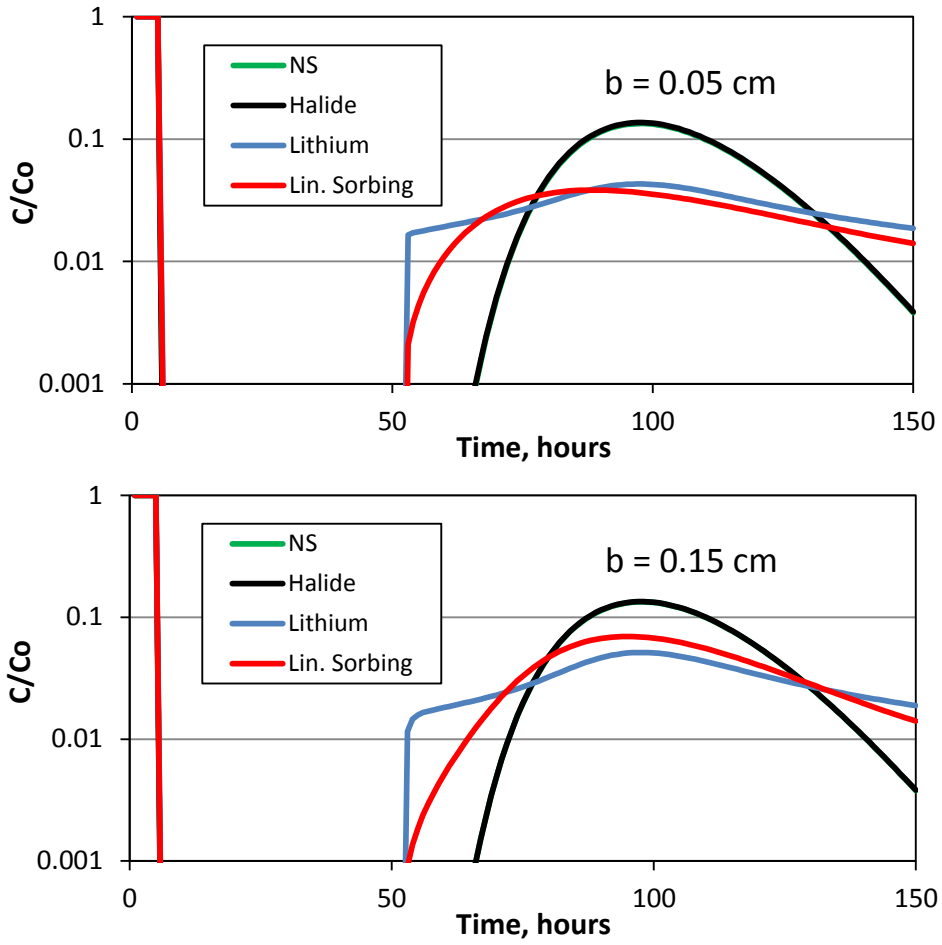

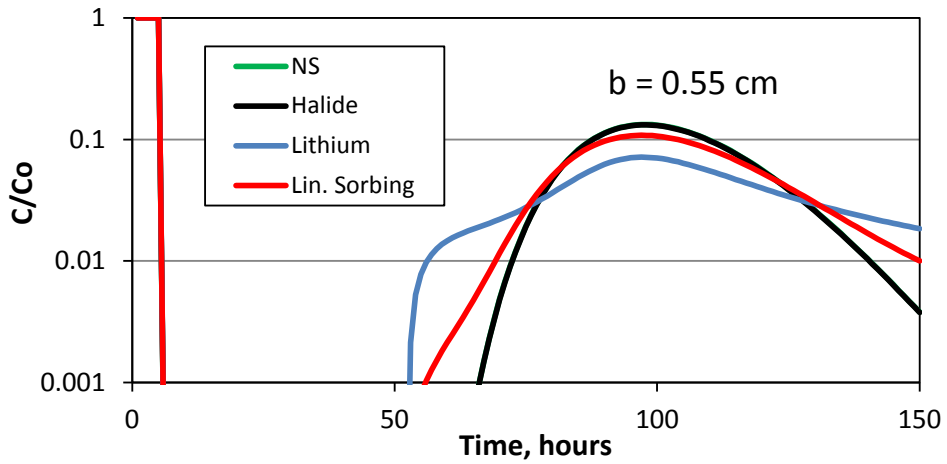

Figure 13. Simulated Single-Well Breakthrough Curves as a Function of Fracture Half-Aperture for a Naphthalene Sulfonate, a Halide, a Cation-Exchanging Tracer, and a Linear Reversibly Adsorbing Tracer in a System with Matrix Diffusion and Cation Exchange Parameters Similar to those Measured in the Newberry Crater Laboratory Column Experiments (see text). Simulated Tracer Injection of 5 hrs, followed by Injection of Tracer-Free Water for 45 hrs, and then a 2-hr Rest Period.

Figure 14 shows the results of simulations conducted at four different temperatures ranging from 50°C to 275°C using the same physical system parameters and tracer testing parameters (50-hr injection, 2-hr rest) as in Figure 5.9, but with the fracture half-aperture fixed to its smallest value in Figure 13. The differences in the simulated breakthrough curves in this case are a result of the temperature dependence of the matrix diffusion coefficients of the tracers as well as the temperature dependence of the cation exchange selectivity coefficient $K_{Na/Li}$ for lithium, which is deduced from the laboratory column experiments (Figure 12). Both temperature effects tend to increase the separation between the conservative tracer and adsorbing tracer breakthrough curves at higher temperatures. Note that the matrix partition coefficient of the linearly-adsorbing non-cation-exchanging tracer was assumed to have no temperature dependence, so the differences in the breakthrough curve of this tracer as a function of temperature purely reflect the influence of the temperature dependence of the diffusion coefficient. Note also that the breakthrough curves of the conservative tracers with different diffusion coefficients were identical at the different temperatures despite the significant differences in the diffusion coefficients as a function of temperature. These results show the importance of accounting for temperature when using adsorbing tracers to interrogate surface-area-to-volume ratios or fracture half-apertures in single-well tracer tests.

Figure 15 shows that the tracer breakthrough curves obtained at 275°C for the simulated conditions of Figure 14 but with significantly different rest periods (2 hrs vs. 50 hrs) are quite similar. This result is different than what is predicted for a system of significant matrix porosity where all tracers are expected to exhibit significantly lower peak concentrations and longer tails after a longer rest period because of the additional matrix diffusion that occurs during the rest period. The result of Figure 15 demonstrates that in a system of very low matrix porosity where there is no observed separation in the breakthrough curves of conservative tracers with different

diffusion coefficients, estimates of fracture half-apertures from adsorbing tracers are relatively insensitive to rest periods.

All of the cases considered in this section, and the corresponding breakthrough curves presented in the figures, only scratch the surface of the many possibilities of cation-exchanging tracer responses (and adsorbing tracer responses in general) that could occur in single-well injection withdrawal tests. The wide range of potential tracer adsorption or cation exchange parameters, including the adsorption/exchange capacity of the rock, result in an essentially infinite range of possibilities. However, the cases presented here should serve to illustrate some general trends that can be expected and some advantages as well as limitations of using adsorbing tracers in single-well tracer tests for surface area interrogation. The important take-home message with cation-exchanging tracers and linearly-adsorbing tracers is that the diffusion and adsorption behavior of the tracers should be carefully characterized in the specific system in which they will be applied to obtain the best possible estimates of fracture half-apertures or surface-area-to volume ratios.

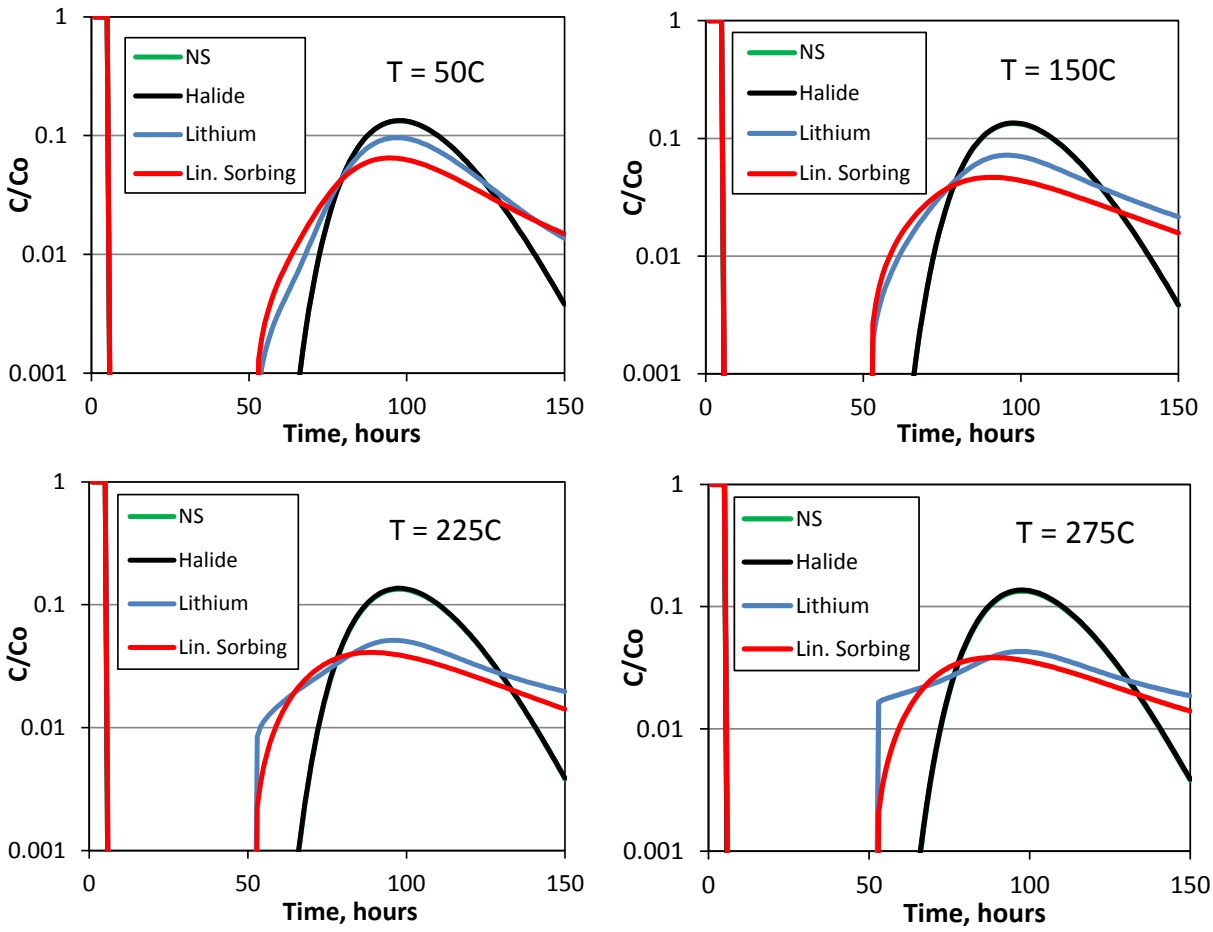

Figure 14. Simulated Single-Well Breakthrough Curves as a Function of Reservoir Temperature for a Naphthalene Sulfonate, a Halide, a Cation-Exchanging Tracer, and a Linear Reversibly Adsorbing Tracer in a System with Matrix Diffusion and Cation Exchange Parameters Similar to those Measured in the Newberry Crater Laboratory

Column Experiments (Fracture Half-Aperture = 0.05 cm). Simulated Tracer Injection of 5 hrs, followed by Injection of Tracer-Free Water for 45 hrs, and then a 2-hr Rest Period. Matrix diffusion and cation exchange parameters are discussed in the text.

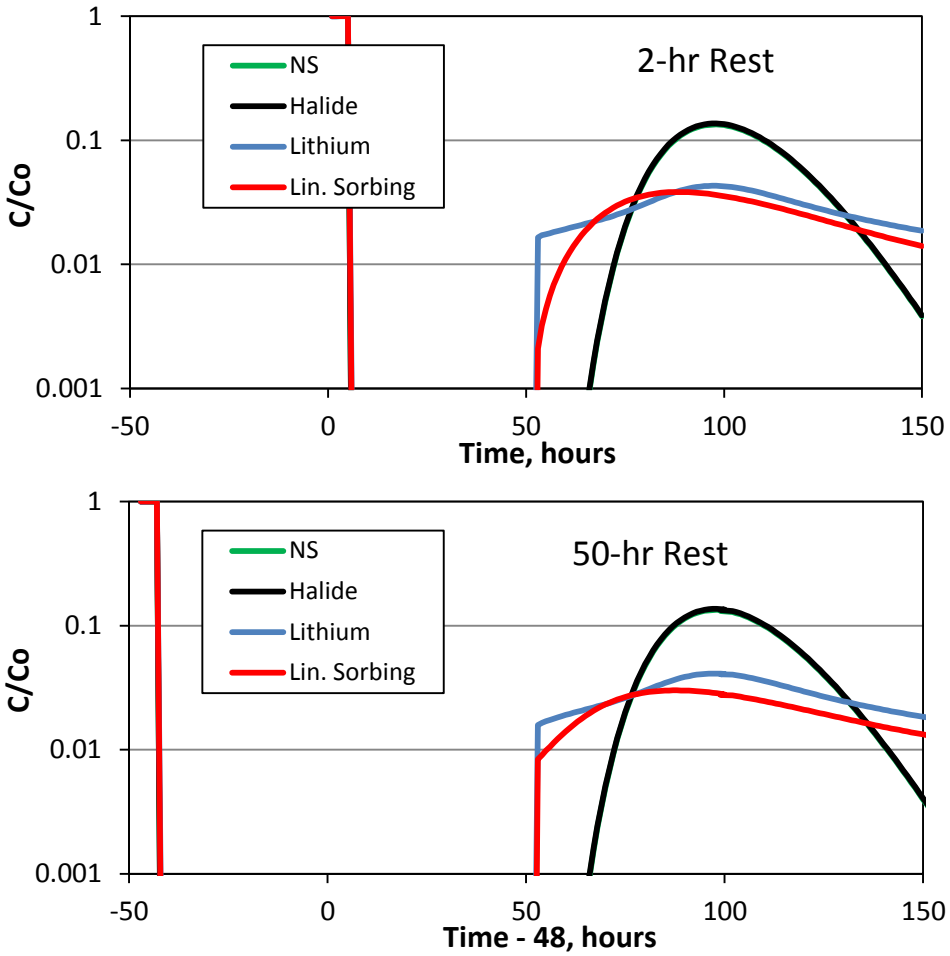

Figure 15. Simulated Single-Well Breakthrough Curves as a Function of Rest Period for a Naphthalene Sulfonate, a Halide, a Cation-Exchanging Tracer, and a Linear Reversibly Adsorbing Tracer in a System with Matrix Diffusion and Cation Exchange Parameters Similar to those Measured in the Newberry Crater Laboratory Column Experiments (Fracture Half-Aperture = 0.05 cm, Temperature = 275^{o}C). Simulated Tracer Injection of 5 hrs, followed by Injection of Tracer-Free Water for 45 hrs, and then a 2-hr or 50-hr Rest Period. Matrix diffusion and cation exchange parameters are discussed in the text.

Fourth Quarter

Task complete.

Task 4.5: Re-Deploy the Field Fluorimeter to Demonstrate Both Fracture Activation and Downhole Measurements of Flow Rate

Background

The original design of the field fluorimeter was analyzed and considered to be too risky to pursue. It was to consist of a spectrometer (complete with fiber optics, a CCD camera and a laser light source) located at the surface near the wellhead. One of the problems identified with the design, however, was the need to mount the spectrometer on the coiled-tubing drum that will be used to deploy the fiber optic cable. The optical fiber would be deployed within the coiled tubing in order to protect it from the harsh environment within the wellbore. However, there are many problems associated with deploying 10,000 ft of optical fiber—even if that fiber is enclosed within capillary tubing. Not only is the fiber quite expensive to deploy in this fashion, any break in the fragile fiber would of course render the tool inoperable. Given these risks, an alternative design was developed that will allow for the deployment of the spectrometer downhole on a wireline, thus avoiding the problems associated with deploying optical fiber over long distances within EGS wellbores. The drawback of this approach is that the tool will now have to be designed and fabricated in such a fashion that it can be deployed downhole and through a lubricator, limiting the diameter of the tool to about 2.6 inches. As described below, excellent progress is being made towards the design and fabrication of the tool.

Current Design

A sketch of the tool design is shown below.

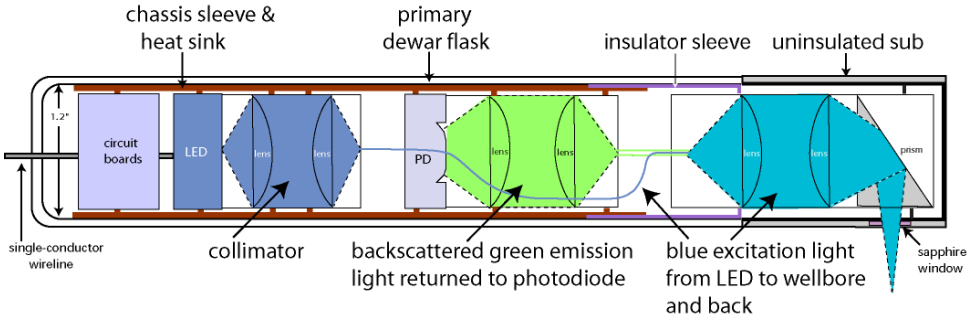

Figure 16. Sketch of the proposed borehole fluorimeter tool.

First Quarter, 2013 (Bruce Boyes, Systronix):

The fabrication of the prototype fluorimeter was completed, including the printed circuit boards that control the operation of the LED and photo-diode. Shown in Figure 17 is picture of the portion of the borehole-fluorimeter prototype that includes the LED light source and the photo-diode detector (with accompanying optics and electronic controls) inside its protective heat-sink chassis. Not shown are the collimator lens and prism at the right of the sketch in Figure 16 that serve to deliver the excitation light signal and return the backscattered light signal. Also not shown is the protective plastic sleeve that will seal the sensitive components in the prototype. In

the temperature-hardened version of the tool this plastic sleeve will be replaced by the thermally insulating Dewar flask.

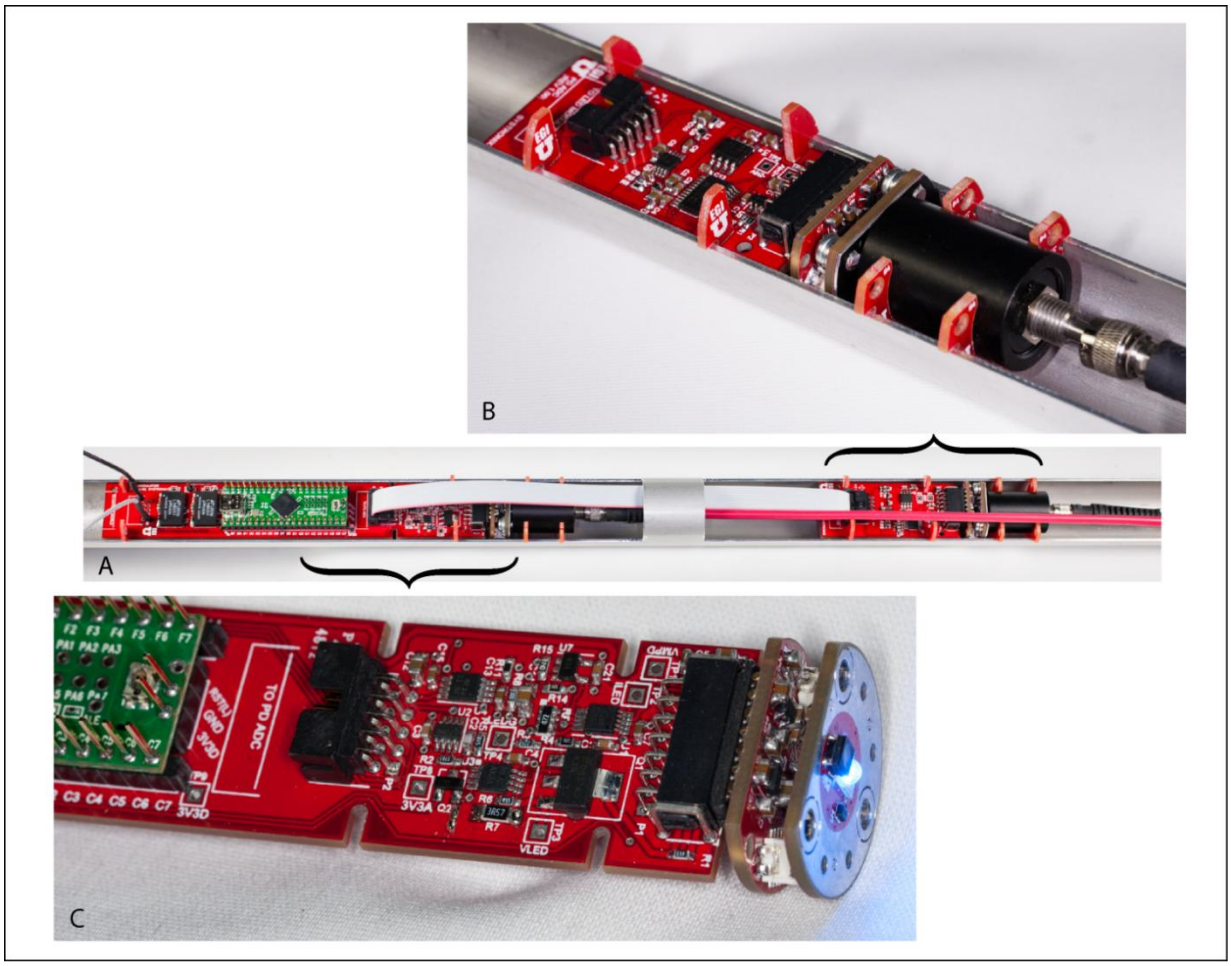

Figure 17. Photographs of a portion of the borehole-fluorimeter prototype, showing (A) the assembled LED light source and photo-diode detector with accompanying fiber-optics, collimators, and electronic controls, (B) an expanded view of the photo-diode detector with the associated circuit boards, collimator, and fiber-optic, and (C) an expanded view of the blue LED light source and associated circuitry.

Second Quarter, 2013 (Bruce Boyes, Systronix):

This quarter, work focused on refining the low-level firmware which communicates with all the new sensors and data converters on the boards shown in Figure 17, and on finishing the design and fabrication of the canoes and related optics mounts and fixtures.

All circuit boards and their solid-state components in this six-circuit-board system have been verified to work properly, which in itself is a significant accomplishment. These boards incorporate multiple new high-resolution design circuits - so there are many chances for mistakes. The firmware work includes writing custom Arduino-compliant libraries. The

photodiode detector AD7794 in particular is a powerful and sophisticated component. The flip side of this sophistication is that there are dozens of interactive configuration, gain, and digital filter settings. This work is ongoing.

The next major step in achieving full operation of this V2 prototype (once the sensor and converter libraries are complete) involves closing the control loops around LED power control, and fine-tuning the fixed and programmable gains of the solid state photodiode photodetector. The LED has feedback sensors which measure its actual drive current, temperature immediately adjacent to the LED emitter die, and its actual light output where it couples to the collimation lens tube. All three of these are needed to ensure the LED output is precise and stable over variations in devices and temperature. The photodiode detector has both fixed gain stages in its transimpedance amplifier as well as programmable gain and filtering within the AD7794 converter. These all need to be characterized to give the sensor the best usable gain range over the expected values of fluorescence signal (hence the need for the laboratory flow simulator).

Part of this process involves integrated auto-calibration using an optical power meter. In the next stage we plan to implement a compact photomultiplier tube sensor (PMTs are currently the industry standard) as a known reference to which we can compare the performance of our photodiode photodetector.

As part of the firmware test process we left the LED temperature sensor running in our laboratory. Its 13-bit resolution (0.0625 deg C per count) reveals in great detail the temperature swings and deadband of a typical setback HVAC thermostat.

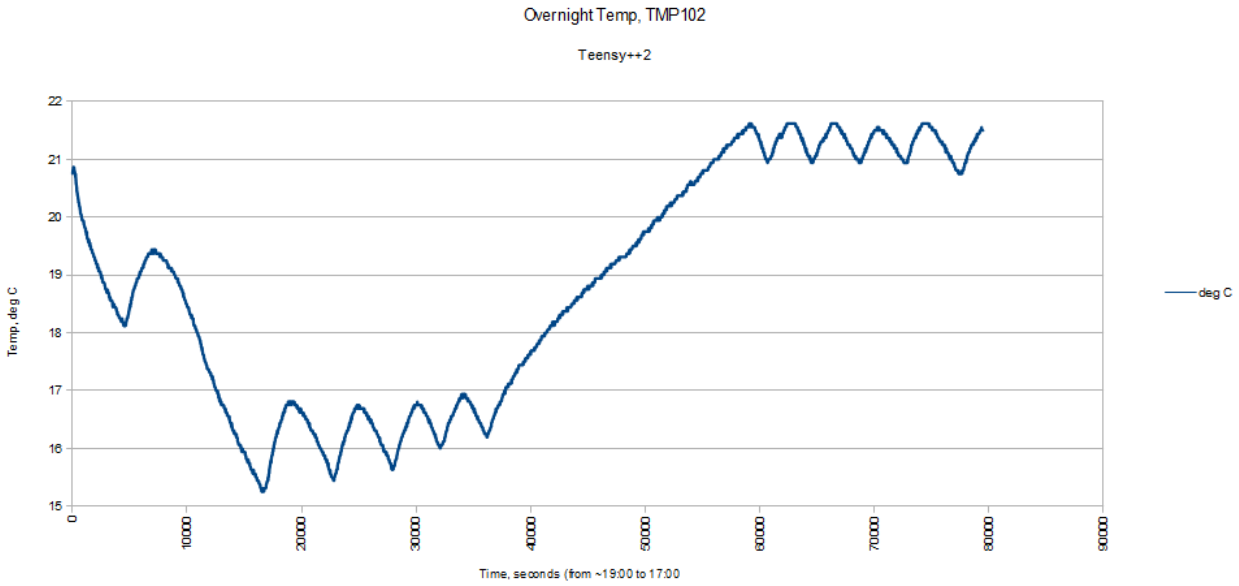

Figure 18. Sample temperature data showing the night and day oscillations of the heating system in the Systronix laboratory, with a resolution of 0.0625°C per count.

The long aluminum "canoe" tube (it has since been black anodized for durability and reduced optical reflection) shown in Figure 17 is designed to fit in the laboratory flow simulator. Its 60-inch length makes it awkward to use on the firmware benchtop, so we also fabricated shorter 12-

and 24-inch mini-canoes which greatly ease development. Additional lens and prism mounting components (modified stock pieces from Thorlabs) were also designed, fabricated, and anodized.

Fourth Quarter

Task complete.